

NAVAL POSTGRADUATE SCHOOL

Monterey, California



THESIS

**SUBTIDAL CIRCULATION OVER THE UPPER SLOPE TO
THE WEST OF MONTEREY BAY, CALIFORNIA**

by

Juan Aguilar Morales

September 2003

Thesis Advisor:

Curtis A. Collins

Co-Advisor:

Reginaldo Durazo

Approved for public release; distribution is unlimited

THIS PAGE INTENTIONALLY LEFT BLANK

REPORT DOCUMENTATION PAGE			<i>Form Approved OMB No. 0704-0188</i>	
Public reporting burden for this collection of information is estimated to average 1 hour per response, including the time for reviewing instruction, searching existing data sources, gathering and maintaining the data needed, and completing and reviewing the collection of information. Send comments regarding this burden estimate or any other aspect of this collection of information, including suggestions for reducing this burden, to Washington headquarters Services, Directorate for Information Operations and Reports, 1215 Jefferson Davis Highway, Suite 1204, Arlington, VA 22202-4302, and to the Office of Management and Budget, Paperwork Reduction Project (0704-0188) Washington DC 20503.				
1. AGENCY USE ONLY (Leave blank)		2. REPORT DATE September 2003	3. REPORT TYPE AND DATES COVERED Master's Thesis	
4. TITLE AND SUBTITLE: Subtidal Circulation Over the Upper Slope to the West of Monterey Bay, California.			5. FUNDING NUMBERS	
6. AUTHOR(S) Aguilar Morales, Juan				
7. PERFORMING ORGANIZATION NAME(S) AND ADDRESS(ES) Naval Postgraduate School Monterey, CA 93943-5000			8. PERFORMING ORGANIZATION REPORT NUMBER	
9. SPONSORING /MONITORING AGENCY NAME(S) AND ADDRESS(ES)			10. SPONSORING/MONITORING AGENCY REPORT NUMBER	
11. SUPPLEMENTARY NOTES The views expressed in this thesis are those of the author and do not reflect the official policy or position of the Department of Defense or the U.S. Government.				
12a. DISTRIBUTION / AVAILABILITY STATEMENT Approved for public release; distribution is unlimited			12b. DISTRIBUTION CODE	
13. ABSTRACT (maximum 200 words) <p>Moored current meters were used to describe currents over the continental slope off Monterey Bay, California, from March 1998 to March 2003. The water depth at this location was 1800 m and current observations included of 16-88 m, 210-290 m, 305 m and 1200 m although measurements at 16-88 m were not continuous. Poleward currents dominated the flow between 24 and 305 m. At 305 m the mean flow was 3.9 cm/s toward 334°. Surprisingly, at 1200 m the mean flow reversed and was 0.8 cm/s toward 169°. The principal axis for the flow at 305 m (1200 m) was 349° (350°), the semi-major axis was 9.4 cm/s (5.8 cm/s) and the semi-minor axis 3.4 (2.0 cm/s). The direction of the principal axis and the mean flow at 1200 m was aligned with the bathymetry to the east of the mooring site. The seasonal cycle at 305 m was dominated by an acceleration of the poleward flow from a minimum near zero on April 15 to maximum, 25 cm/s on July 15. This flow resulted in an increase of temperature at 305 m of 1.2°C due to geostrophic adjustment and a corresponding 10 cm increase in sea level due to steric effects. The acceleration of alongshore flow was out of phase with the alongshore pressure gradient which was greatest in mid-April. At 1200 m, the temperature increase (0.2°C) only lasted from April 15 to June 1 after which equatorward flow increased and temperature decreased. Mesoscale variability dominated the velocity measurements with maximum variance at about 60-day periods. At 305 m, the eddy kinetic energy was greatest (smallest) in October (December), 40 cm²/s² (4 cm²/s²) while at 1200 m the maximum (minimum) occurred in July (February), 5 cm²/s² (0.5 cm²/s²). Poleward events were stronger at 305 m while equatorward events were stronger at 1200 m. The three first empirical orthogonal functions explained 90% of the temporal variability of the horizontal currents. The first, second, and third Z-scores represented flow along the principal axis, undercurrent vs. Davidson current, and upwelling modes, respectively. While the seasonal patterns for the first two modes agreed with seasonal variability described above, the seasonal variability of the upwelling mode (6% of the variance) indicated that the waters between 16 and 88 m flowed onshore during the spring and summer upwelling period.</p>				
14. SUBJECT TERMS California Current System, Seasonal and Mesoscale Circulations of Monterey, CA			15. NUMBER OF PAGES 128	
			16. PRICE CODE	
17. SECURITY CLASSIFICATION OF REPORT Unclassified	18. SECURITY CLASSIFICATION OF THIS PAGE Unclassified	19. SECURITY CLASSIFICATION OF ABSTRACT Unclassified	20. LIMITATION OF ABSTRACT UL	

THIS PAGE INTENTIONALLY LEFT BLANK

Approved for public release; distribution is unlimited

**SUBTIDAL CIRCULATION OVER THE UPPER SLOPE TO THE WEST OF
MONTEREY BAY, CALIFORNIA**

Juan Aguilar Morales
Commander, Mexican Navy
B.S. Naval School, 1985

Submitted in partial fulfillment of the
requirements for the degree of

**MASTER OF SCIENCE IN METEOROLOGY AND PHYSICAL
OCEANOGRAPHY**

from the

**NAVAL POSTGRADUATE SCHOOL
September 2003**

Author: Juan Aguilar Morales

Approved by: Curtis A. Collins
Thesis Advisor

Reginaldo Durazo
Co-Advisor

Mary L. Batteen
Chairman, Department of Oceanography

THIS PAGE INTENTIONALLY LEFT BLANK

ABSTRACT

Moored current meters were used to describe currents over the continental slope off Monterey Bay, California, from March 1998 to March 2003. The water depth at this location was 1800 m and current observations included depths of 16-88 m, 210-290 m, 305 m and 1200 m although measurements at 16-88 m were not continuous. Poleward currents dominated the flow between 24 and 305 m. At 305 m the mean flow was 3.9 cm/s toward 334°. Surprisingly, at 1200 m the mean flow reversed and was 0.8 cm/s toward 169°. The principal axis for the flow at 305 m (1200 m) was 349° (350°), the semi-major axis was 9.4 cm/s (5.8 cm/s) and the semi-minor axis 3.4 (2.0 cm/s). The direction of the principal axis and the mean flow at 1200 m was aligned with the bathymetry to the east of the mooring site.

The seasonal cycle at 305 m was dominated by an acceleration of the poleward flow from a minimum near zero on April 15 to maximum, 25 cm/s on July 15. This flow resulted in an increase of temperature at 305 m of 1.2°C due to geostrophic adjustment and a corresponding 10 cm increase in sea level due to steric effects. The acceleration of alongshore flow was out of phase with the alongshore pressure gradient which was greatest in mid-April. At 1200 m, the temperature increase (0.2°C) only lasted from April 15 to June 1 after which equatorward flow increased and temperature decreased.

Mesoscale variability dominated the velocity measurements with maximum variance at about 60-day periods. At 305 m, the eddy kinetic energy was greatest (smallest) in October (December), 40 cm²/s² (4 cm²/s²) while at 1200 m the maximum (minimum) occurred in July (February), 5 cm²/s² (0.5 cm²/s²). Poleward events were stronger at 305 m while equatorward events were stronger at 1200 m.

The three first empirical orthogonal functions explained 90% of the temporal variability of the horizontal currents. The first, second, and third Z-scores represented flow along the principal axis, undercurrent vs. Davidson current, and upwelling modes, respectively. While the seasonal patterns for the first two modes agreed with seasonal variability described above, the seasonal variability of the upwelling mode (6% of the variance) indicated that the waters between 16 and 88 m flowed onshore during the spring and summer upwelling period.

THIS PAGE INTENTIONALLY LEFT BLANK

TABLE OF CONTENTS

I.	INTRODUCTION.....	1
A.	LITERATURE REVIEW	1
1.	Large Scale Circulation.....	1
2.	The California Undercurrent.....	3
3.	Shelf Circulation	5
4.	Monterey Bay Circulation.....	6
B.	THESIS ORGANIZATION	8
II.	DATA COLLECTION	11
A.	MOORING S2.....	11
B.	MOORING M2.....	13
C.	WINDS AND SEA LEVELS	14
III.	RESULTS	23
A.	HISTOGRAMS OF UNSMOOTHED CURRENT OBSERVATIONS....	23
B.	MEANS, VARIANCES, AND INTEGRAL TIME SCALES	24
C.	CURRENT AND TEMPERATURE TIME SERIES	27
D.	SEASONAL VARIABILITY.....	29
E.	MESOSCALE VARIABILITY	31
F.	VERTICAL STRUCTURE.....	33
G.	STATISTICAL RELATIONSHIP BETWEEN CURRENTS AND SEA LEVELS AND WINDS.....	35
IV.	SUMMARY AND CONCLUSIONS	65
A.	CHARACTERISTICS OF CURRENTS OFF MONTEREY, BAY	65
B.	RECOMMENDATIONS FOR FUTURE WORK.....	67
	APPENDIX A. TIDAL COMPONENTS	73
	APPENDIX B. ROTARY SPECTRA ANALYSIS	79
	APPENDIX C. TIME SERIES OF CURRENTS AND TEMPERATURES, MEANS AND ELLIPSES PARAMETERS BY DEPLOYMENT AT 305 AND 1200 M...83	
	LIST OF REFERENCES	105
	INITIAL DISTRIBUTION LIST.....	109

THIS PAGE INTENTIONALLY LEFT BLANK

LIST OF FIGURES

Figure I-1.	Position of the Mooring S2 and M2. The location of sea level gauges at Monterey and Port San Luis is also shown.	10
Figure II-1.	Schematic diagram of mooring S2. Jacketed Wire Rope (JWR) is a wire designed for oceanographic applications, JWR of 1/4" (3/16") diameter was used in the upper (lower) portion of the array. Hardhats are enclosures that hold glass flotation spheres. A total of 13 hardhats were used in the array.	17
Figure II-2.	Plot of depth versus number of bad data for the ADCP at S2. Numbers and corresponding color marks in the legend are the deployment number.	18
Figure II-3.	Schematic diagram of mooring M2.	19
Figure II-4.	Time diagram showing ADCP data collection at mooring M2 from January 1, 1998 to March 30, 2003. Black dots show "bad" data flags.	20
Figure II-5.	Plot of depth versus number of bad data for the ADCP at M2. Numbers in the legend indicate month.	21
Figure III-1.	Histogram of speed (left) and direction (right) for currents, at (top) 290 m, (middle) 305 m, and (bottom) 1200 m depth. The upper panel is for ADCP measurements and the middle and bottom panels are for Aanderaa RCM8 measurements.	41
Figure III-2.	Scatter plot of 6 hourly detided 305 m current observations. Note that the origin of the ellipse coincides with the mean flow.	42
Figure III-3.	Scatter plot of 6 hourly detided 1200 m current observations. Note that the origin of the ellipse coincides with the mean flow.	43
Figure III-4.	Bathymetry at mooring S2. Red dots are the location of the mooring anchor for each of the 10 deployments from March 1998 to March 2003.	44
Figure III-5.	Integral time scale. (a) At 305 m depth, blue (red) major (minor) axis. (b) At 1200 m depth, blue (red) major (minor) axis.	45
Figure III-6.	Time series of daily average currents at 305 m depth.	46
Figure III-7.	Time series of daily average temperature observations at 305 m depth.	47
Figure III-8.	Time series of daily average currents at 1200 m depth.	48
Figure III-9.	Time series of daily average temperature observations at 1200 m depth.	49
Figure III-10.	Time series of daily average temperature and currents at 305 m (blue) and 1200 m (red), respectively.	50
Figure III-11.	Scatter plot of monthly 305 m current observations, from March 24, 1998 to March 11, 2003.	51
Figure III-12.	Scatter plot of monthly 1200 m current observations, from March 24, 1998 to March 11, 2003.	52
Figure III-13.	Progressive Vector Diagram for current meter at 305 m depth. Solid black line (blue, red, green, cyan) corresponds to 1998 (1999, 2000, 2001, and 2002). 53	

Figure III-14.	Progressive Vector Diagram for current meter at 1200 m depth. Solid black line (blue, red, green, cyan) corresponds to 1998 (1999, 2000, 2001, and 2002).....	54
Figure III-15.	Eddy field of daily averaged currents at 305 m. A 7-day running mean was used to remove high frequency variability.	55
Figure III-16.	Eddy field of daily averaged currents at 1200 m. A 7-day running mean was used to remove high frequency variability.	56
Figure III-17.	Rotary spectra of the currents at 305 m (upper spectra) and 1200 m (lower spectra). The red (blue) line is the anticlockwise (clockwise) rotation.	57
Figure III-18.	Eddy kinetic energy variance preserving spectra at 305 (red line) and 1200 m (blue line).	58
Figure III-19.	Mean (blue), principal axes (red), and standard deviation ellipses at (upper) M2, 16-88 m, and (lower) S2, 210-290 m.	59
Figure III-20.	Vertical structure of horizontal velocity at M2/S2. (upper) Zscore, mean and standard deviation of east-west (u) and north-south (v) components of velocity. (lower) Temporal variability of first three principal components as a function of yearday (left) and year (right). The first principal component is red, the second is blue and is displaced -1, and the third is green and displaced -2. Black solid lines in the lower right represent a biharmonic fit to the temporal variability of the corresponding principal component.	60
Figure III-21.	Frequency dependent transfer functions between adjusted sea level (ASL) for Monterey and S2 currents. From left to right, the panels are current width (upper left), phase (mid left), and coherence (bottom left) of ASL vs. 305 m currents. Current width (upper right), phase (mid right), and coherence (bottom right) of ASL vs. 1200 m currents. Red (blue) line is ASL vs. along shore currents (ASL vs. across shore currents), and the green line on coherence panels represents the 99% confidence interval.	61
Figure III-22.	Frequency dependent transfer functions for the change in horizontal pressure gradient versus S2 currents. The change in horizontal pressure gradient was approximated by subtracting ASL for Monterey from ASL at Port San Luis. From left to right, the panels are amplitude (upper left), phase (mid left), and coherence (bottom left) of ASL difference between Port San Luis and Monterey vs. 305 m currents. Amplitude (upper right), phase (mid right), and coherence (bottom right) of ASL difference between Port San Luis and Monterey vs. 1200 m currents. Red (blue) line is ASL difference between Port San Luis and Monterey vs. along shore currents (ASL difference between Port San Luis and Monterey vs. across shore currents), and the green line on the coherence panels represents the 99% confidence interval.	62
Figure III-23.	Frequency dependent transfer functions for rotary cross spectra. From left to right, the panels are amplitude (upper left), phase (mid left), and coherence (bottom left) of wind stress vs. 305 m currents. Amplitude (upper right), phase (mid right), and coherence (bottom right) of wind stress vs. 1200 m currents. The red (blue) line is the alongshore wind	

	stress vs. alongshore currents (across shore wind stress vs. across shore currents) and the green line on coherence panels represents the 99% confidence interval.	63
Figure IV-1.	Biharmonic fit to daily averaged data. Biharmonic frequencies include annual and semiannual frequencies. (a) Current speed at 300 m. Red (blue) line represents the v_r (u_r) component of currents. (b) Temperature at 300 m (1200 m) is the red (blue) line. (c) Currents at 1200 m. The red (blue) line represents the v_r (u_r) component of currents. (d) ASL difference between Monterey and Port San Luis (blue line) and the ASL at Monterey (red line). (e) Kinetic energy at 300 m (1200 m) is the red line (blue line). (f) Wind stress t_{rx} (t_{ry}) is the blue (red) line.....	71
Figure IV-2.	Comparison of current measurements at S2 (290 m) and M2 (288 m) using acoustic Doppler current profilers from February 8 to August 28, 2002. Upper left (upper right) east-west (north-south) velocity component. Solid red line is the linear regression of S2 and M2 measurements.....	72

THIS PAGE INTENTIONALLY LEFT BLANK

LIST OF TABLES

Table II-1.	Equipment included at S2. Nominal depth is 1800 m of water at the mooring site.....	15
Table II-2.	Deployments at Mooring S2.	15
Table II-3.	Timing error for each current meter by deployment at S2.....	16
Table III-1.	Statistics for the 6-hour, detided current meter data at 305 m and 1200 m for each six-month deployment of S2. Red (blue) quantities are maximum (minimum) values.	37
Table III-2.	Monthly mean currents at 305 m depth.	38
Table III-3.	Monthly mean currents at 1200 m depth.....	39
Table III-4.	Velocity statistics for M2/S2 using daily time series.....	40
Table IV-1.	Percent of variance of daily averaged data explained by a biharmonic fit which includes annual and semiannual frequencies.	69
Table IV-2	Comparison of ocean current measurements at S2 at 290 m and M2 at 288 m, using acoustic Doppler current profilers from February 8 to August 28, 2002.....	70
Table A-1.	Major harmonic tidal constituents at 305 m depth. Amplitudes and phases are relative to Greenwich central time. A Raleigh criterion of 0.1 was used. The percent of variance predicted / variance original is 2.5%. The technique used follows Pawlowicz et al. 2002.	76
Table A-2.	Major harmonic tidal constituents at 1200 m depth. Amplitudes and phases are relative to Greenwich central time. A Raleigh criterion of 0.1 was used. The percent of variance predicted / variance original is 2.5%. The technique used follows Pawlowicz et al. 2002.	77

THIS PAGE INTENTIONALLY LEFT BLANK

ACKNOWLEDGMENTS

Moorings M2 and S2 are maintained by the Monterey Bay Aquarium Research Institute (MBARI) and funded by David and Lucile Packard Foundation. Within MBARI, Dr. Francisco Chavez has directed the S2 mooring efforts. Support for these observations is gratefully acknowledged. Ms. Marla Stone was responsible for preparing the current meters on S2, and setting and retrieving the moorings. The latter were accomplished using the *R/V Point Sur*. The skill and competence of Ms. Marla Stone and the master and crew of the *R/V Point Sur* were also critical for this study.

This thesis involved many to whom I owe much for their assistance and scientific support during my research and I would like to offer my thanks, knowledge and appreciation.

I would first like to thank to my thesis advisor, Dr. Curtis A. Collins, and co-advisor, Dr. Reginaldo Durazo, for their wisdom, guidance and advice which facilitated the solution of problems during this study.

I would also like to thank Fred Bahr and Marla Stone, for their efforts in the joint data work-up, preparation and utilization. For their invaluable assistance in computer programming, I thank Mike Cook and Tarry Rago.

My special thanks to Jeff Dixon, Claude Gahard, Vincent Dominick, and Vic Ross for their help and words, my classmates with whom I spent many hours in the classroom during these last two years.

Most importantly, I would like to thank my family, my daughters Sofia and Fernanda, and specially my wife Josefina “Josse”, for providing encouragement, patience, and love.

THIS PAGE INTENTIONALLY LEFT BLANK

I. INTRODUCTION

The purpose of this study is to analyze and describe the seasonal and mesoscale circulations over the upper slope to the west of Monterey Bay, California, using a 5-year time series of currents at moorings S2 and M2 (Fig. I-1). Current variability is compared to the variability of sea level and winds for the same period as a possible cause of seasonal and mesoscale circulations. Since this study focuses on the region below the main thermocline over the continental slope, and therefore poleward flow is expected to influence the data set more than any other large scale feature of the California Current (CC) System.

A. LITERATURE REVIEW

1. Large Scale Circulation

The large-scale sub-tropical oceanic circulation in the North Pacific Ocean is dominated by a clockwise ocean-wide gyre driven by the anticyclonic atmospheric flow of the North Pacific High, the Aleutian low, and in summer the thermal low over the western United States. When the eastward flowing North Pacific Current impacts the North American continental shelf in the vicinity of southern Canada, it bifurcates and one branch flows northward into the Gulf of Alaska to form the counterclockwise flowing Alaskan current. The second branch flows southward and forms the CC (Duxbury et al. 1999).

A number of manifestations of counter-flow are observed to the east of the CC: Inshore Countercurrent (IC), Davidson Current (DC), Southern California Countercurrent (SCC), Southern California Eddy (SCE), and California Undercurrent (CU). These flows, with the CC, form the CC System (CCS).

The CCS is a classical eastern boundary current system extending approximately from the Strait of Juan de Fuca southward to the tip of the Baja California Peninsula. Seasonal variations in alongshore wind stress, coastline irregularities, bottom topography, and temperature and salinity variations, have been shown to be the mechanisms responsible for the observed large-scale structure within the CCS (Hickey, 1998).

The CC is an offshore (850-900 km), near-surface (0-300 m), and equatorward flow characterized by low salinities, low temperatures, and high dissolved oxygen, with average speeds of $\sim 10 \text{ cm s}^{-1}$. South of Point Conception and near the coast, a seasonal change occurs in direction of a narrow zone of coastal portion of the CC. Throughout the fall and winter and within approximately 150 km of the coast, the direction of the CC reverses forming the California Countercurrent (CCC). This current has also been called the IC (Lynn and Simpson, 1987). In regions north of Point Conception the IC is often referred to as the DC.

There are other IC currents. South of Point Conception, a portion of the CC turns southeastward, then shoreward and then poleward. This current is known as the SCC. When the CC recirculates within the southern California Bight, the flow is referred to as the SCE (Hickey, 1998).

The CC, CU, and the SCE all have seasonal maxima in summer to early fall. The IC has seasonal maxima in winter, coincident with the seasonal development of the Davidson Current in regions north of Point Conception (Hickey, 1998).

The water properties that make up this system are determined by four water masses that can be defined by their temperature, salinity, dissolved oxygen, and nutrients (Lynn and Simpson, 1987). Pacific Subarctic waters, formed by the Kuroshio extension (cooler, fresher waters), and characterized by relatively low temperatures, low salinity, high dissolved oxygen, and high nutrients, enter the CCS near 48° N and leave it near 25° N . Equatorial Pacific waters, from the eastern tropical Pacific, characterized by relatively high temperature, high salinity, low dissolved oxygen, and high nutrients, enter the CCS from the south and are carried northward by the CU. Eastern North Pacific Central waters enter the CCS from the west and are characterized by relatively high temperature, high salinity, low dissolved oxygen, and high nutrients. Upwelled waters are found within 50 km of the coast and are identified by relatively cold temperature, high salinity, high nutrients, and low dissolved oxygen.

Satellite imagery, field studies using Lagrangian drifter results, and recent numerical modeling efforts suggest the existence of numerous large-scale (50-300 km), and long-lived (20-40 day) jets and meanders in the region offshore of the northern

California shelf (Hickey, 1998). Filaments are the result of separation from the shelf of the coastal jet formed over the shelf during upwelling events. Batteen (1997) demonstrated that the upwelling jet that forms over the Oregon shelf separates from the shelf near Cape Blanco and meanders equatorward through the CCS during spring and summer. The flow then undergoes alternating cyclonic (offshore) and anticyclonic (onshore) excursions, and sheds westward propagating eddies.

2. The California Undercurrent

The CU is a relatively narrow (10-40 km width), subsurface poleward flow that flows over the continental slope from Baja California to at least Vancouver Island (Hickey, 1998). The CU has been the subject of numerous studies which include calculations of geostrophic velocity derived from hydrographic data to direct current measurements. It has a high velocity core (100-300 m depth), with an average speed of $30\text{-}50\text{ cm s}^{-1}$, and its flow can be interrupted by eddy-like features (Ramp et al. 1997).

Hickey (1979) reviewed the available observations of the CU and concluded that west of the North American coast, over the continental slope, northward subsurface flow is generally present and shows considerable seasonal variability in position, strength, and core depth. North of Point Conception, the flow at 200 dbars is stronger during winter than during summer and fall.

Chelton (1984) used 23 years of California Cooperative Oceanic Fisheries Investigation (CalCOFI) hydrographic measurements collected between 1950 and 1978 to describe the seasonal geostrophic velocity along two sections, one off Point Sur and the other off Point Conception. Chelton found that the geostrophic flow in the upper 100 m, referenced to 500 dbar, for both locations reversed annually with equatorial flow from February to September and poleward flow from October to January. Below 100 m, the flow at Point Conception was poleward through the year with two maximum flows occurring in June and December. The nearshore deep flow off Point Sur, however, reversed annually with maximum poleward flow in December and weak equatorward flow from March to May.

Lynn and Simpson (1987) also studied the seasonal variability of the CCS. Strong semiannual variability was prevalent for the CU off Central California, Point

Conception and within the Southern California Bight. The CU became weaker from January through March as its core was found at increasingly greater depths. The CU remained weak or vanishes from March through May. The maximum poleward flow velocity ($\sim 13 \text{ cm s}^{-1}$) was found in late fall to early winter. Tisch et al. (1992) selected seven cruises along the Point Sur Transect (POST) in order to determine seasonal variations of alongshore geostrophic velocities and water mass characteristics of the CCS. The core of the CU occupied a position 12 to 42 km from shore with speeds between 10 and 35 cm s^{-1} at depths of 70 to 460 m over the continental slope. The alongshore variability of the CU appeared to be related to both local and remote wind forcing.

Collins et al. (1996), analyzed currents measured at 350 m over the continental slope off Point Sur, from 1989 through February 1995. The pattern of monthly flow reveals that the spring transition begins in mid-April when temperature reaches its minimum. Subsequently the poleward flow triples its speed, persisting until mid-July with a steady warming. By mid-December temperatures start to decrease and the flow decelerates. Ramp et al. (1997) analyzed current meter data from seven moorings on the continental slope along the central California coast, from Point Piedras Blancas to Point Reyes. The poleward flowing CU was the most prominent feature observed, with flows over the slope occurring in 3 to 4 month bursts, with vector speeds exceeding 40 cm s^{-1} , and interaction with at least three eddy-meanders.

The continuity of the CU along California and Oregon coasts was established by measurements with isobaric RAFOS floats (Garfield et al., 1999); these float measurements yielded a mean alongshore velocity of 10.8 cm/s . Pierce et al. (2000), using ADCP data collected during July-August 1995, between Cape Blanco, Oregon, and Cape Mendocino,

California, found that the undercurrent was present over the 440 km mid-latitude eastern boundary of the North Pacific, with a mean maximum velocity of 0.18 m s^{-1} , core depth 200-275 m, overall mean of 0.10 m s^{-1} , and mean location 20-25 km off the shelf break.

Collins et al. (2000) measured velocity along 36.3° N to the west of Point Sur, California, and found mean poleward flow in the upper 1000 dbars within 100 km of the coast with maximum velocities, 6 cm/s , at a depth of 100 m next to the coast.

Noble and Ramp (2000) analyzed current meter data collected from two arrays parallel to each other consisting of six current meters moored for one year (March 1991-March 1992) across the central California outer shelf and slope. The alongshore mode empirical orthogonal function showed that coherent, surface intensified, alongshore fluctuations exist across the entire outer shelf and slope. Both the mean and first mode currents showed that the CU in this region is energetic, surface intensified and extended to depths of 800 m, and width of 40 km offshore of the shelf break. The CU in this region may be occasionally forced offshore through interactions with a seasonal offshore jet that probably originated at Point Reyes, hence this region may be important as a generation site for meanders and eddies in the CU. These fluctuations in the undercurrent were not correlated with the local wind stress or sea surface pressure gradients.

Collins et al. (2003) analyzed hydrographic data collected along CalCOFI line 67 for the period 1988-2002 perpendicular to the central California coast. Geostrophic adjustment of the pycnocline caused by seasonal variation of the CCS and the cycle of upwelling favorable winds, resulted in strongly seasonal inshore circulation. One of the important consequences to follow from these dynamics was that the offshore location of the CC jet (a surface-enhanced southward, coastal upwelling jet, with maximum velocities during late winter and spring which marked the inshore edge of the CC) was determined by the width and strength of the CU and Inshore Current. The CC was closer to shore when both the CU and Inshore Current were weak.

3. Shelf Circulation

The currents between the surf zone, also called the nearshore, and the shelf break are referred to as “shelf circulation”. Here depth is shallow (200 m and less) as compared to the deep ocean. Shelf circulation is dominated by low frequencies, compared to tidal and inertial oscillations, in regions where the shelf is relatively long and straight with fairly simple geometry.

A comprehensive summary of the present knowledge of the circulation of currents over the shelf region in the west coast of United States is given by Huyer (1990). The time scale of currents over the shelf region vary over periods ranging from a few days to a few weeks, and in some regions they vary also seasonally, and are different from those

currents in the open ocean (Figure 1, Huyer 1990). In eastern boundary currents the influence of the open ocean is relatively weak and current circulation responds to seasonal variations in the local winds, i.e. in the Northern Hemisphere the North Pacific high is displaced northward (southward) in summer (winter) and the equatorward winds along the coast associated with the high pressure system migrate and intensify seasonally, causing offshore Ekman transport and upwelling along the coast. Conversely, winds blowing along the coast in the opposite direction cause onshore Ekman transport and downwelling near the coast. The flow pattern along the western shelf of United States is similar: there is a shallow equatorward surface current (CC) with average velocities of 10 cm s^{-1} , and a subsurface undercurrent with a core depth between 100-300 m and average velocity of $30\text{-}50 \text{ cm s}^{-1}$.

Strub et al. (1987) analyzed the seasonal cycles of currents, temperatures, winds, and sea level over the continental shelf from 35° N to 48° N for the period 1981-1983, and characterized the fall-winter and spring-summer seasons. For fall-winter, north of 35° N monthly mean winds were northward for 3-6 months, and south of 35° N , were near zero or weakly southward. Over midshelf and shelf, monthly mean alongshore currents were northward from 35° N to 48° N at depths of 35 m and deeper and were associated with high coastal sea levels and relatively warm temperatures. For spring-summer, monthly wind stress was southward for all latitudes for 3-6 months, sea levels were low, water temperature was relatively cool, and monthly mean currents at 35 m depth over the shelf were southward 1-6 months while the deeper currents were less southward or northward. At 35° N annual mean currents at 35 m depth over midshelf and shelf break opposed to the annual mean wind, and from 35° N to 43° N both summer and winter regimes were dominated by strongly fluctuating currents.

4. Monterey Bay Circulation

The available information on currents offshore Monterey Bay indicates a complex and occasionally contradictory picture of the circulation in this region. There exists, superimposed on the large scale flow, mesoscale meanders, eddies, filaments and jet-like surface currents. Previous studies (Ramp et al. 1997; Collins et al. 1996) have shown that currents over the slope of Central California are dominated by long-period fluctuations.

These fluctuations have generally been associated with the offshore eddy and meander field.

Skogsberg (1936) conducted an extensive oceanographic study of Monterey Bay between 1929 and 1933, and described three distinct seasonal phases in his study of the hydrography of Monterey Bay. The “upwelling period” was caused by upwelling and extended from mid-February through August or September. Along the central California coast, winds from the northwest associated with the Subtropical High Pressure cell produce coastal upwelling, which in turn influences strongly the coastal circulation and thermal structure. The start of the upwelling season is marked by the so-called spring transition (Hickey, 1998), a rapid progression to sustained northwesterly winds along the west coast. At the latitude of Monterey area, coastal upwelling usually occurs between March and October (Breaker and Broenkow, 1994). Upwelling centers in the Monterey area are located north and south, near Point Año Nuevo and Point Sur, respectively (Paduan and Rosenfeld, 1996).

Pennington et al. (2000) used time series of temperature, salinity, nitrate, primary production and chlorophyll for the period 1989-1996 at station H3/M1 in central Monterey Bay and found that the upwelling period developed at about the same time as that described by Skogsberg (1936), but reached its maximum 1-2 months later. Pennington divide Skogsberg’s upwelling period into two seasons, early and late upwelling. During the early upwelling (February-April), isolines shoal in February, but the minimum surface temperatures occurred intermittently in March-June, and the upwelling reached its maximum in June with shallow isotherms but higher salinity and nitrate. During late upwelling (July-August), the upwelling decays with surface salinities remaining high but temperatures increase and subsurface isotherms and isohalines deepened.

The “oceanic period” extends from late summer to early fall. Skogsberg (1936) attributed this period to the onshore movement of oceanic waters associated with the CC. During this period the North Pacific high weakens and drifts southward, and the Aleutian low reforms. With the slackening of wind stress, the cool, upwelled water begins to sink and is replaced by warmer surface water from offshore, coastal sea surface temperatures

rise to their highest seasonal values and strong vertical temperature gradients form (Breaker et al. 1994). Rosenfeld et al. (1994), named this period as a “relaxation state” in which Monterey area is characterized by rapid onshore advection of warm oceanic water combined with surface warming.

The “Davidson current period” is from December through early-February, coincident with the local occurrence of the northward DC. In late fall and early winter of most years, northerly winds are weak and variable, and a northward flowing countercurrent usually forms at the surface, the DC. Periodically, strong southerly winds interrupt the anticyclonic atmospheric circulation pattern of the weakened North Pacific high, stimulating and reinforcing the northward DC. The southerly winds also generate onshore Ekman transport, resulting in general rise in the sea level due to water pile-up at the coastal boundary. The elevated sea level, in turn, causes downwelling and offshore cross shelf flow below the Ekman layer.

It is noteworthy that the description used above may be useful to describe the changing hydrographic conditions, but in reality these periods overlap extensively and do not recur with clockwork punctuality. The irregular timing of changes in the wind field and associated oceanographic effects, and aperiodic phenomena such as El Niño and La Niña, makes establishment of a regular timing for these periods difficult.

Rosenfeld et al. (1994) focused on Monterey Bay, observed the development of a warm, fresh anticyclonic eddy at the mouth of Monterey Bay, or just to the south of it, upon return of upwelling that immediately followed a relaxation event. Satellite observations suggest that a meander or warm-core eddy, 50 to 100 km in diameter, may be present upon occasion just west of Monterey Bay (Breaker, et al. 1994).

B. THESIS ORGANIZATION

Five years of ocean current observations at moorings S2 and M2, provide an opportunity to resolve the pattern of flow over the continental slope at the entrance to Monterey Bay. Observational methods will be discussed in Chapter II. Mean flow, seasonal and mesoscale variability, and forcing mechanisms are described in Chapter III. Chapter IV contains a summary of conclusions and recommendations for future work.

For purposes of clarity, each chapter has been organized as followed: first the body of the text, next tables and finally figures.

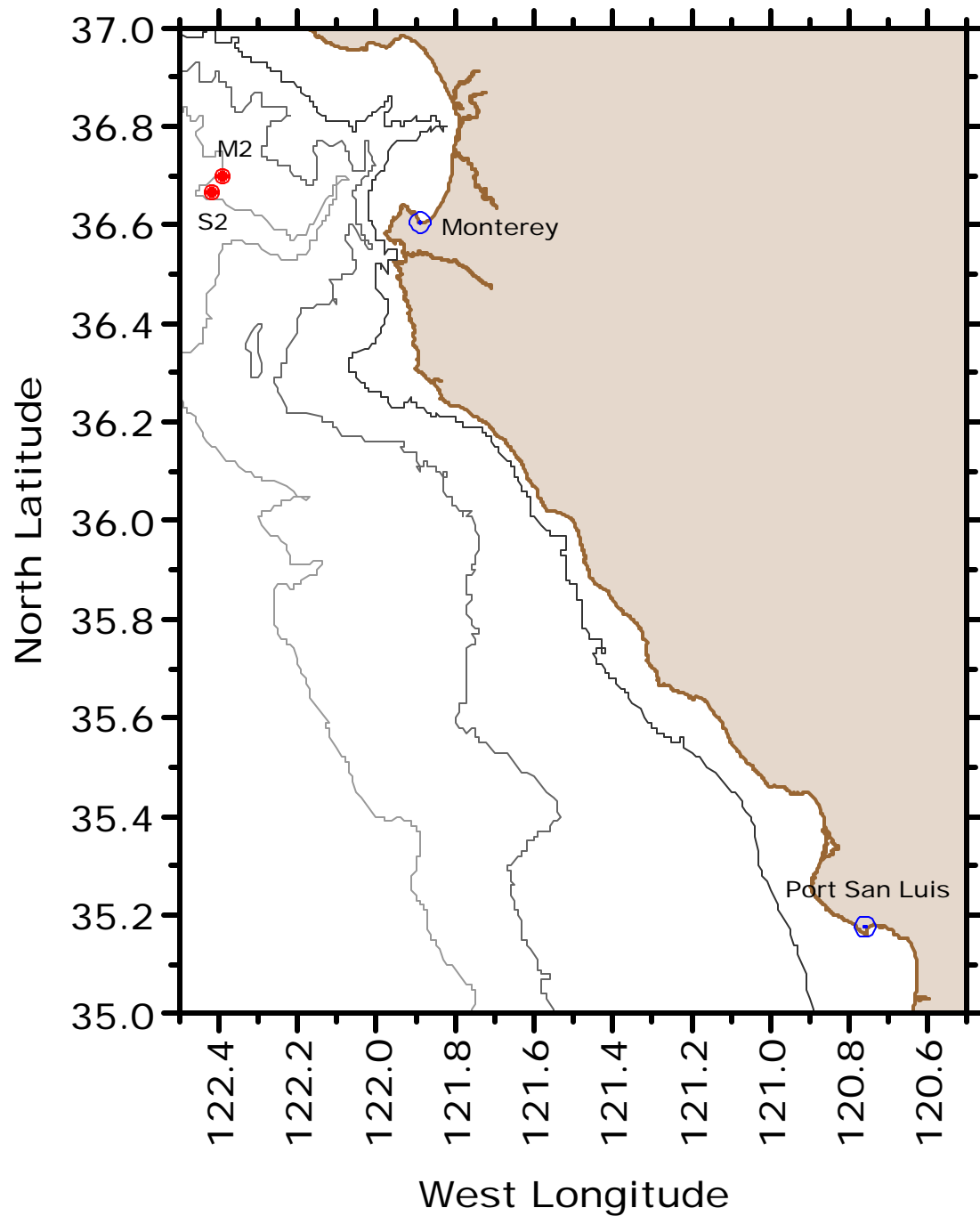


Figure I-1. Position of the Mooring S2 and M2. The location of sea level gauges at Monterey and Port San Luis is also shown.

II. DATA COLLECTION

Data collection and processing at both 305 and 1200 m, Aanderaa current meters, and acoustic Doppler current profiler (ADCP) at 300 m at mooring S2 are described in this chapter. Data collected by a downward looking ADCP and an anemometer at mooring M2 and maintained by Monterey Bay Aquarium Research Institute (MBARI), along with sea level data from two tide observation stations at Port San Luis and Monterey, and provided by the Hawaii's Sea Level Data Center, are also described.

A. MOORING S2

The Naval Postgraduate School (NPS) and the Monterey Bay Aquarium Research Institute (MBARI) have maintained a mooring of the intermediate type, designated S2, offshore Monterey Bay, and located in 1800 m of water at 36° 40' N and 122° 25' W. The mooring included an upward looking ADCP at 300 m depth, two current meters at 305 m and 1200 m depth, and IRSC and Honjo sediment traps below each meter, respectively (Fig. II-1, Table II-1). The mooring was buoyed with 13 Benthos glass flotation spheres with a total positive buoyancy of 299 kg as well as a subsurface sphere that contained the ADCP, which had a positive buoyancy of 455 kg. Photocell activated flashing lights, radio direction finders, and Argos transmitters were mounted on the upper flotation unit to facilitate recovery.

Deployments ranged in duration from five to six months, limited by the six-month sediment trap sampling capacity. Thus, 10 data collection deployments occurred over the continuous measurement period from March 1998 to March 2003 (Table II-2).

The current meters used at mooring S2 were Aanderaa recording current meter Model 8 (RCM8). The meters are self-contained instruments for recording vector averaged speed and direction. The raw data for each sensor was stored in the current meter's data storage unit (DSU) as a bit number ranging from 0 to 1023. Prior to deployment, all current meters sensors were calibrated or tested at NPS facilities. Current speed was measured by rotations of a shrouded paddle-type rotor magnetically linked to an electronic counter; the counter is tested for accuracy and proper operation in

the laboratory by using a modified rotor with known rotation rate. Current direction was measured by a magnetic compass. For the compass calibration, a table of bit numbers versus degrees was prepared by use of a compass stand surveyed to true north. The instruments also include pressure and temperature sensors.

Upon recovery, the raw Aanderaa recording current meter data files were converted to standard scientific units using the sensor calibration equations and stored as formatted ASCII files. Data were then visually inspected for outliers due to instrument failures or malfunctions, and were edited or deleted when necessary. Timing errors by deployment for each current meter are listed in Table II-3. After the editing process, gaps were linearly interpolated and records produced at 30 minute intervals.

Since this thesis focused on subtidal variability, the 30 minute observations were filtered with a cosine-Lanczos filter with a half power period of 2.9 hours (Alessi et al. 1985), to remove tides and inertial period currents (tidal current results are given in Appendix A). After filtering, the data were decimated to 1 hour intervals, and filtered again with a cosine-Lanczos filter with a half power point of 46 hours. Except for the Figure III-1, the data used subsequently in this thesis were obtained by then decimating the smoothed 1 hour time series to 6 hours.

The direction vane of the current meter at 305 m failed in the second half of 2000. To fill this gap, the current measurement at the first good bin (290 m) of the upward looking ADCP was used. Results discussed in Chapter III will justify this substitution.

ADCP data were collected at mooring S2 using an upward-looking RD Instruments 300 kHz broadband ADCP. The RD Instruments ADCP uses the principle of Doppler shift. It transmits sound at a fixed frequency and listens to the sound backscattered from particles in the ocean that move at the same horizontal velocity as the water. The ADCP measures average velocity over depth cells (bins) away from the acoustic transducer. The instrument at 300 m depth was configured to resolve currents in 4 m depth intervals over a period of 180 seconds and 25 pings. Adjacent bins overlap and are not independent.

The echo amplitude, or intensity, is a measure of the signal strength returned to the ADCP, and is adjusted by the automatic gain control of the ADCP. As the sound

travels further away from the transducer, the signal-to-noise ratio decreases, as does the echo intensity and the correlation values. Two criteria were used to “flag” bad ADCP data. When the echo intensity becomes a constant value (“flattens out”) for several successive bins, the ADCP has stopped collecting valid data. Comparing the echo intensity to the correlation, both values fall off (correlation values have fallen below 64 counts). The percent of good data also fall off (percent of good data should drop to zero), and are “flagged” as a bad data. A second criterion utilized the ADCP data output based on the three and four beam solution. If the percentage good for both 3 and 4 beam solutions are less than 25% data is “flagged” as bad data.

Figure II-2 shows the number of bad data for bins 1-20 for each deployment. When the number of bad values exceeded 10, it increased by a factor of ten for each of the next 2-3 bins. If 10% (874 bad data points for a 6 months record) is chosen arbitrarily as a limit for the last good bin, then bin 18 would be the last good bin for deployment five and six, bin 19 for deployments eight and ten, and bin 20 for deployment one.

RDI reports a nominal standard deviation due to instrument error of 0.04 cm s^{-1} for a 25-ping average for the broadband ADCP. Maximum pitch and roll recorded by the tilt sensors on the ADCP were -1.6° , and -1.4° respectively. Following manufacturer specifications, it was not necessary to correct data due to these movements.

B. MOORING M2

Since 1989, MBARI has maintained a surface mooring, designated M2 at approximately $36^\circ 42' \text{ N } 122^\circ 23.4' \text{ W}$ (Fig. I-1). The mooring serves as a platform for several instruments including a near surface, downward looking RDI ADCP (Fig. II-3). Although a surface mooring introduces “noise” into current measurements due to greater movements caused by waves and currents, a great advantage of M2 is that the data are telemetered to shore and available in near real time.

Different models of ADCP’s were used on M2 for the period 1998-2003. For the period 1998 (year-day 180) to 1999 (year-day 260), MBARI used a workhorse 300 kHz ADCP, configured to resolve currents in 4 m depth bins every 30 minutes. For the period 2000 (year-day 140) to 2001 (year-day 010) a narrow band 150 kHz ADCP was used.

The 150 kHz ADCP was configured to resolve currents in 4 m depth bins every 15 minutes. For the period 2001 (year-day 110) to present, a workhorse long range 75 kHz ADCP was used with a configuration to resolve currents in 8 m depth bins every hour. All data was collected and stored in the OASIS-3 or “Ozone” controller in compact-flash memory. It is then telemetered to shore once an hour via a packet radio station on Mount Toro to MBARI’s Moss Landing facility via a FreeWave radio modem. The “flagging” of bad data was the same as for S2.

Two long gaps exist in the data record (Fig. II-4), one from 1999 (year-day 260) to 2000 (year-day 140), and other in 2001 (from year-day 010 to year-day 110). The determination of the bottom “good” bin for each ADCP deployment was done by inspection as for S2. 20 bins (~11-85 m depth) were satisfactory for deployments in 1998 and 1999 (Fig II-5). For deployments in 2000, 2001, 2002, and 2003, 30 bins were good (~40-200 m depth, Fig. II-5), beyond that point, more than 10% of the data drop out.

C. WINDS AND SEA LEVELS

Sea level data from two tide observation stations, Port San Luis (35° 10.6′N 120° 45.6′W) and Monterey (36° 36.3′N 121° 53.3′W) were used in this study to compute the alongshore sea surface slope. These stations were selected due to their proximity to the moored deployment locations. Hourly tidal observations for the period 1998-2003, were provided by the Hawaii’s Sea Level Data Center. Prior to computation, diurnal and higher frequency signals were removed by using a low pass filter. Sea level difference between Monterey and Port San Luis were calculated for this period.

Wind data measured at 3.5 m above sea level on the M2 mooring was used in this study. Wind data collected at M2 prior to 1996 were not reliable (Mr. Fred Bahr, personal communication) and only data collected in 1996 and later were used. Wind data from NOAA buoy 46042 (Lat. 36.75° N Long. 122.42° W), was used when data at M2 was not available. When both M2 and the NOAA buoy failed, PFEG frictionally adjusted geostrophic winds were used.

Anemometers on M2 were Handar (now VAISALA) sonic anemometer and a R.M. Young anemometer. Wind data was reported from the R.M. Young instrument

every 10 minutes as a 1 minute average. In order to remove high-frequency variability, data was filtered in the same manner as the current observations. Magnetic deviation and variation of the magnetic compass was determined on a survey test bench. Histograms of direction, comparison of measurements with nearby anemometers mounted in buoys and internal and external calibration were performed as a data quality control.

MOORING	INSTRUMENT	INSTRUMENT LEVELS
S2	Upward looking ADCP	300 m
S2	RCM8 current meter	305 m
S2	IRSC Sediment Trap	320 m
S2	RCM8 current meter	1200 m
S2	Honjo Sediment Trap	1205 m

Table II-1. Equipment included at S2. Nominal depth is 1800 m of water at the mooring site.

SETTING No.	START DATE	LATITUDE (N)	LONGITUDE (W)	BOTTOM DEPTH	DATE RECOVERED
1	03/24/98	36° 40.016	122° 22.523	1800 m	08/20/98
2	08/26/98	36° 39.953	122° 22.536	1800 m	01/27/99
3	02/04/99	36° 39.920	122° 22.482	1790 m	07/21/99
4	07/27/99	36° 39.920	122° 22.448	1809 m	01/27/00
5	02/05/00	36° 39.925	122° 22.448	1801 m	07/20/00
6	07/29/00	36° 39.884	122° 22.374	1792 m	01/25/01
7	01/25/01	36° 39.932	122° 22.399	1797 m	08/09/01
8	08/16/01	36° 39.929	122° 22.381	1785 m	02/01/02
9	02/08/02	36° 39.971	122° 22.463	1802 m	08/28/02
10	08/28/02	36° 39.971	122° 22.449	1792 m	03/11/03

Table II-2. Deployments at Mooring S2.

SETTING NUMBER	INSTRUMENT LEVEL	TIMING ERROR
1	295 m	5' 23"
	1194 m	3' 03"
2	303 m	5' 30"
	1199 m	2' 02"
3	305 m	11' 04"
	1185 m	2' 10"
4	293 m	0' 40"
	1172 m	2' 25"
5	294 m	0' 36"
	1173 m	2' 07"
6	308 m	0' 35"
	1176	2' 22"
7	307 m	6' 54"
	1175 m	4' 09"
8	299 m	2' 20"
	1177 m	5' 55"
9	303 m	7' 02"
	1175 m	4' 13"
10	296 m	0' 30"
	1177 m	2' 33"

Table II-3. Timing error for each current meter by deployment at S2.

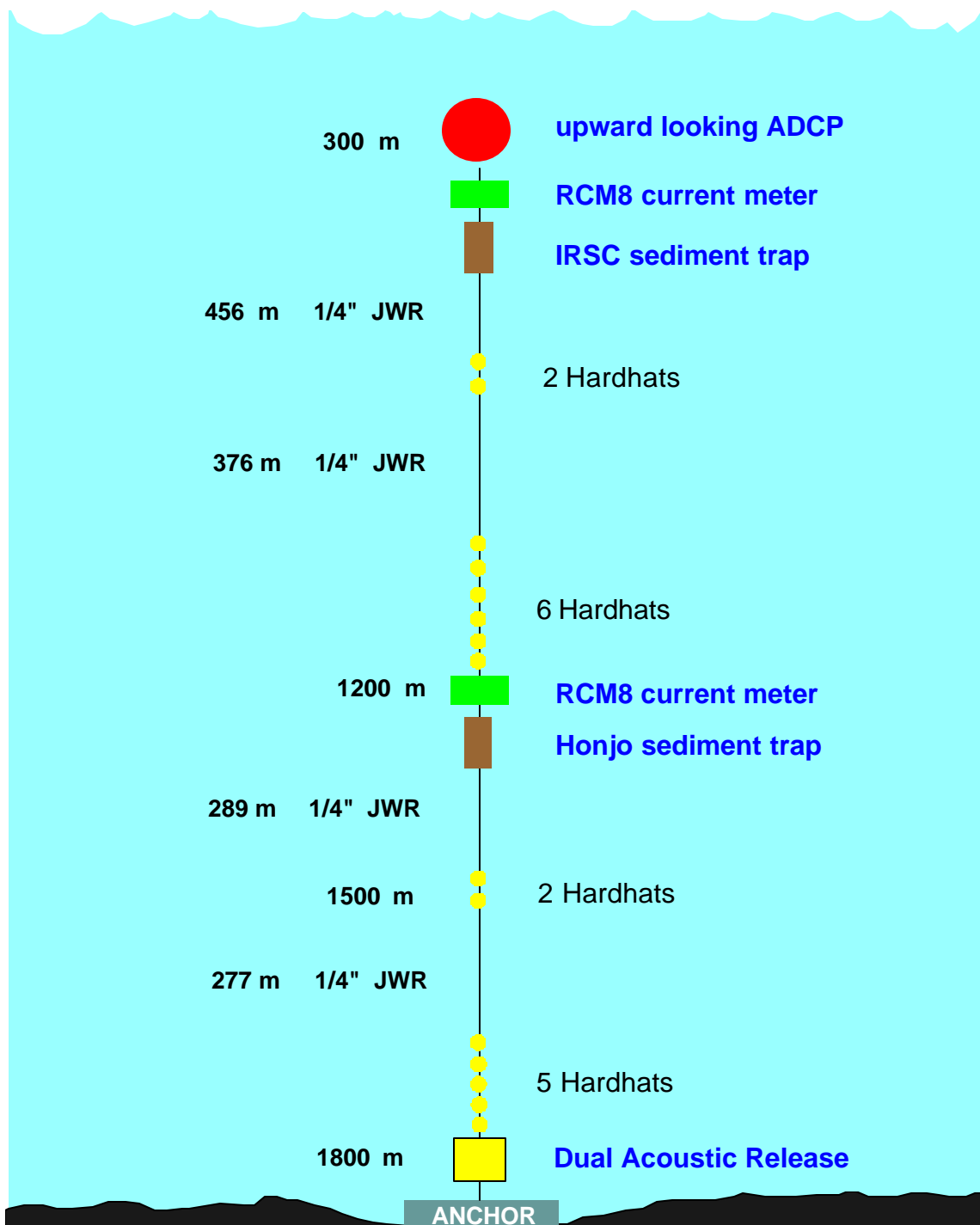


Figure II-1. Schematic diagram of mooring S2. Jacketed Wire Rope (JWR) is a wire designed for oceanographic applications, JWR of 1/4" (3/16") diameter was used in the upper (lower) portion of the array. Hardhats are enclosures that hold glass flotation spheres. A total of 13 hardhats were used in the array.

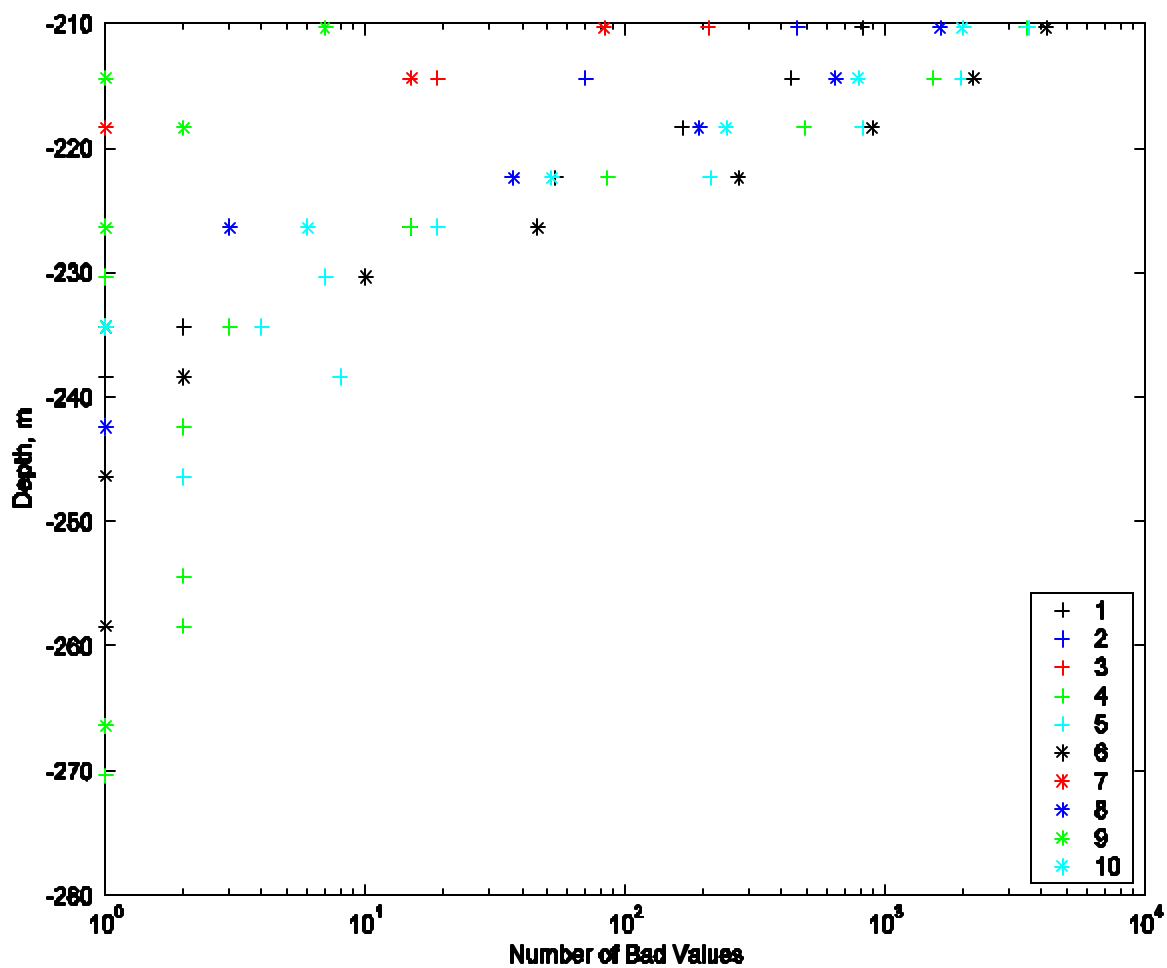


Figure II-2. Plot of depth versus number of bad data for the ADCP at S2. Numbers and corresponding color marks in the legend are the deployment number.

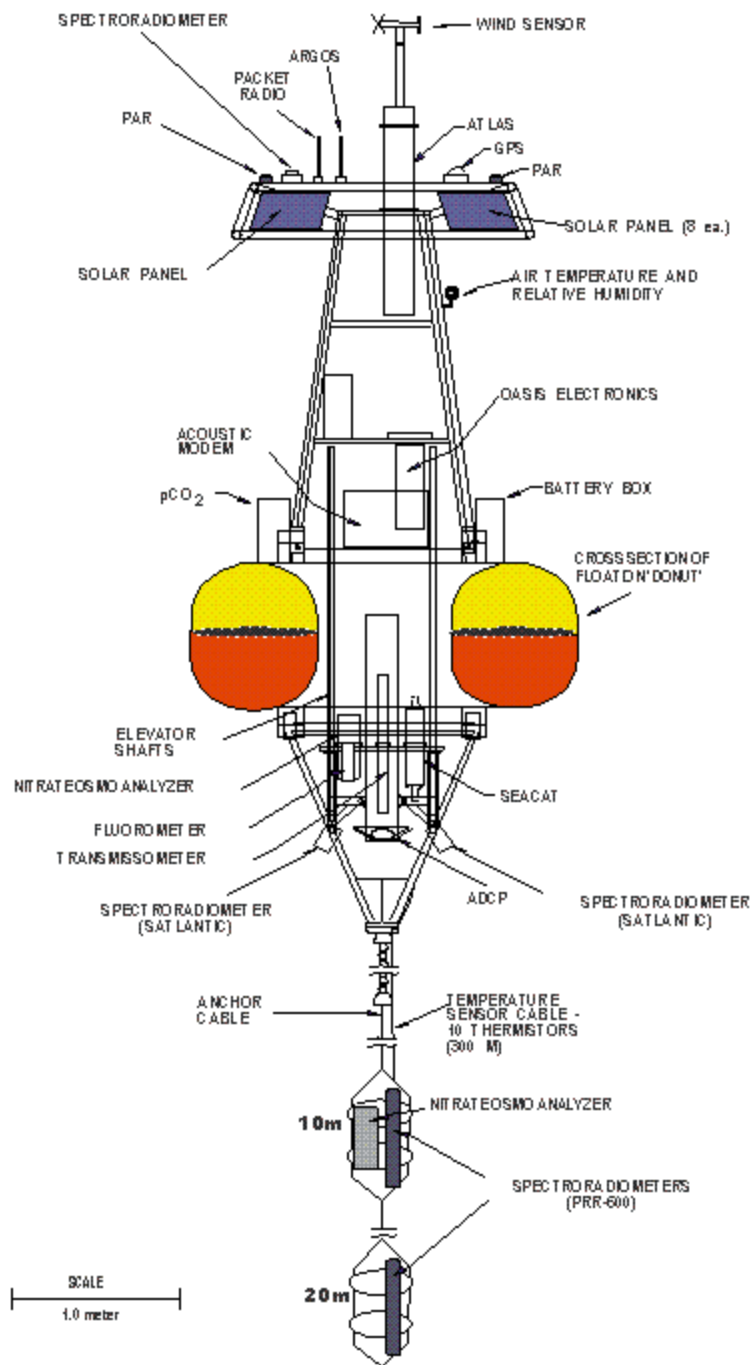


Figure II-3. Schematic diagram of mooring M2.

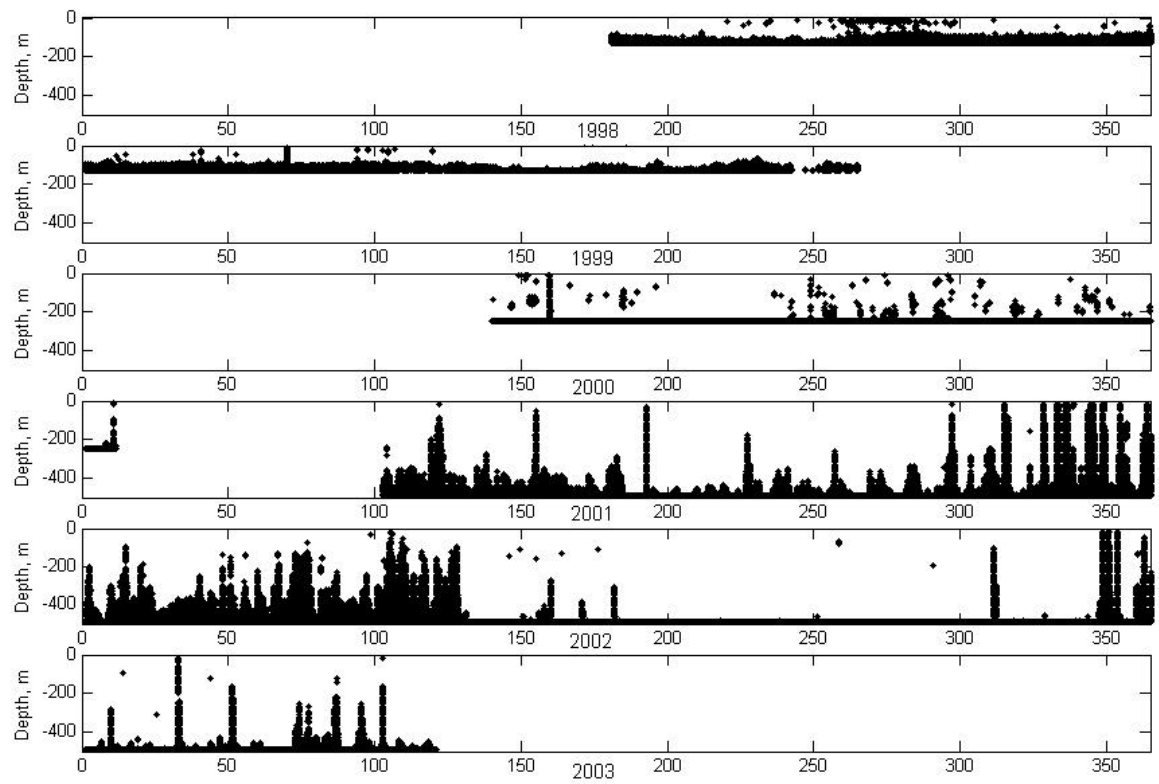


Figure II-4. Time diagram showing ADCP data collection at mooring M2 from January 1, 1998 to March 30, 2003. Black dots show “bad” data flags.

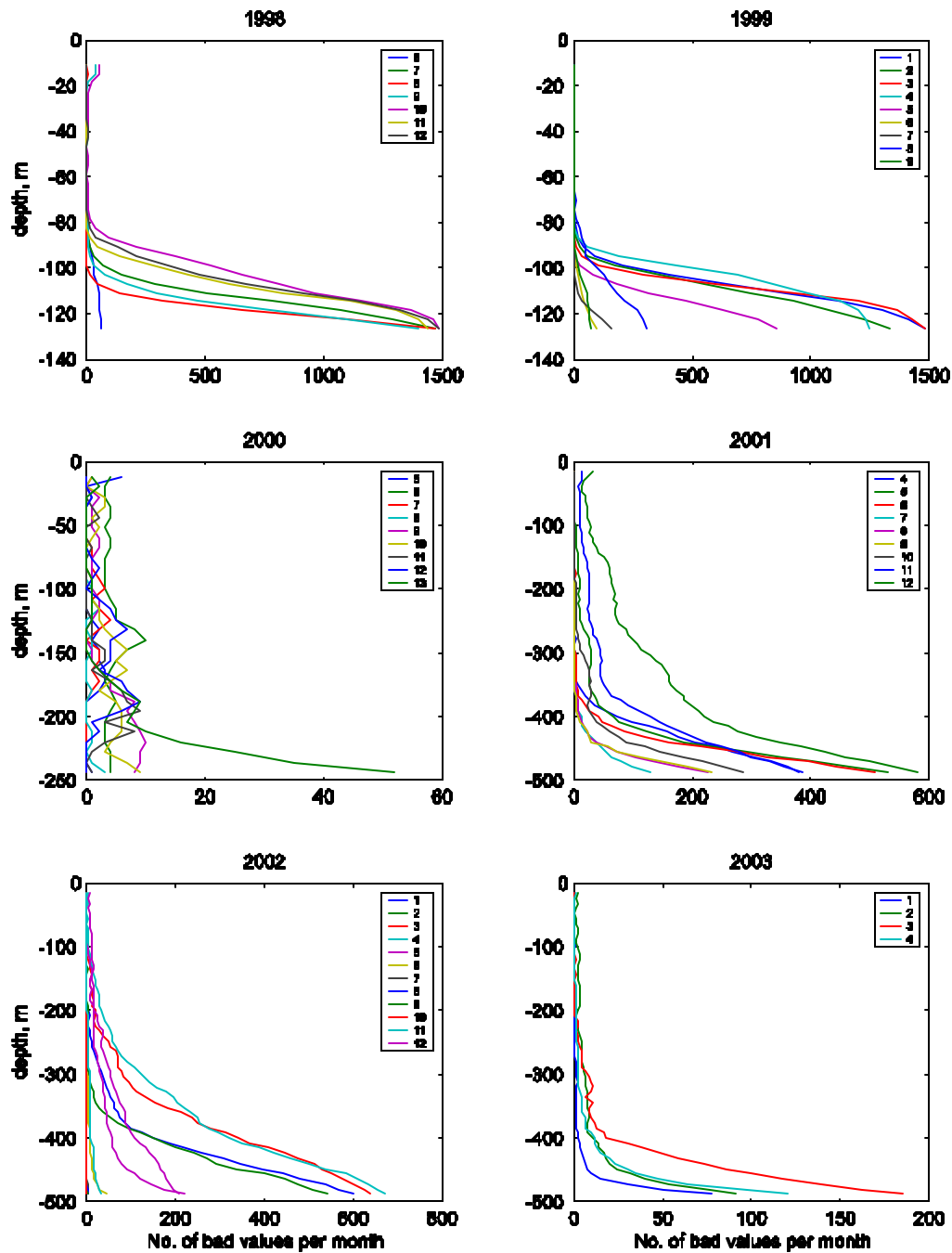


Figure II-5. Plot of depth versus number of bad data for the ADCP at M2. Numbers in the legend indicate month.

THIS PAGE INTENTIONALLY LEFT BLANK

III. RESULTS

Observed currents at S2 are first described using histograms of speed and direction at 305 m and 1200 m depth. Tides are removed from the data set. Mean currents for the entire 5-year set of current observations are computed and variability described using the principal axis rotation. Then seasonal variability of currents is described using averaged time series of currents and temperatures, principal axis rotation, and progressive vector diagrams. Next, mesoscale variability is analyzed using rotary and kinetic energy spectral analysis and empirical orthogonal functions. The vertical structure of the flow is derived by adding S2 and M2 acoustic Doppler current meter results. Finally the statistical relationship between currents and sea level and winds are discussed.

A. HISTOGRAMS OF UNSMOOTHED CURRENT OBSERVATIONS

Histograms of speed and direction for observed 15 minute samples at 290 m for the upward looking ADCP and 30 minute samples at 305 m and 1200 m current meters are shown in Figures III-1. At 290 m the most frequently observed speed was 8 cm s^{-1} , the maximum speed was 47 cm s^{-1} , and 0.03% (64) of observed speeds fell below the 5 mm s^{-1} threshold for the workhorse ADCP. The histogram of direction shows a prevalent northward direction centered at 340°T . At 305 m, the most frequently observed speed was 6 cm s^{-1} , the maximum speed was 51.4 cm s^{-1} , and 5.2% (3790) of observed speeds fell below the 2 cm s^{-1} threshold for the RCM-8 current meters. The histogram of directions shows that northward flow dominated at 305 m as 47% of the current direction fell between 293°T and 31°T .

The histograms for the RCM-8 current meter at 1200 m are also shown in Figure III-1. 24.4% (17703) of the observed speeds were less than the threshold for the paddlewheel, 2 cm s^{-1} , and are not shown in the plot. Above 2 cm s^{-1} the most frequently observed speed was 5 cm s^{-1} and the maximum speed was 24.4 cm s^{-1} . The direction histogram shows two broad peaks, with the most prevalent direction being to the south, centered at 164°T , with the smaller peak located in nearly the opposite direction.

Since the focus of this thesis is on subtidal variability, the 30-minute current meter data were smoothed using the low pass filter described in the previous section to remove diurnal and higher frequency tidal and inertial period currents. Results of tidal analyses are included in Appendix A and indicate that maximum tidal velocities were associated with the lunar semidiurnal (M_2) tide, 1.0 cm s^{-1} . The smoothed data were then decimated to 6-hour intervals for the analyses described below.

B. MEANS, VARIANCES, AND INTEGRAL TIME SCALES

Observed currents at a given depth are represented as $U(t) = [u(t), v(t)]$, where u is the east-west component and v is the north-south component. The fluctuating portion of the flow is obtained by removing the mean,

$$U'(t) = U(t) - \langle U(t) \rangle = [u'(t), v'(t)],$$

where $u' = u - \langle u \rangle$, $v' = v - \langle v \rangle$, and $\langle \rangle$ indicates time averaging over the five year period. At 305 m (1200 m), the mean current was directed toward 334°T (169°T) at 3.9 cm s^{-1} (0.8 cm s^{-1}).

For a vector time series, the variance includes $\langle u'^2 \rangle, \langle v'^2 \rangle, \langle u'v' \rangle$. To eliminate the cross correlation terms, the axes are rotated so that the maximum variance lies along the major axis of the variance ellipse. This is referred to as a “principal” axis rotation (Emery and Thomson, 1997), and the orientation of the principal axis, \mathbf{q} , is found by

$$\mathbf{q} = \frac{1}{2} \tan^{-1} \left[\frac{2\langle u'v' \rangle}{\langle u'^2 \rangle - \langle v'^2 \rangle} \right].$$

In the new coordinate system, the rotated velocity components are defined as

$$u_r = u' \cos \mathbf{q} + v' \sin \mathbf{q}$$

and

$$v_r = -u' \sin \mathbf{q} + v' \cos \mathbf{q}.$$

In this coordinate system, the maximum amount of data scatter (maximum variance or standard deviation) is associated with the major axis (v_r), while the minimum amount of data scatter is associated with the minor axis (u_r). The utility of the principal axes are that they determine the orientation of the variability of the flow at any current meter site and decompose the velocity into uncorrelated scalar components (Emery and Thompson, 1997, Denbo et al., 1984).

At S2, the major axis at 305 m (1200 m) was directed toward 349°T (350°T), the length of the semi-major axis was 9.4 cm s⁻¹ (3.4 cm s⁻¹) and the length of the semi-minor axis was 5.8 cm s⁻¹ (2 cm s⁻¹). Figure III-2 (Fig. III-3) shows the mean currents at 305 m (1200 m), the standard deviation ellipse, and the scatter of individual 6-hour current observations. For coastal and near-bottom currents, the bathymetry usually controls both the direction of the flow and the principal axis. Figure III-4 shows details of the local bathymetry near the mooring site. The 1400-1600 m isobaths, just to the east of the mooring site, are oriented in the same direction as the mean flow and principal axis of the 1200 m flow at S2. This direction also coincides with the orientation of the principal axis at 305 m but the mean flow at 305 m was directed more to the west, similar to the orientation of the deeper isobaths at the mooring site.

Statistics (mean current speed and direction, principal axis orientation, and semi-major and semi-minor axis) were also computed for the 6-hour, smoothed current meter data at 305 m and 1200 m for each six-month deployment of S2 (Table III-1). Mean temperature and pressure and their standard deviations are also included in Table III-1. At 305 m depth, the mean flow was northward and westward for all but deployments 4 and 10 when the flow was southward. Mean speeds at 305 m for each deployment ranged from 1.2 cm/s for deployment 2 to 7.0 cm/s for deployment 9, a factor of five. Semi-major (semi-minor) axes ranged from a maximum of 11.8 cm/s (7.4 cm/s) for deployment 10 (5) to a minimum of 7.2 cm/s (3.6 cm/s) for deployment 2 (2). The ellipse orientation at 305 m ranged from almost due north (002.6°T) for the first deployment to west-north-west (304.4°T) for deployment 5. The effects of seasonal and interannual variability will be considered below, but it is clear that variability from deployment to deployment was large.

At 1200 m depth, the mean flow was southward for all but deployments 2 and 6, and the mean flow was eastward for six of the ten deployments. Mean speeds at 1200 m for each deployment varied by a factor of ten, from 0.2 cm/s for deployment 6 to 2.4 cm/s for deployment 10. The standard deviations represented by the ellipse half axes varied by a factor of two: the semi-major (semi-minor) axes ranged from a maximum of 4.2 cm/s (2.9 cm/s) for deployment 10 (6) to a minimum of 2.3 cm/s (1.3 cm/s) for deployment 3 (4). The ellipse orientation at 1200 m ranged from almost due north (14.7°T) for the third deployment to north-northwest (337.3°T) for deployment 9, a range of 37.4° vs. 58.2° at 305 m.

Temperature usually decreases with increasing pressure at S2 so minimum temperature should correspond to maximum pressure and vice-versa. The former was observed, but the latter was not. Although the pressure at a fixed level was expected to vary from deployment to deployment due to differences in the depth of the anchor, the pressure difference between the two meters should remain constant, 885 dbar, if the mooring is vertical. The mean pressure difference between the current meters was 882 dbar and varied 24 dbar from a minimum of 874 dbar to a maximum of 898 dbar. The elasticity of the mooring wire is close to zero, so the difference (13 dbar) between the maximum observed pressure, 898 dbar, and the pressure difference fixed by the length of the wire, 885 dbar, was clearly an error and was consistent with the manufacturer's specification for the accuracy of the pressure gauges, ± 6 dbar at 1200 m and ± 1 dbar at 305 m.

The integral time scale T^* , is the sum of the normalized autocorrelation function

$$r_{yy}(t) = \frac{C_{yy}(t)}{S^2}$$

over the length $L = N\Delta t$ of the time series

$$\begin{aligned} T^* &= \frac{\Delta t}{2} \sum_{i=0}^{N'} [r(t_i) + r(t_i + 1)] \\ &= \frac{\Delta t}{2S^2} \sum_{i=0}^{N'} [C(t_i) + C(t_{i+1})] \end{aligned}$$

where r_{yy} = autocorrelation function, t = lag time, C_{yy} = autocovariance function, s^2 = variance, L = length of the time series, $N \Delta t$ = number of lag steps (Emery and Thomson, 1997). The integral time scale is a measure of the period of the process that dominates a given time series. The integral time scales for flow along the major and minor axes at 305 m were 6 and 4 days respectively, and are shown in Figure III-5. At 1200 m, integral time scales for flow along the major and minor axes was 7.5 and 4 days, respectively. For temperature at 305 m and 1200 m, the integral time scale was 31 days.

C. CURRENT AND TEMPERATURE TIME SERIES

Time series of daily currents measured at 305 m and 1200 m are shown as stick plots in Figures III-6 and III-8, respectively, and time series of temperature at 305 m and 1200 m are shown in Figures III-7 and III-9, respectively. At 305 m, the stick plot (Fig. III-6) showed a burst of strong (> 20 cm/s) poleward flow in the spring which followed a late winter period of weak flow. This occurred in May-June in every year but 2001 when the strong flow occurred in March. This strong poleward flow in late spring will be referred to as the “spring jet”. Subsequent to the spring jet, additional bursts of poleward flow were observed, separated by periods of current reversals or relaxation. The timing and pattern of these additional bursts varied widely. In 1998, the spring jet lasted for about one month, the flow reversed direction in late June, and weaker bursts occurred in mid July and early August. In 1999, the spring jet was about two weeks long and was followed by two bursts of similar duration at about monthly intervals. In 2000, the spring jet resembled that in 1998, but subsequent bursts of poleward flow occurred at two month intervals. In 2001, the first three bursts of poleward flow associated with the spring jet occurred at about 2 month intervals but unlike other years, moderate to strong (10-20 cm/s) poleward flow was observed from late August to September. In 2002, the bursts of poleward flow that occurred in late July and mid-September were stronger than the initial burst in late March to mid June as well as stronger than poleward bursts seen during this time in previous years, and, as in 2001, strong poleward flow was also observed in November.

Although poleward flow dominated the 305 m stick plot, periods of equatorward flow occurred 4-9 times per year. A few of these were as strong as the springtime poleward bursts (> 20 cm/s). The first period of strong equatorward flow occurred in October 1999, and subsequent strong bursts were observed in August 2000 and October 2002, the latter representing the strongest equatorward flow registered. Sustained equatorward flow of 10-20 cm/s was also seen in January 2003.

The 305 m temperature time series (Fig. III-7) showed a distinct seasonal pattern although significant changes occurred from year to year. At this depth, temperature changes were largely due to vertical movement of isopycnals due to acceleration of the alongshore flow. The coolest temperatures are typically observed between April and June and maximum temperatures from August through early November. Temperature oscillations which were almost as large as the seasonal cycle also occurred. A number of these are associated with the bursts of poleward (equatorward) flow and temperature warmed (cooled) as the poleward (equatorward) flow accelerated. But some exceptions to this occurred, for example during the equatorward burst of flow in October 2002, temperature remained relatively warm

The relationship between the direction of alongshore flow and temperature, cooling (heating) associated with equatorward (poleward) flows, can be seen by examining the time series for a specific year. For instance, in 1999 during spring the temperature cooled from 7.8°C to 6.7°C from early January to mid April, with flow speed of 21 cm s^{-1} and poleward direction through mid January, offshore direction in late January and poleward direction through February and April. The spring jet developed around April 14 and extended until early July, with maximum velocities of 26 cm s^{-1} , accompanied by warming from 6.7°C in late April, to 7.7°C in late July, remaining warm. The spring jet was interrupted twice by equatorward and offshore flow on May 17 and June 3. This offshore flow coincided with the decreased temperature from a maximum of 7.3°C and 7.5°C to a minimum of 6.7°C and 6.8°C , respectively.

The strength of the currents and the variability of temperature decreased at 1200 m. The stick plots at 1200 m (Fig. III-8) showed weak flow through the first third of the year with stronger currents developing later in the year. The spring jet did not exist at

1200 m although weak poleward flow sometimes coincided with the 300 m poleward jet, e.g. late May 2000. During the last three months of the year, the flow at 1200 m was often as strong or stronger than the flow at 305 m. A number of the stronger equatorial flows (August 1999, July 2000, and December 2002) exceeded those observed at 305 m. This suggests that the poleward flows were surface enhanced while a number of the equatorward flows were bottom trapped.

The 1200 m temperature time series (Fig. III-9) did not show a clear annual oscillation. Minimum (maximum) temperatures occurred in April (November), October (May), September (July), November (October) and June (September) in 1998, 1999, 2000, 2001 and 2002 respectively. Springs were characterized by decreasing temperatures followed by temperature increases but these temperature excursions were often exceeded by subsequent cooling and warming. Cooling was generally associated with equatorward acceleration of the 1200 m current (Fig. III-8).

D. SEASONAL VARIABILITY

Seasonal cycles were constructed by sorting current and temperature data by the day of the year and then averaging the resulting five-days of data (one day for each year of the five-year time series). Results for currents and temperature at 305 m and 1200 m are shown in Figure III-10. The annual cycle of temperature at 305 m showed the clearest annual signal. The temperature minimum, 6.7°C, occurred on April 29 and three months later on July 29 the temperature was maximum, 8.0°C. Subsequent to July 29, the trend of the 305 m temperature was decreasing but with excursions of $\pm 0.3^\circ\text{C}$. In early March, the rate of cooling increased. The seasonal variability of velocity at 305 m showed strong poleward flow (10 to 20 cm/s) while the temperature increased from April 29 to July 29, weaker poleward flow with some current reversals from August through February, and weakest flow during late March and early April.

The temperature at 1200 m showed a pattern similar to that at 305 m only during the period from March through early June. Temperatures decreased from 3.6°C on March 1 to 3.43°C on April 22 (a week earlier than the minimum temperature at 305 m) and then warmed to 3.6°C on June 11. Subsequent to June 11, the temperatures remained

near 3.55°C when they decreased to the seasonal minimum, 3.39°C, on October 22. The principal feature of the 1200 m velocities occurred during the June 11 to October 22 as southward velocities greater than 5 cm/s. Subsequent to October 22, temperatures increased again to 3.6°C on March 1.

Daily data were used to compute monthly means and velocity ellipses. At 305 m means were toward the north (Fig. III-11, Table III-2) for each month except October when the flow was toward the south due to the two strong southward flows observed in 1999 and 2002 described above. The mean flow was also directed along NW-SE except in January when it was offshore and March when it was onshore. The orientation of the major axes varied from 329° in March to 012° in June. In April, May and June the ellipses were nearly circular and in other months the semi-major axis was about twice the semi-minor axis. During May and June, the mean current (10.5 cm s⁻¹ and 10.4 cm s⁻¹, respectively), were larger than the magnitude of the semi-major axis. Currents were twice as variable during the period from June through October than they were from November to May.

At 1200 m (Fig III-12, Table III-3), the monthly means were a fraction of the length of the semi-major axis except in August when the mean speed, 3.3 cm/s, exceeded the semi-major axis, 2.9 cm/s. Monthly means were southward in every month but May, but their direction strayed widely from the trend of the local bathymetry. In contrast, the direction of the major axis varied less than at 305 m, from 336° in August to 003° in May. Ellipse dimensions at 1200 m were about half those at 305 m. As at 1200 m, currents were least variable during April and most variable in October. The semi-minor axis was about half the size of the semi-major axis except in June when the ellipse was nearly circular (as it was at 305 m in June). Currents were twice as variable from June through December than they were from January through May.

Progressive vector diagrams (PVDs) were constructed for each month to visualize the monthly displacements caused by the currents. They were calculated by integrating the velocity from the beginning of the month, 0, to the end of the month, T,

$$x(t) = \int_0^T u(t)dt, \quad y(t) = \int_0^T v(t)dt.$$

The resulting paths begin at the origin and look like trajectories. PVDs would only represent trajectories if the velocity field was spatially homogeneous and the flow was accelerated at the same time and rate at all locations.

The monthly PVDs at 305 m are shown in Fig. III-13. They cover an area which was two to six times larger than those for 1200 m. The PVDs show clearly the predominantly northwestward direction flow in all months except October. For October, the strong southward flow in October 2002 resulted in a southward displacement of more than 400 km, the largest displacement observed at 305 m. In October, flow was also southward in 1999 but was northward in other years. Displacements seen in May and June and August showed more than 300 km of northward displacement, confirming the strong poleward flow seen in means and ellipses described above. The April PVD for 305 m showed a remarkable year-to-year change in the mean flow direction. Although some onshore flow occurred in March 1999, 2000 and 2002, the net eastward flow for the mean was clearly the result of southeastward flow in 2002. Eddy-like features occurred in the PVDs for June, July, August, and September.

The PVD's at 1200 m (Fig. III-14) showed predominantly southeastward displacement except in May when displacements were northwestward except in 1999. Largest displacements were associated with southwestward flow in July and August 2000 and October 2002. Anticyclonic features occurred in June, July and September. In June, eastward, southeastward, southward and westward displacements were seen in different years. Eastward displacements of about 50 km, not associated with southward flow, were seen in March, June, and October.

E. MESOSCALE VARIABILITY

Current meter data at 305 m and 1200 m were daily averaged and a 7 day filter used to remove high frequency variability. The alongshore and onshore (u, v) components of velocity were used to calculate the monthly means ($\langle u \rangle, \langle v \rangle$) and variances ($\langle u'^2 \rangle, \langle v'^2 \rangle$) where the overbar signifies monthly averages, and a prime superscript indicates the deviation from the mean. Eddy kinetic energy (EKE) was calculated as

$$K_E = 0.5(\langle u'^2 \rangle + \langle v'^2 \rangle).$$

Figure III-15 and III-16 show the monthly average for the eddy field and error bars (one standard deviation) for $\langle u'^2 \rangle, \langle v'^2 \rangle$ and $\langle u'v' \rangle$ at 305 m and 1200 m. At 305 m most of the contribution to the total EKE comes from the along-shore component which had large variability during June and October as described above. The maximum EKE was $38 \text{ cm}^2/\text{s}^2$ in October and minimum was $4 \text{ cm}^2/\text{s}^2$ in December. At 1200 m the along-shore component also contributed the most to the total EKE with the largest uncertainties in July. The maximum value of EKE at 1200 m was $5 \text{ cm}^2/\text{s}^2$ in July and was minimum, $0.4 \text{ cm}^2/\text{s}^2$, in February.

Rotary and kinetic energy spectra were used to determine how the variance of the time series was distributed over frequency. Analysis was performed using Matlab™ programs, which are based on the discrete Fourier transform and the periodogram method. A Hanning window was applied with a 50% overlap. As is usual practice, the mean and trend of the time series were removed before analysis. A description of the mathematical procedure for calculation of rotary spectra is given in Appendix B.

Figure III-17 shows the clockwise (CW) and counter-clockwise (CCW) rotary components at 305 m and 1200 m. The energy spectra of the currents at 305 m showed that currents were more rectilinear (i.e. neither CW nor CCW components were dominant). An energy peak occurred at low frequency, 0.019 cpd (~52 days), where CCW was dominant. At 1200 m there was clear dominance of CW component at low frequencies, with peak energy at 0.018 cpd (~56 days). At all frequencies, the energy level at the shallower current meter was five times greater than at 1200 m depth.

Kinetic energy spectra at both 305 m and 1200 m (Fig. III-18) showed energy peaks at the same low frequencies as the rotary spectra. The 305 m kinetic energy spectra had three large peaks at 0.03 cpd (~33 days), 0.07 cpd (~14 days) and 0.11 (~9 days). At 305 m there was a reduction of kinetic energy at high frequencies (periods less than ~9 days) as well as lower frequencies (periods greater than ~52 days), while at 1200 m energy decreased at periods less or greater than 59 days, respectively. At 1200 m, the peak energy density at .018 cpd, $1050 (\text{cm/s})^4 \text{ day}^{-1}$, exceeded that at 305 m, $750 (\text{cm/s})^4$

day⁻¹, but at other frequencies, the eddy kinetic energy spectrum at 1200 m had about 5-10 times less energy density than at 305 m. A series of smaller energy peaks occurred at 1200 m but only one was at the same frequency, 0.03 cpd, as 305 m.

F. VERTICAL STRUCTURE

Mean velocity and variance ellipse parameters for the 300 m BBADCP on S2 and the downward looking surface ADCP on M2 are shown in Figure III-19 and are listed in Table III-4 along with the current meter results given above. From 16-40 m, the mean flow at M2 (Fig. III-19a) became more northward with depth, changing direction from 281° to 346°, in a manner consistent with Ekman flow. The speed was also consistent with Ekman flow between 16 and 24 m, decreasing from 2.4 to 2.2 cm/s, however below the minimum at 24 m, the speed of the mean flow increased to 4.2 cm/s at 88 m. The mean flow was most northward at 40 m and gradually rotated 8° counter clockwise with depth so that flow was north-northwestward at 88 m. The S2 BBADCP (Fig. III-19b) showed the mean flow directed in the same direction at 210 m as was observed at M2 at 88 m, but the mean speed was 1.1 cm/s greater. From 210 m to 290 m, the mean speed at S2 decreased from 5.3 cm/s to 3.9 cm/s and the direction of the speed continued the westward trend with depth, changing from 338° to 334°. The increase of speed with depth seen at M2 and the decrease of speed below 210 m at S2 imply the existence of a speed maximum between 88 m and 210 m which was not observed. This speed maximum is associated with the CU and was observed to lie at a depth of 150 m in velocity soundings at a nearby location. (Data from the M2 ADCP show that the speed of the mean current was maximum, 6.4 cm/s, in 2002 at 112 m.) The shear measured by the S2 BBADCP, -1.2 cm/s in 72 m, was -1.6×10^{-2} cm/s-m, and compares well to -2.0×10^{-2} cm/s-m measured by RAFOS floats (Garfield et al 1999) and -1.6×10^{-2} cm/s-m measured by an acoustically tracked dropsonde (Rischmiller, 1993). Taking this shear into account, the mean speed and direction at 305 m measured with the RCM8 agreed well with extrapolations from the BBADCP at 290 m.

The velocity ellipse statistics were also remarkably consistent. At M2 (Table III-4), the direction of the semi-major axis varied from 339° to 345°, and the semi-major axis varied from a minimum of 13.0 cm/s to a maximum of 14.28 cm/s at 88 m and the ratio

of the semi-major and semi-minor axis was 1.4. Between 210 m and 290 m at S2, the direction of the semi-major axis was 348° or 349° and the ratio of the semi-major and semi-minor axis was 1.6. The maximum semi-major axis at S2 was 11.5 cm/s at 210 m and this decreased steadily with depth to 3.4 cm/s at 1200 m.

Momentum empirical orthogonal functions (EOF) (also called principal component analysis) were utilized to determine patterns of temporal and spatial variability of the horizontal currents. This technique was described by Chereskin et al. (2002) and is used to decompose space-time distributed data into modes ranked by their percentage of variance. The modes or EOF's can be defined as those patterns which are most powerful in explaining the variance of the data set. Each mode or EOF consists of a dimensional spatial pattern function (Z-scores) that is uncorrelated with other modes, a time series of amplitude coefficients that show how a given principal component varied with time, and an associated percent of the total variance. Generally the first three principal components account for about 80-90% of the total variability.

Days which contained daily averaged currents at each depth in Table III-4 were used to calculate the EOFs for the M2/S2 velocity observations. The three modes shown in Figure III-20 accounted for a total of 90% of the variance. The first Z-score accounted for 75% of the variance and represented flow along the principal axis, to the northwest for positive principal components (except at 1200 m where the flow was to the southwest). The second Z-score accounted for 9% of the variance and had $u \sim 0$ and v to the south at M2 and north at S2 (including 1200 m) for positive principal components; this pattern might be called an undercurrent vs. Davidson Current mode. The third Z-score accounted for 6% of the variance and had $v \sim 0$ and u to the east at M2 and to the west at S2 for positive principal components and might be thought of as an upwelling mode.

The temporal variability of the first three principal components is shown in the lower portion of Figure III-20 as a function of yearday (left) and year (right). Considerable variability occurred in the principal component scores. The second principal component had the strongest seasonal pattern; the biharmonic fit was maximum on yearday 125 and minimum on yearday 360. This corresponds to the pattern of DC vs.

undercurrent flow described by previous authors. The biharmonic fit to the first mode was minimum on yearday 85, crossed zero on yearday 150 and was maximum on yearday 190, resembling the pattern of seasonal flow at 300 m described above. The biharmonic fit to the third principal component was positive from yearday 90 to yearday 205. Since this is the period when upper layer flow is expected to be offshore, this is opposite to what would be expected from an upwelling mode. The temporal variation of the principal component scores as a function of year contains a number of gaps which correspond to periods when there was no data available at M2. Subsequent to 2001, a clear seasonal cycle was apparent for the first two modes.

G. STATISTICAL RELATIONSHIP BETWEEN CURRENTS AND SEA LEVELS AND WINDS

The relationships between currents, sea level, and wind stress were studied by means of spectrum analysis. The linear response of the output of a system, y , to an input (forcing), x , may be written in terms of a complex transfer or frequency response function, \mathbf{H}_{xy} ,

$$\mathbf{H}_{xy}(f) = \mathbf{G}_{xy}(f) / \mathbf{G}_{xx}(f), \text{ so } \mathbf{G}_{xx}(f) = \mathbf{H}_{xy}(f) \mathbf{G}_{yy}(f)$$

where \mathbf{G}_{xy} is the cross spectrum of x and y , \mathbf{G}_{xx} is the spectrum of x , and \mathbf{G}_{yy} is the spectrum of y (Bendat and Piersol, 1986). Note that \mathbf{H}_{xy} has a magnitude and an associated phase angle for each frequency estimate.

The relationship between adjusted sea level, η , and alongshore velocity, v_r , is approximated by geostrophic balance,

$$v_r = \frac{g}{f} \frac{\partial \eta}{\partial x} \approx \frac{g}{fL} \eta$$

where g is gravitational acceleration, f is the Coriolis parameter, and L is the current width. Then $|\mathbf{H}_{v_r \eta}| \approx \frac{g}{fL}$, e.g. the width of the alongshore geostrophic current can be estimated from the amplitude of the transfer function between the alongshore velocity and adjusted sea level (Collins, 1968).

Figure III-21 shows the relationships between the spectrums of alongshore and across shore currents at 305 m and 1200 m and adjusted sea level, respectively. The transfer functions were noisy with changes in amplitude and phase between adjacent frequency bins that were usually physically impossible. Frequency bands for which the phase was relatively steady and coherence high did occur. The phase between adjusted sea level and alongshore velocity was close to zero for frequencies including 0.01-0.03, 0.10-0.14 and 0.15-0.19 day⁻¹. The coherence between across shore velocity and adjusted sea level was greater than that for alongshore velocity, exceeding 0.5 at 0.005, 0.015, and 0.1 day⁻¹; phases at these frequencies were about -p and the amplitude of the transfer function was about the same as that for the alongshore velocity. At 1200 m, the phase between adjusted sea and alongshore (across shore) velocity was close to zero (-p), the coherence greater than 0.4 (0.4) and the current width about 11 (12) km for frequencies greater than 0.2 day⁻¹.

The rate of change of the alongshore horizontal pressure gradient was approximated by subtracting the ASL at Monterey from the ASL at Port San Luis (the location of the sea level gauges is shown in Fig. I-1). The transfer function between the fluctuating horizontal pressure gradient and currents at S2 is shown in Figure III-22. As in Fig. III-21, the transfer functions were noisy. For alongshore flow at 305 m, the largest transfer function (coherence) was 4 s⁻¹ (0.58) at 0.04 day⁻¹ and with a phase of about p, e.g. an elevation of ASL at Port San Luis of 1 cm relative to Monterey will result in a 4 cm/s alongshore flow at S2 about 12 days later. For across shore flow at 305 m, the largest coherence was 0.59 at 0.11 day⁻¹ and the phase at this frequency was close to zero. At 1200 m, highest coherences, 0.59, occurred at 0.23 day⁻¹ for both the alongshore and across shore velocity with a phase of p and 0, respectively. The amplitude of the transfer function at 1200 m was about half that at 305 m.

The transfer functions between wind stress vs. currents at S2 is shown in Figure III-23. For wind stress vs. 305 m currents, the largest transfer function amplitude (>1.5x10⁵) was at frequencies of 0.014, 0.04, 0.05, and 0.065 day⁻¹ with counterclockwise component dominating at those frequencies. At frequency of 0.13 day⁻¹ clockwise component dominated, although the amplitude transfer function was less than 1x10⁵. For

wind stress vs. 1200 m currents, counterclockwise component dominated at frequencies of 0.027, 0.07, and 0.16 day⁻¹, although amplitudes at those frequencies were less than 0.25 except at frequency of 0.16 that showed a value of 0.3.

Setting No.	Depth m	Mean		Semi-Major Axis		Semi-Minor Axis	Temperature		Pressure	
		Speed cm s ⁻¹	Direction °T	Direction °T	Magnitude cm s ⁻¹	Magnitude cm s ⁻¹	Mean °C	S.D.	Mean	S.D.
1	305	4.9	345	002.6	8.4	5.7	7.53	0.59	295	0.11
	1200	1.1	149.8	344.2	2.5	1.7	3.39	0.06	1195	0.33
2	305	1.2	335.3	336.8	7.2	3.6	7.46	0.33	303	0.34
	1200	0.6	321.5	346	2.7	1.5	3.38	0.05	1199	0.001
3	305	6.9	333.6	357	9.0	5.6	7.09	0.25	308	0.62
	1200	0.4	237.2	014.7	2.3	2.1	3.54	0.05	1186	0.24
4	305	2.3	149	341.1	7.6	3.7	7.52	0.31	293	0.37
	1200	1.1	167.4	339.1	3.2	1.3	3.43	0.06	1172	0.005
5	305	6.4	331.3	304.4	7.8	7.4	7.33	0.42	295	0.47
	1200	1.0	155.3	350.5	4.1	1.7	3.58	0.08	1173	0.66
6	305	3.0	312.7	352.1	10.2	5.4	7.57	0.26	308	0.34
	1200	0.2	307.3	353.9	4.1	2.9	3.43	0.07	N/A	N/A
7	305	6.5	347.9	331.5	8.2	4.9	7.34	0.27	307	0.39
	1200	0.8	199.4	013	2.9	2.0	3.54	0.06	1175	0.17
8	305	6.7	352	306	6.3	6.1	7.69	0.31	298	0.43
	1200	1.2	159.3	002.1	2.7	1.9	3.52	0.05	1177	0.32
9	305	7.0	332.4	341.2	10.2	7.1	7.69	0.31	298	0.43
	1200	1.1	151.1	337.3	3.3	2.2	3.52	0.08	1175	0.36
10	305	3.0	232.9	358.5	11.8	4.9	8.13	0.33	296	1.55
	1200	2.4	167.1	355.1	4.2	1.9	3.49	0.11	1177	0.74

Table III-1. Statistics for the 6-hour, detided current meter data at 305 m and 1200 m for each six-month deployment of S2. Red (blue) quantities are maximum (minimum) values.

Month	Mean Speed cm s⁻¹	Standard error of the mean	Mean Direction	Semi- Major Axis Direction	Semi- Major Axis Magnitude cm s⁻¹	Semi- Minor Axis Magnitude cm s⁻¹
January	1.7	0.1969	286.8	345.8	9.6	4.3
February	3.9	0.1527	330.3	351.0	5.8	2.8
March	2.5	0.2219	42.9	329.1	7.4	3.9
April	1.7	0.1429	332.7	349.4	4.6	4.2
May	10.5	0.1995	340.8	350.9	6.8	5.8
June	10.4	0.2746	329.2	011.6	10.3	8.9
July	6.2	0.2676	329.1	354.7	10.1	6.9
August	4.3	0.2665	335.3	000.5	11.7	6.9
September	5.1	0.2544	318.2	346.0	10.8	4.6
October	3.0	0.2922	172.4	006.8	11.9	6.2
November	3.3	0.1463	345.4	337.3	7.1	4.2
December	2.2	0.1287	353.0	334.7	5.4	3.7

Table III-2. Monthly mean currents at 305 m depth.

Month	Mean Speed cm s⁻¹	Standard error of the mean	Mean Direction	Semi- Major Axis Direction	Semi- Major Axis Magnitude cm s⁻¹	Semi- Minor Axis Magnitude cm s⁻¹
January	0.8	0.0648	113.6	352.6	2.9	1.7
February	0.8	0.0513	183.5	348.6	2.2	1.3
March	1.2	0.0841	120.5	349.8	2.6	2.0
April	0.1	0.0481	212.0	339.9	1.9	0.9
May	0.9	0.0717	326.8	002.7	2.7	1.5
June	2.0	0.0903	180.5	357.6	3.4	3.1
July	1.4	0.0920	167.4	354.6	3.9	2.3
August	3.3	0.0663	159.7	335.8	2.9	1.6
September	0.5	0.0783	253.0	346.6	3.5	1.8
October	1.1	0.0928	201.8	344.8	4.0	2.2
November	0.3	0.0928	182.1	358.0	3.9	1.6
December	1.1	0.0963	158.6	000.7	3.7	2.4

Table III-3. Monthly mean currents at 1200 m depth

Mooring	Instrument	Depth m	<u> cm s⁻¹	<v> cm s⁻¹	Major cm s⁻¹	Minor cm s⁻¹	Angle deg
M2	ADCP	16	-2.38	0.47	13.07	9.67	344.7
M2	ADCP	24	-1.46	1.70	12.99	9.36	342.0
M2	ADCP	32	-0.88	2.45	13.01	9.24	340.3
M2	ADCP	40	-0.73	2.85	13.13	9.28	339.4
M2	ADCP	48	-0.79	3.16	13.28	9.40	339.7
M2	ADCP	56	-0.94	3.45	13.42	9.55	340.9
M2	ADCP	64	-1.08	3.59	13.65	9.73	342.1
M2	ADCP	72	-1.27	3.68	13.85	9.93	343.2
M2	ADCP	80	-1.40	3.77	14.07	10.10	344.1
M2	ADCP	88	-1.54	3.87	14.28	10.24	345.0
S2	BBADCP	210	-1.93	4.89	11.51	7.39	348.9
S2	BBADCP	218	-1.96	4.80	11.27	7.21	348.7
S2	BBADCP	226	-1.98	4.67	11.03	7.01	348.4
S2	BBADCP	234	-1.96	4.53	10.81	6.82	348.2
S2	BBADCP	242	-1.91	4.41	10.59	6.65	348.1
S2	BBADCP	250	-1.88	4.29	10.37	6.48	348.0
S2	BBADCP	258	-1.83	4.15	10.14	6.30	348.1
S2	BBADCP	266	-1.80	4.00	9.90	6.15	348.1
S2	BBADCP	274	-1.76	3.87	9.66	5.96	348.3
S2	BBADCP	282	-1.73	3.76	9.44	5.78	348.3
S2	RCM8	305	-1.7	3.5	9.40	5.80	349.0
S2	RCM8	1200	0.2	-0.8	3.40	2.00	350.0

Table III-4. Velocity statistics for M2/S2 using daily time series.

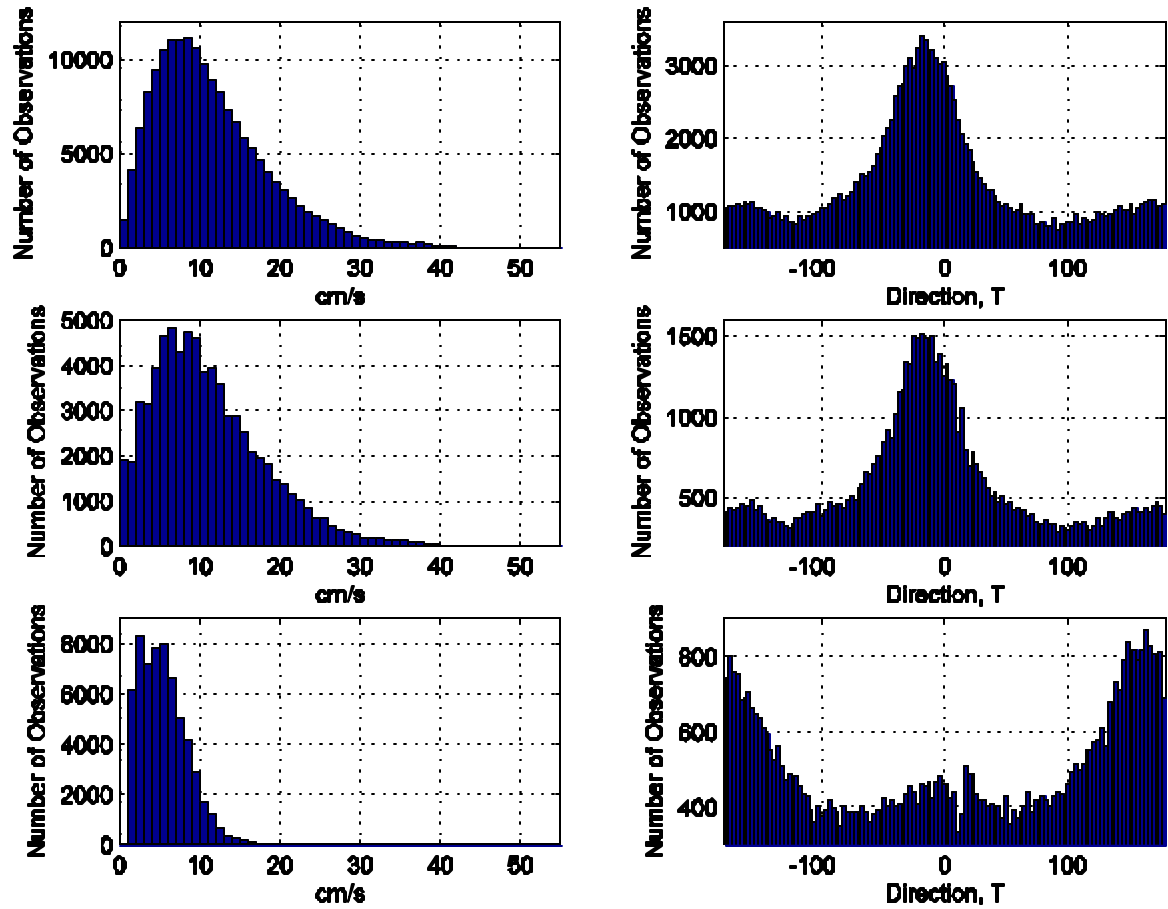


Figure III-1. Histogram of speed (left) and direction (right) for currents, at (top) 290 m, (middle) 305 m, and (bottom) 1200 m depth. The upper panel is for ADCP measurements and the middle and bottom panels are for Aanderaa RCM8 measurements.

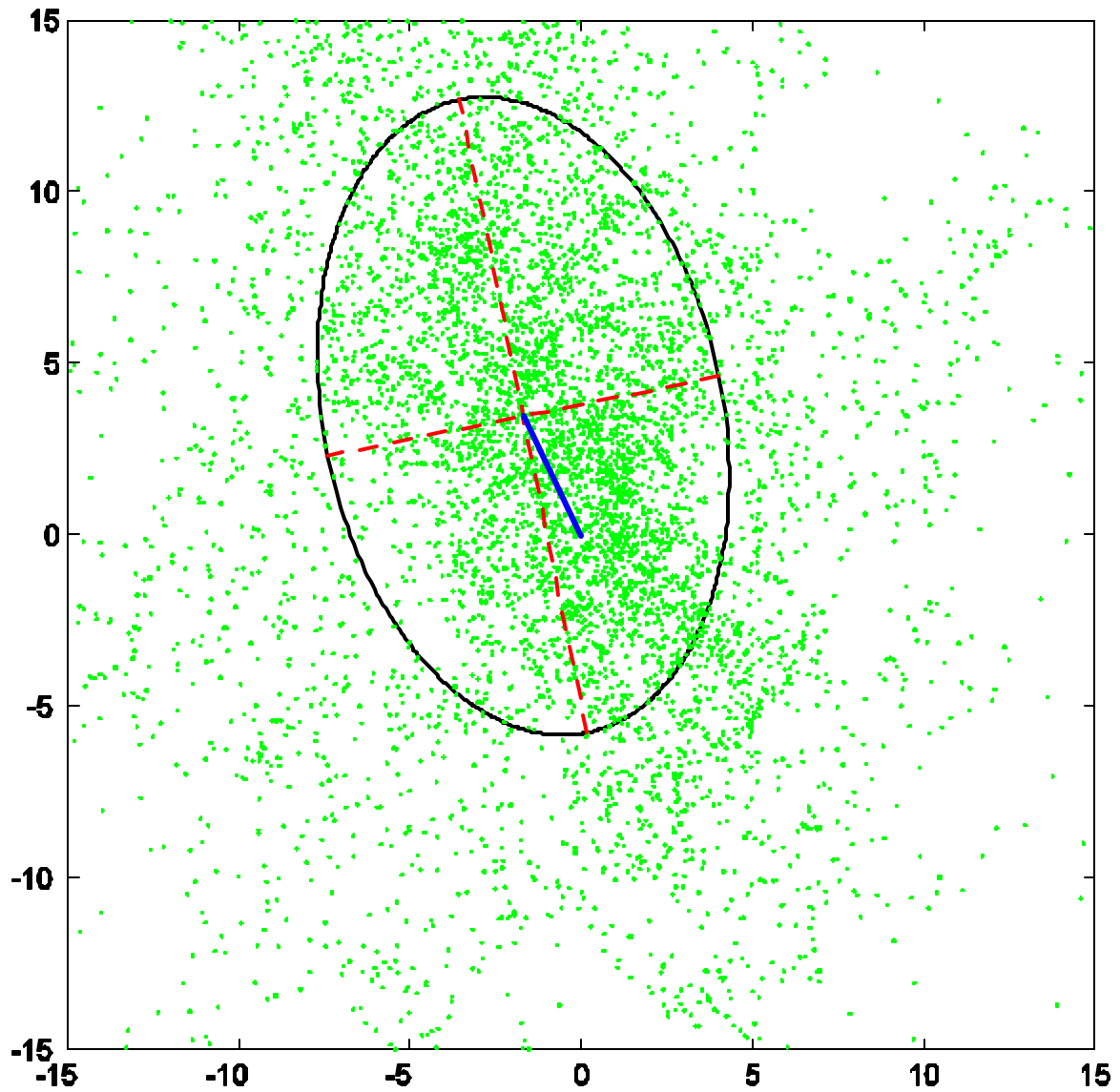


Figure III-2. Scatter plot of 6 hourly detided 305 m current observations. Note that the origin of the ellipse coincides with the mean flow.

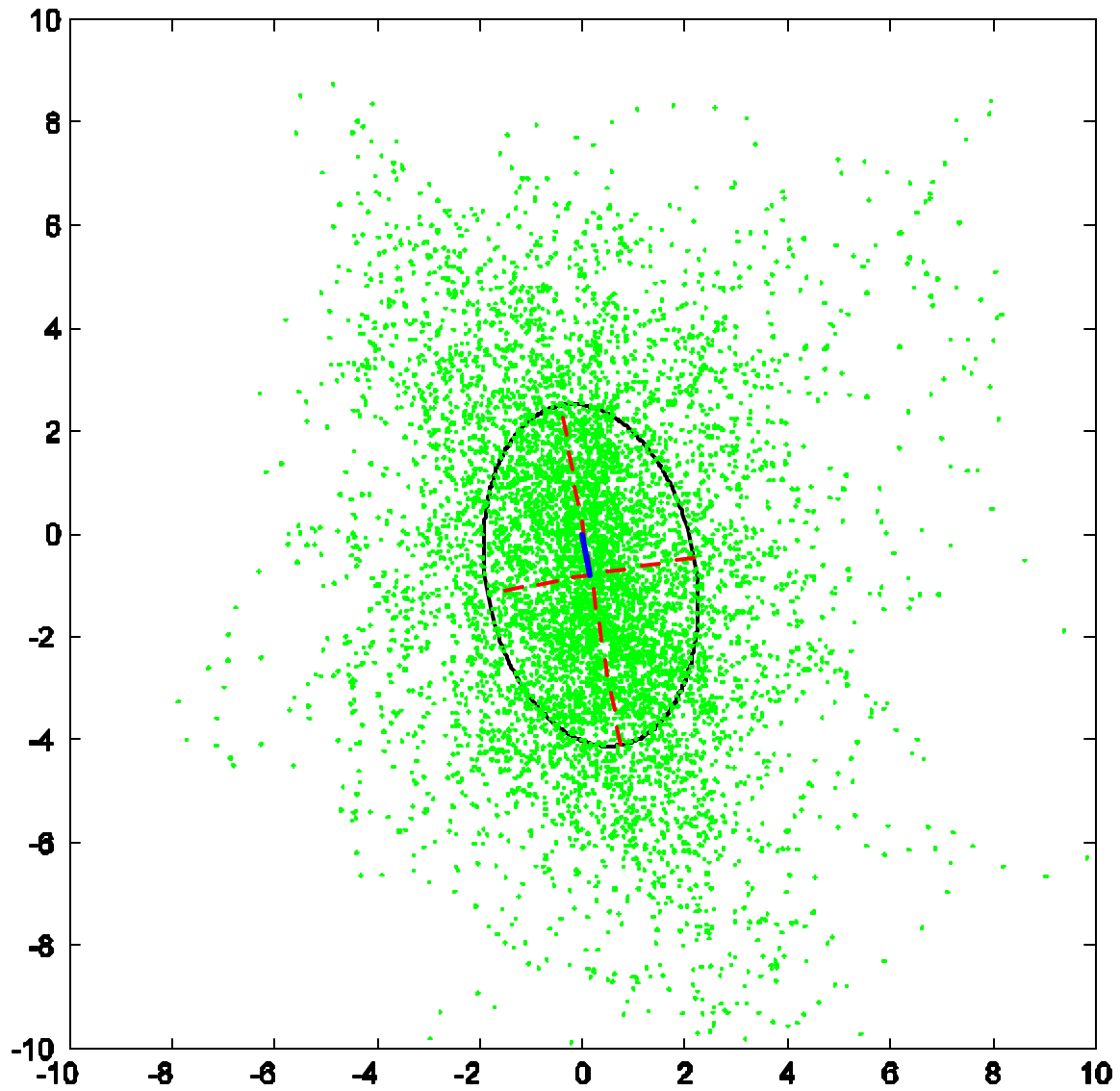


Figure III-3. Scatter plot of 6 hourly detided 1200 m current observations. Note that the origin of the ellipse coincides with the mean flow.

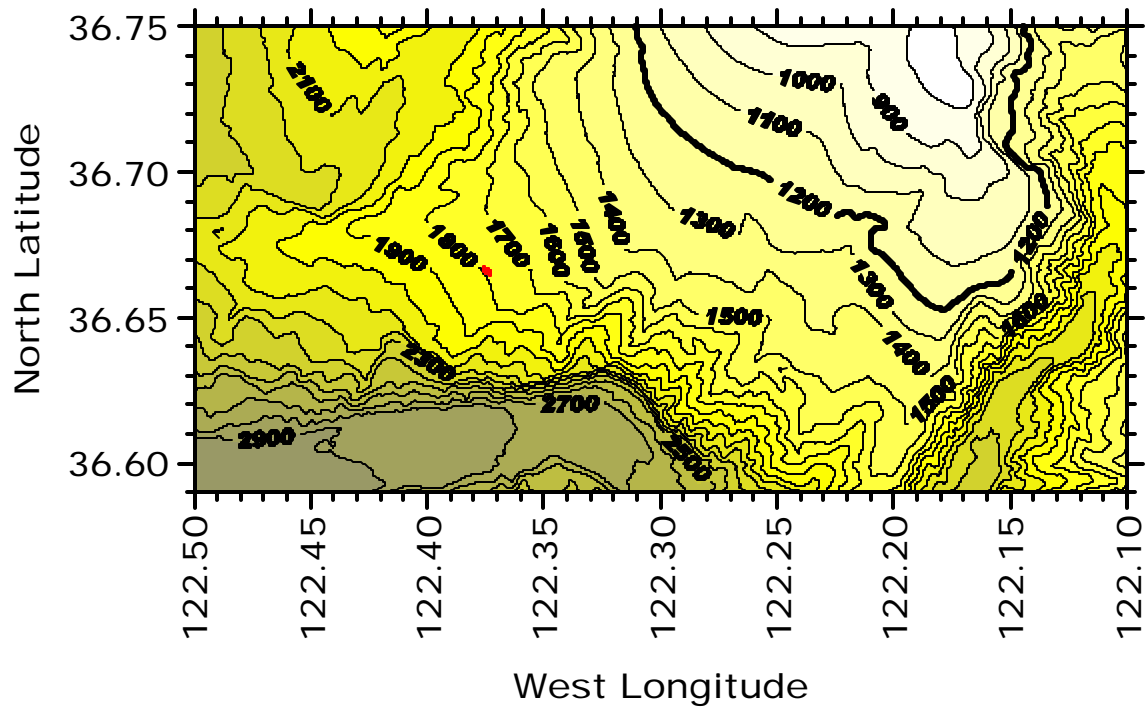


Figure III-4. Bathymetry at mooring S2. Red dots are the location of the mooring anchor for each of the 10 deployments from March 1998 to March 2003.

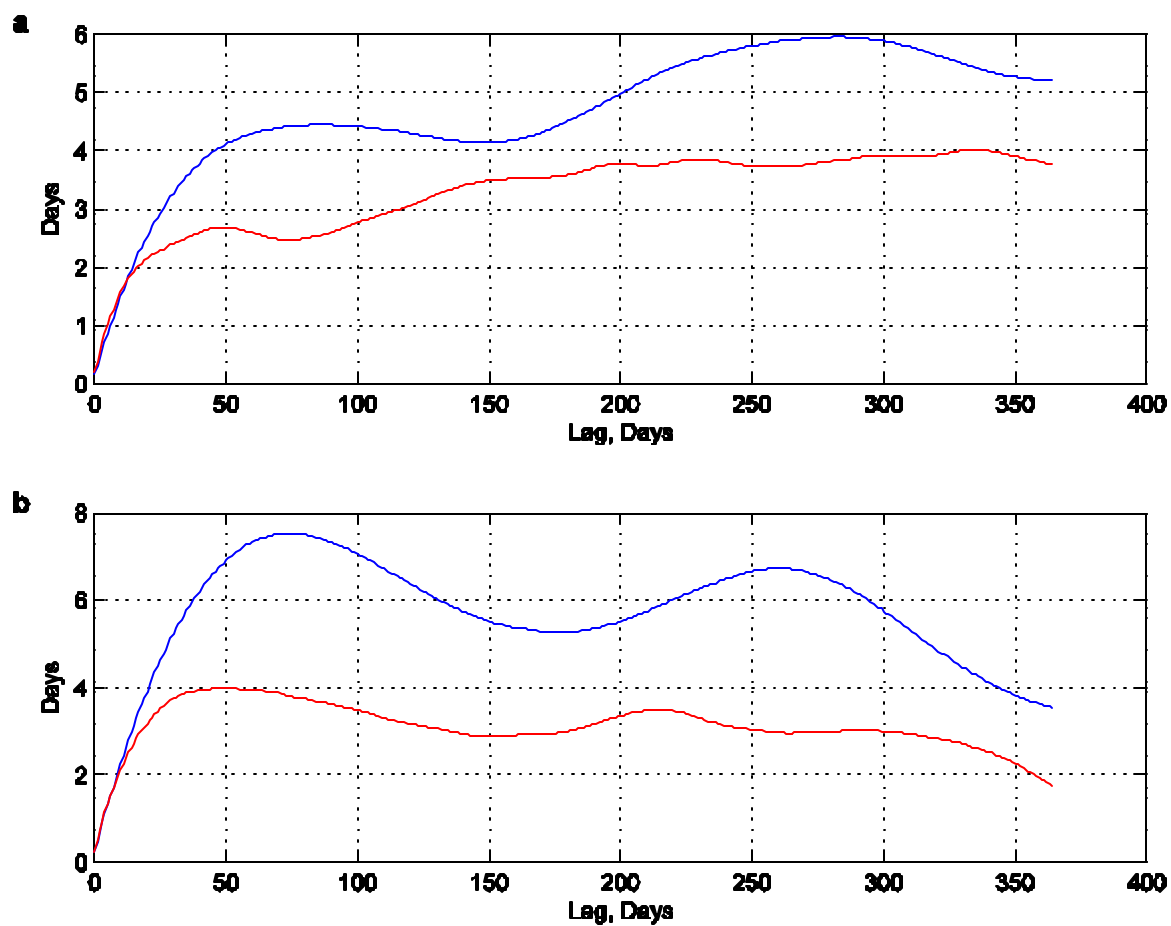


Figure III-5. Integral time scale. (a) At 305 m depth, blue (red) major (minor) axis. (b) At 1200 m depth, blue (red) major (minor) axis.

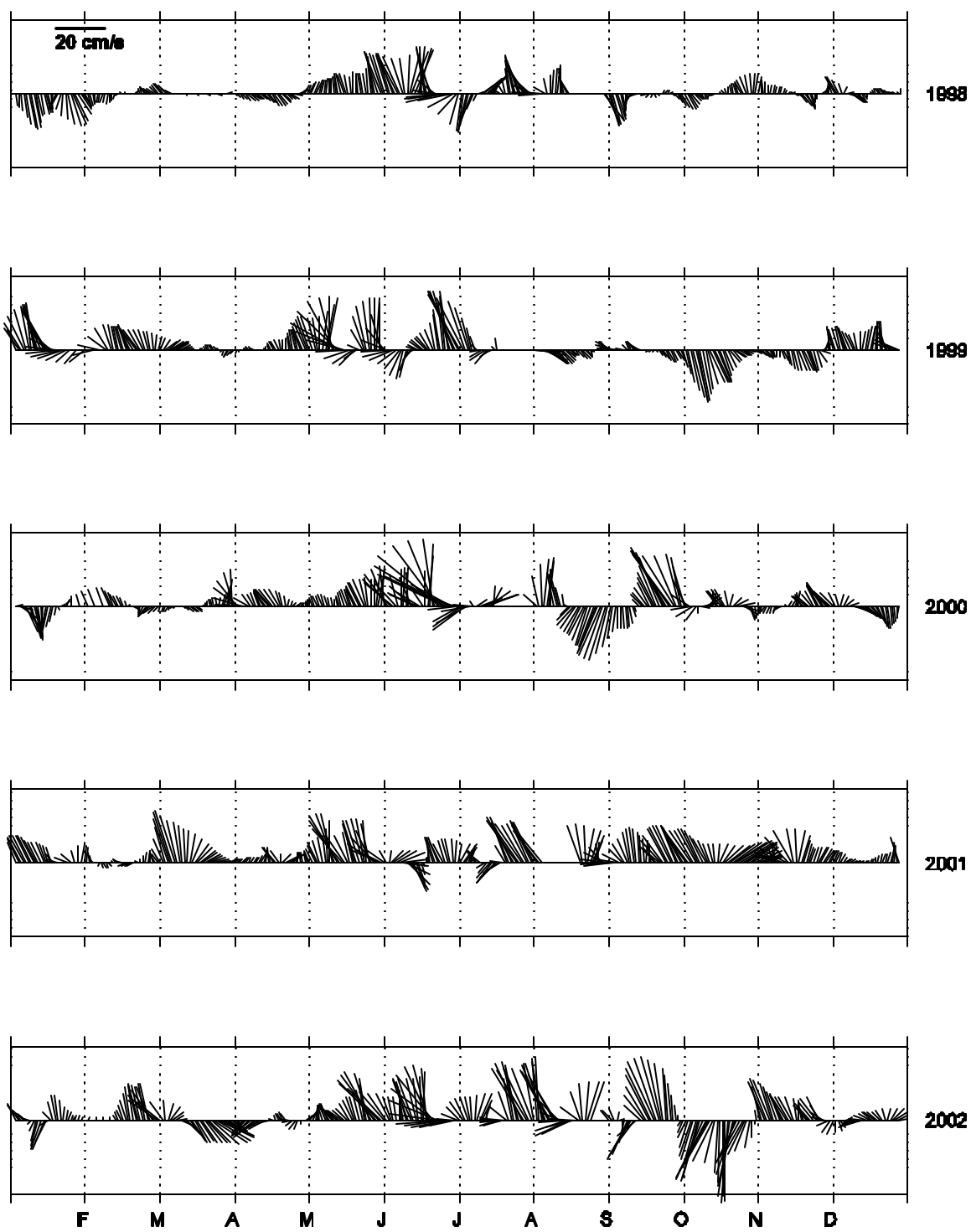


Figure III-6. Time series of daily average currents at 305 m depth.

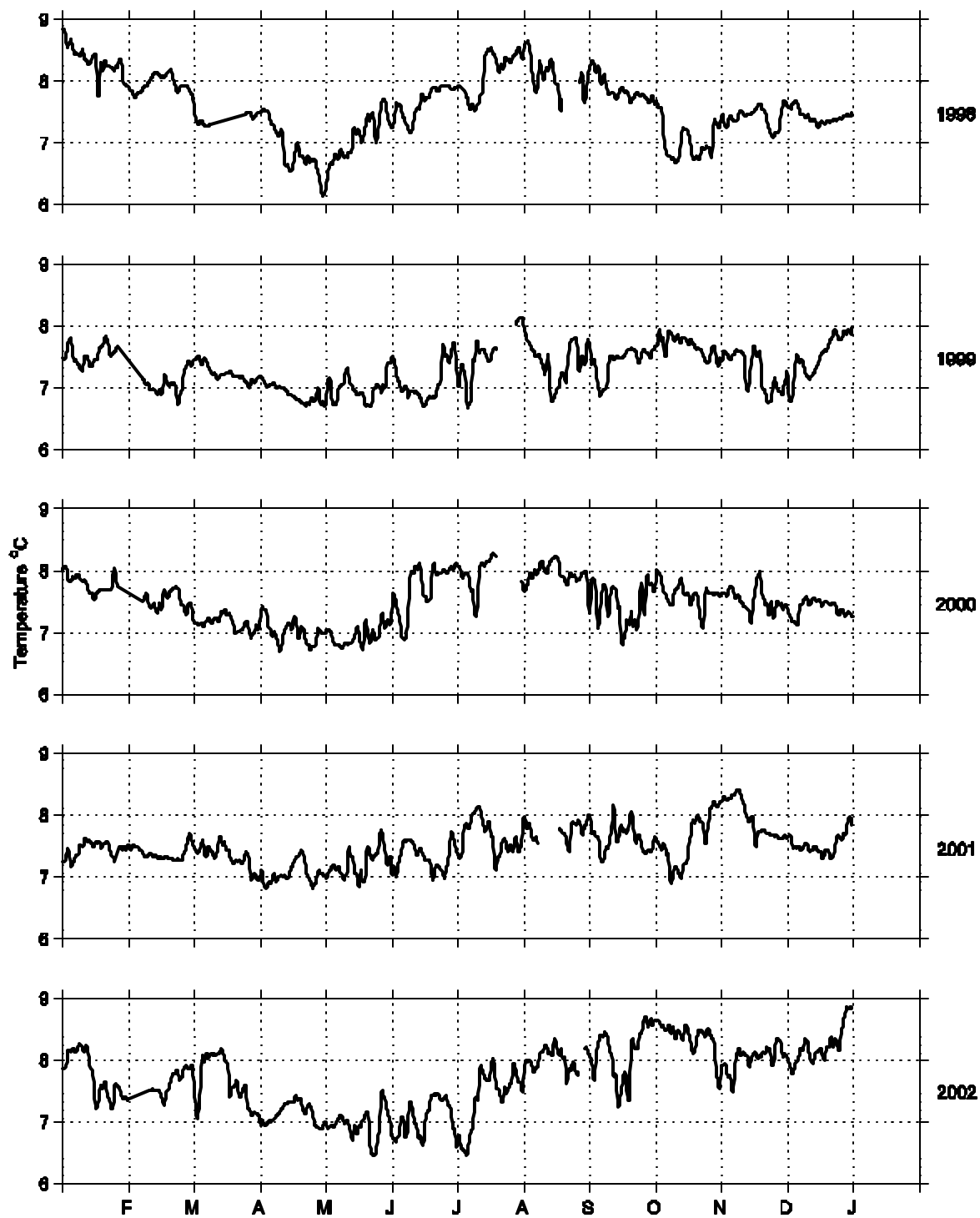


Figure III-7. Time series of daily average temperature observations at 305 m depth.

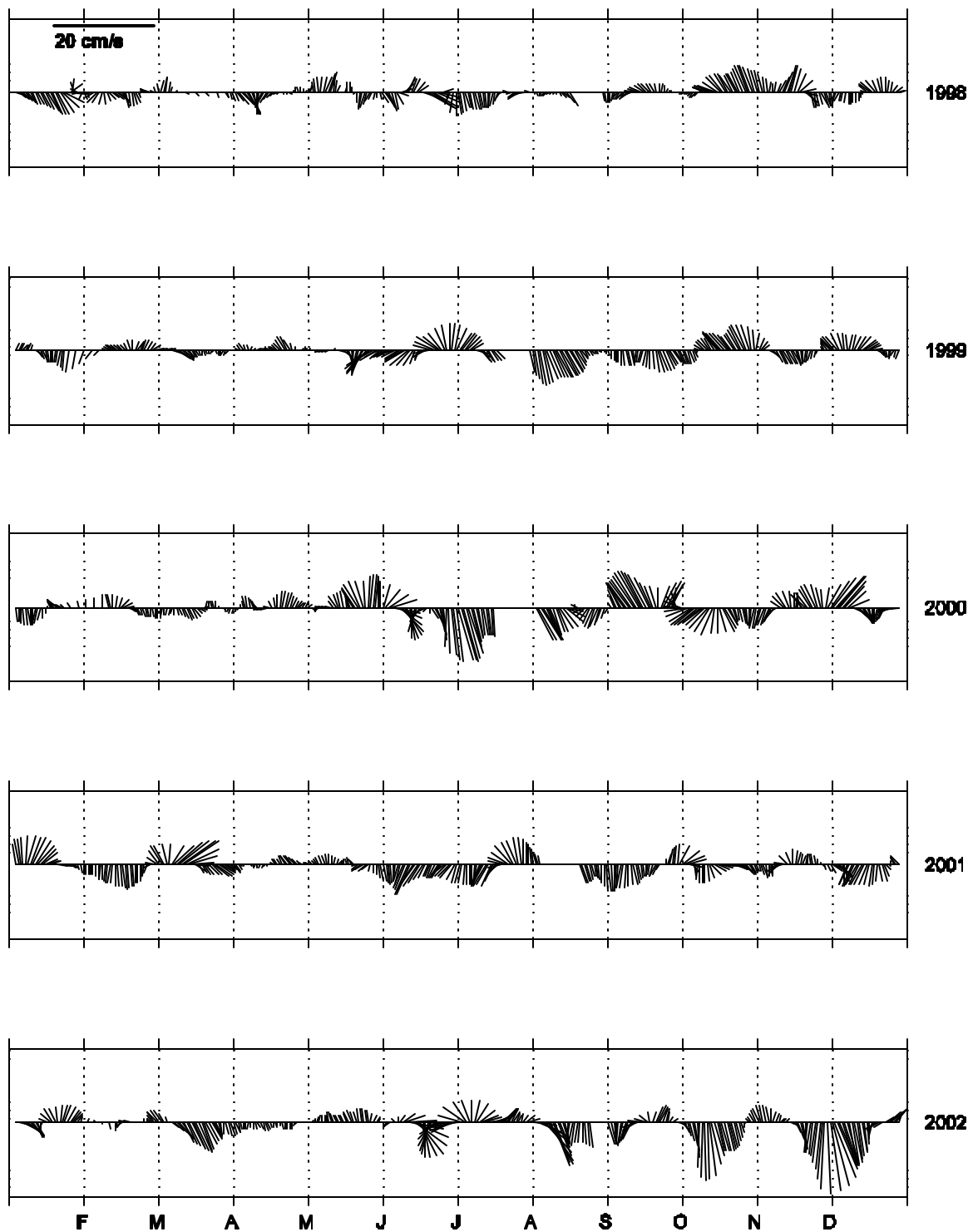


Figure III-8. Time series of daily average currents at 1200 m depth.

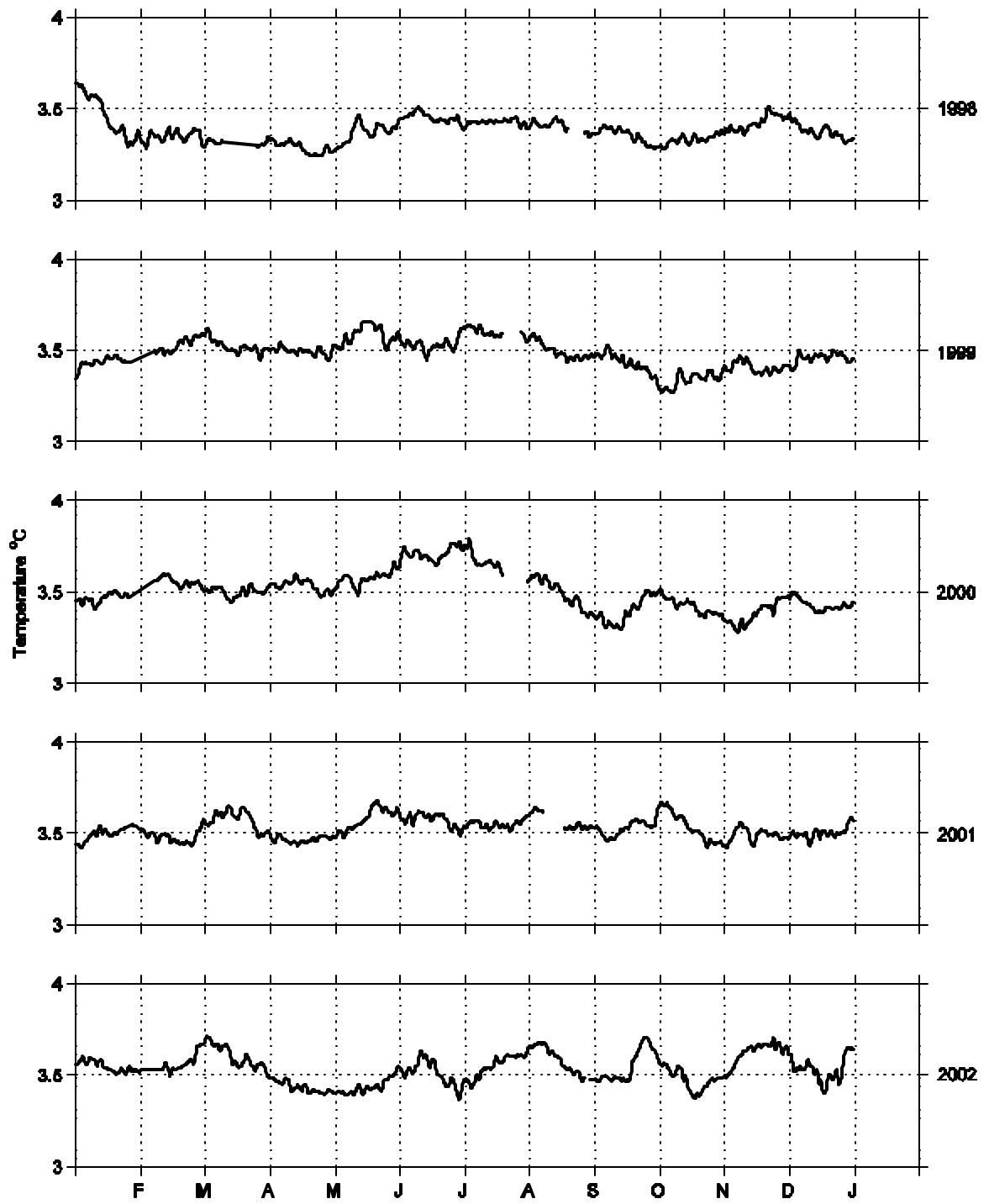


Figure III-9. Time series of daily average temperature observations at 1200 m depth.

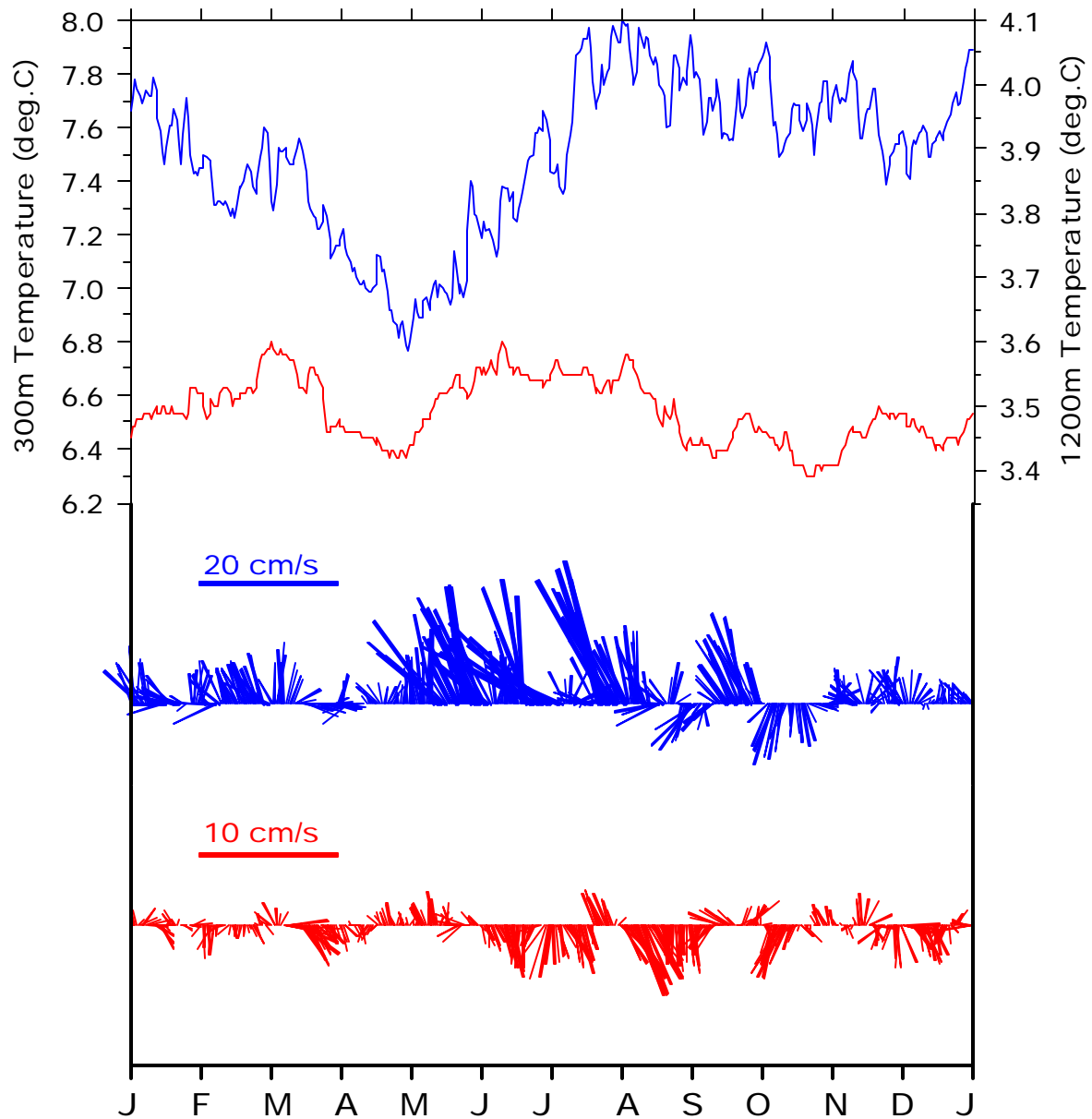


Figure III-10. Time series of daily average temperature and currents at 305 m (blue) and 1200 m (red), respectively.

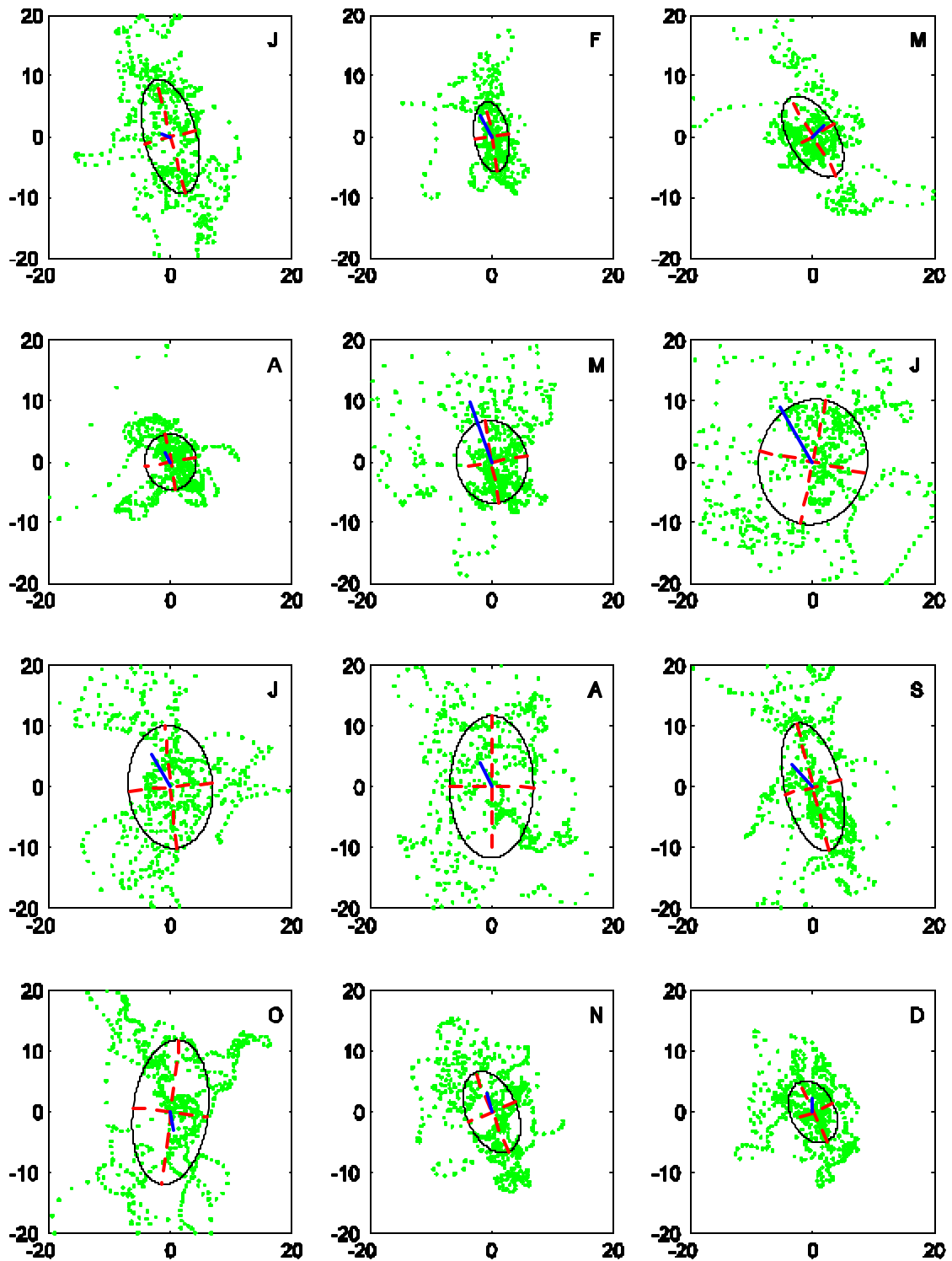


Figure III-11. Scatter plot of monthly 305 m current observations, from March 24, 1998 to March 11, 2003.

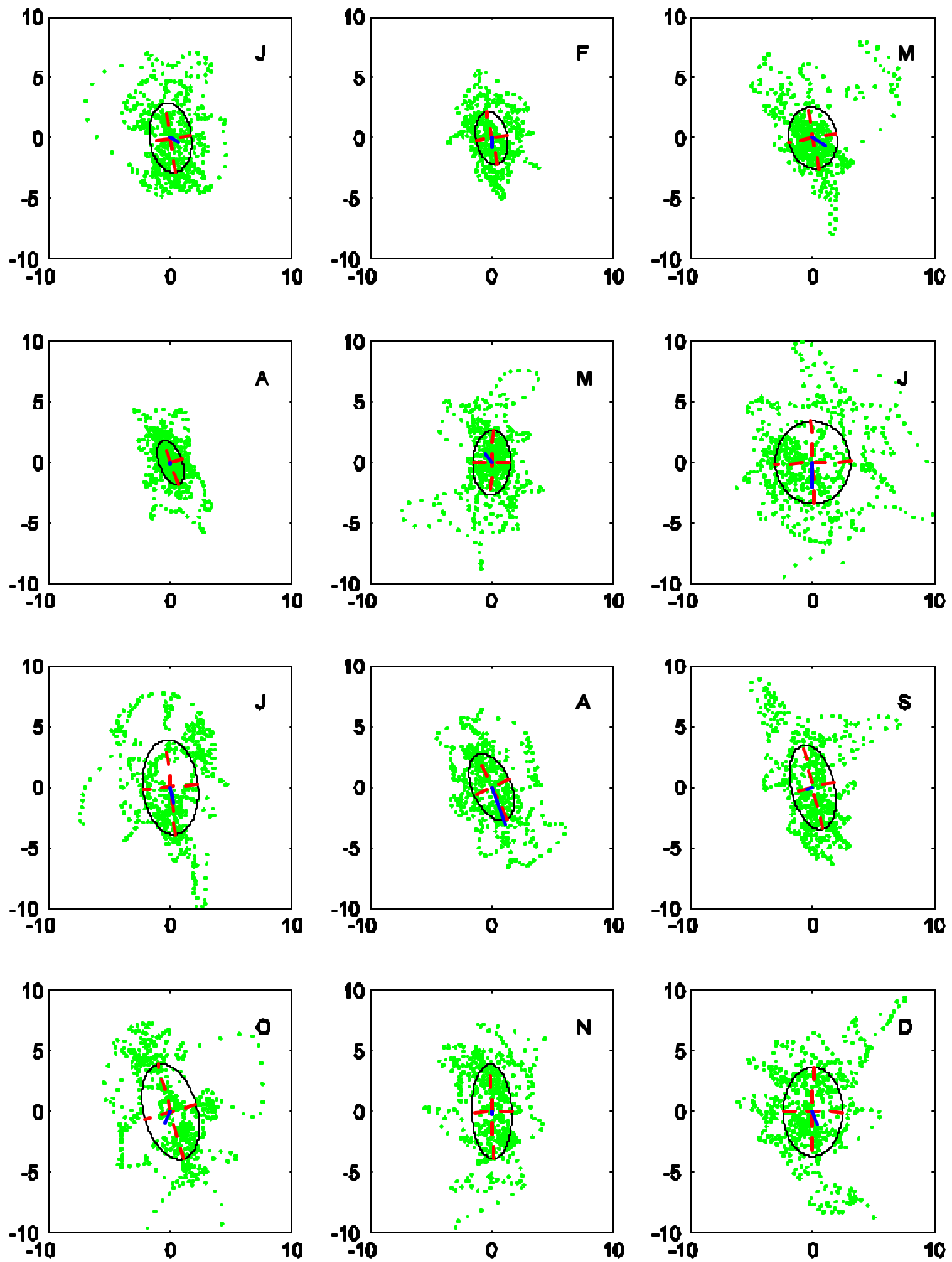


Figure III-12. Scatter plot of monthly 1200 m current observations, from March 24, 1998 to March 11, 2003.

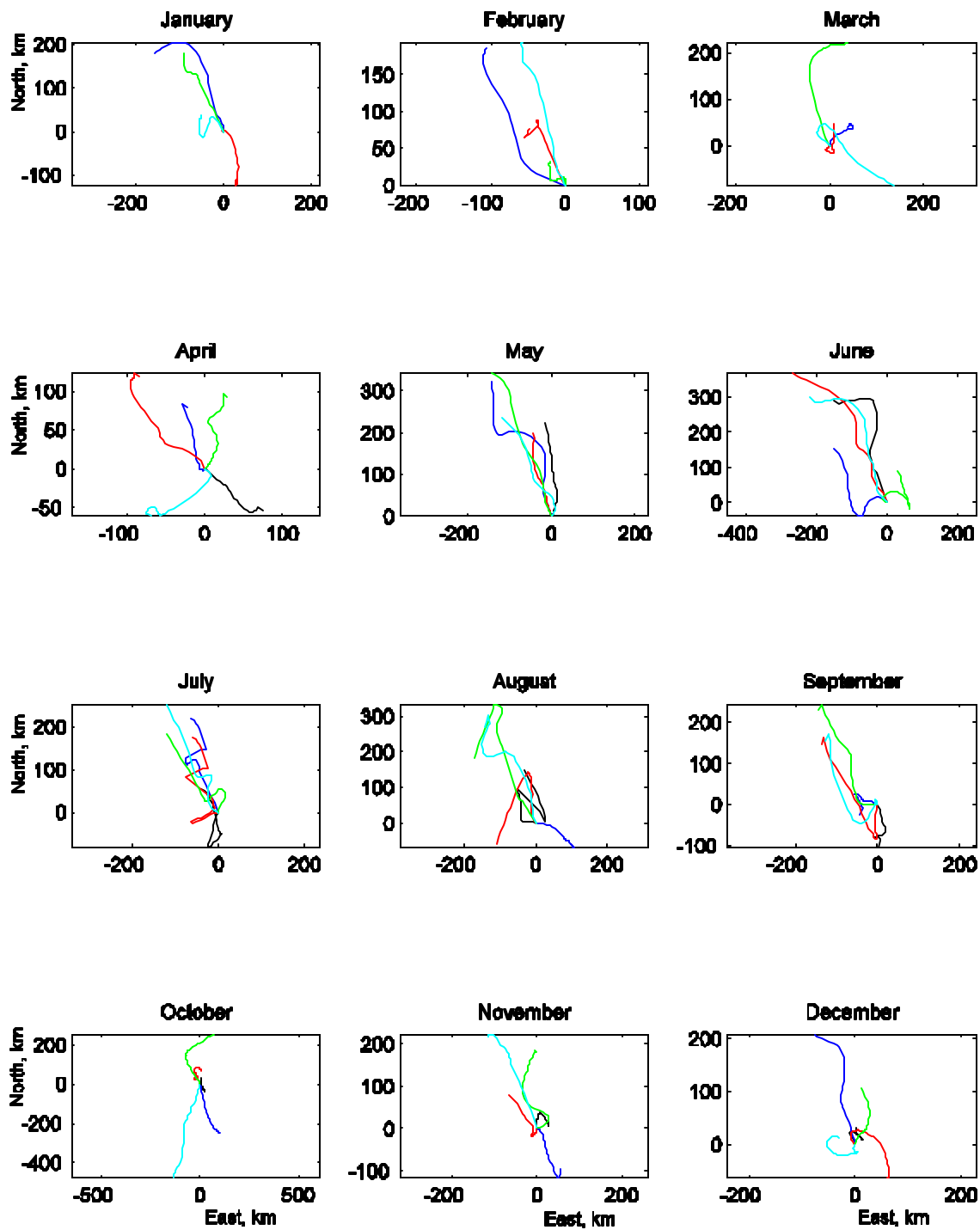


Figure III-13. Progressive Vector Diagram for current meter at 305 m depth. Solid black line (blue, red, green, cyan) corresponds to 1998 (1999, 2000, 2001, and 2002).

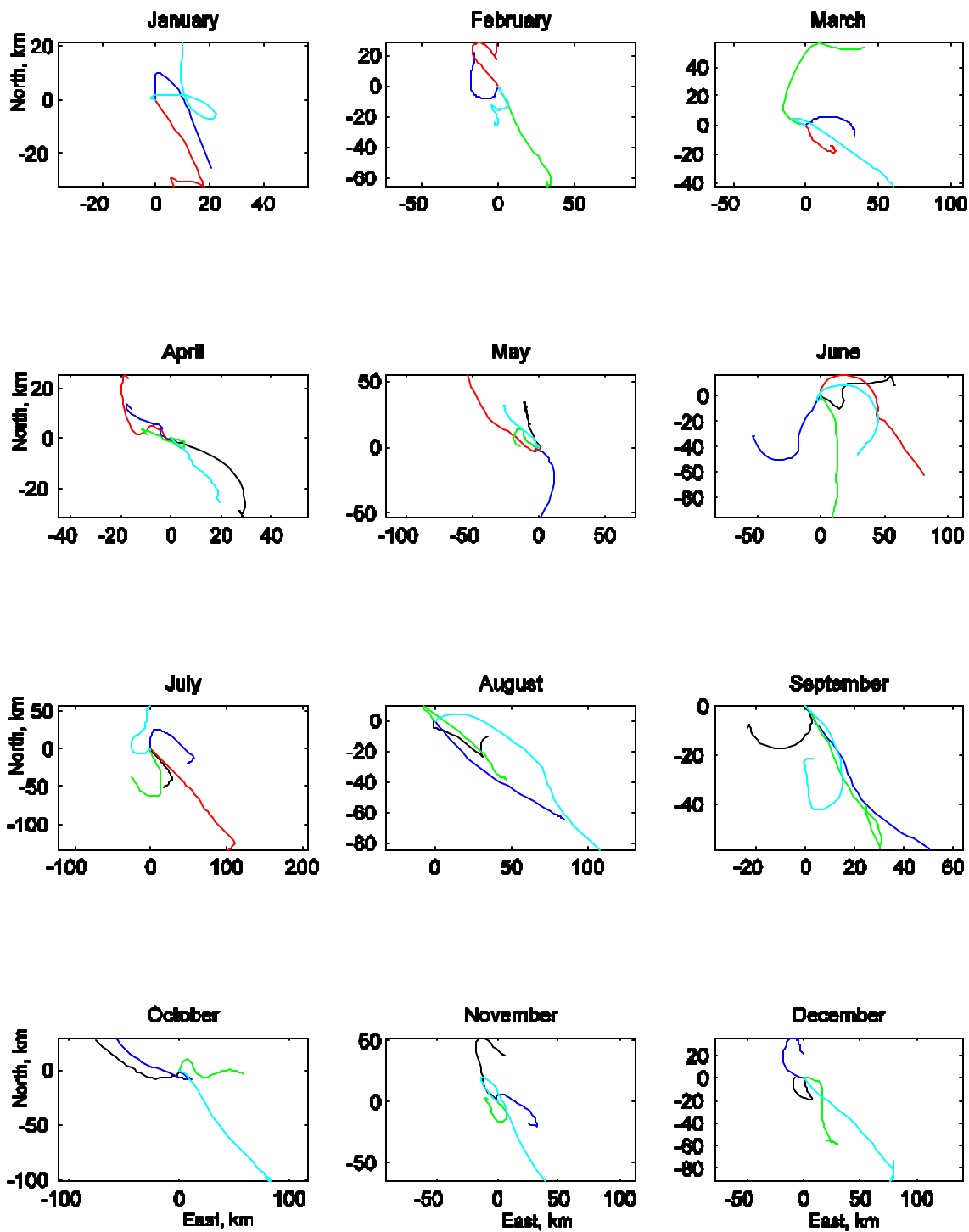


Figure III-14. Progressive Vector Diagram for current meter at 1200 m depth. Solid black line (blue, red, green, cyan) corresponds to 1998 (1999, 2000, 2001, and 2002).

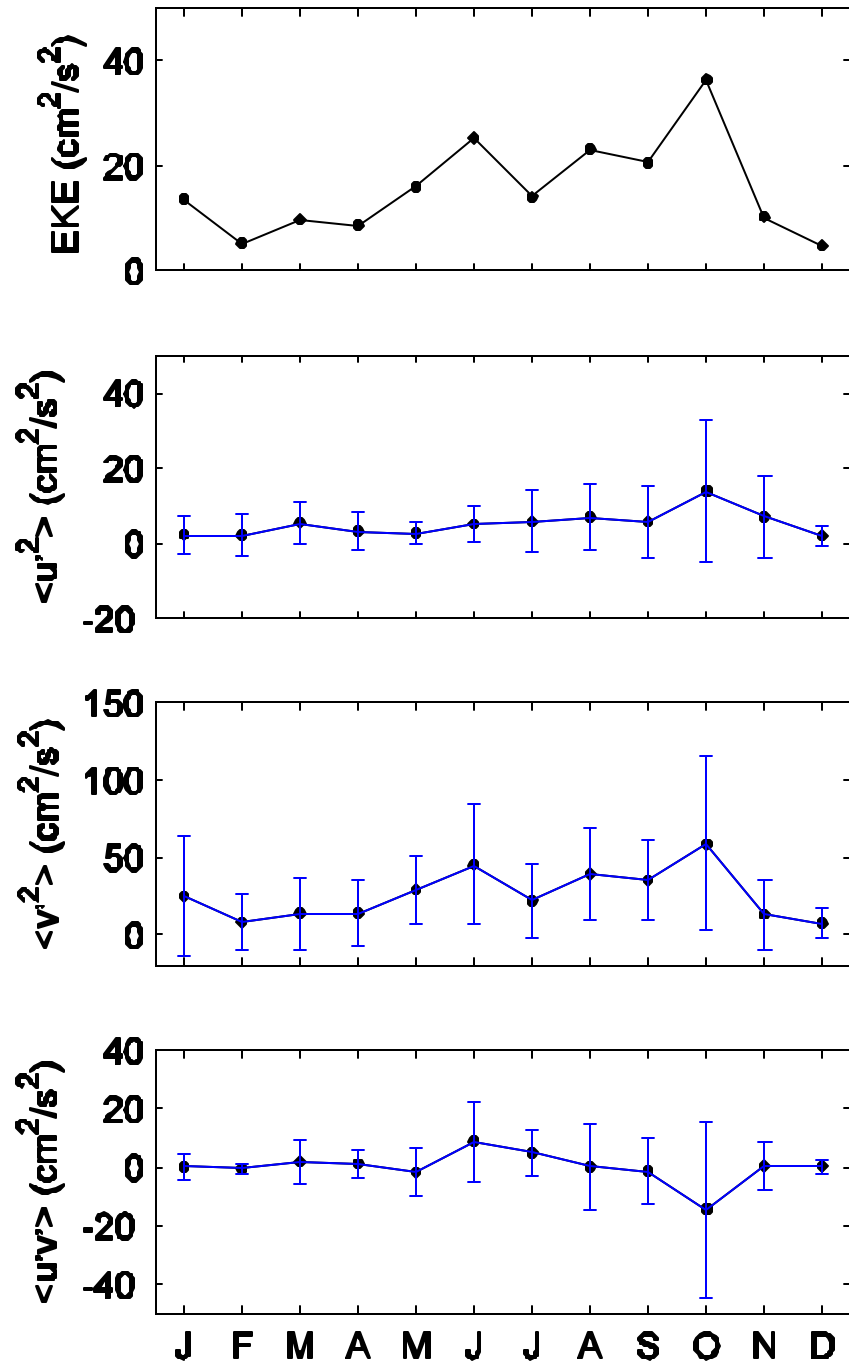


Figure III-15. Eddy field of daily averaged currents at 305 m. A 7-day running mean was used to remove high frequency variability.

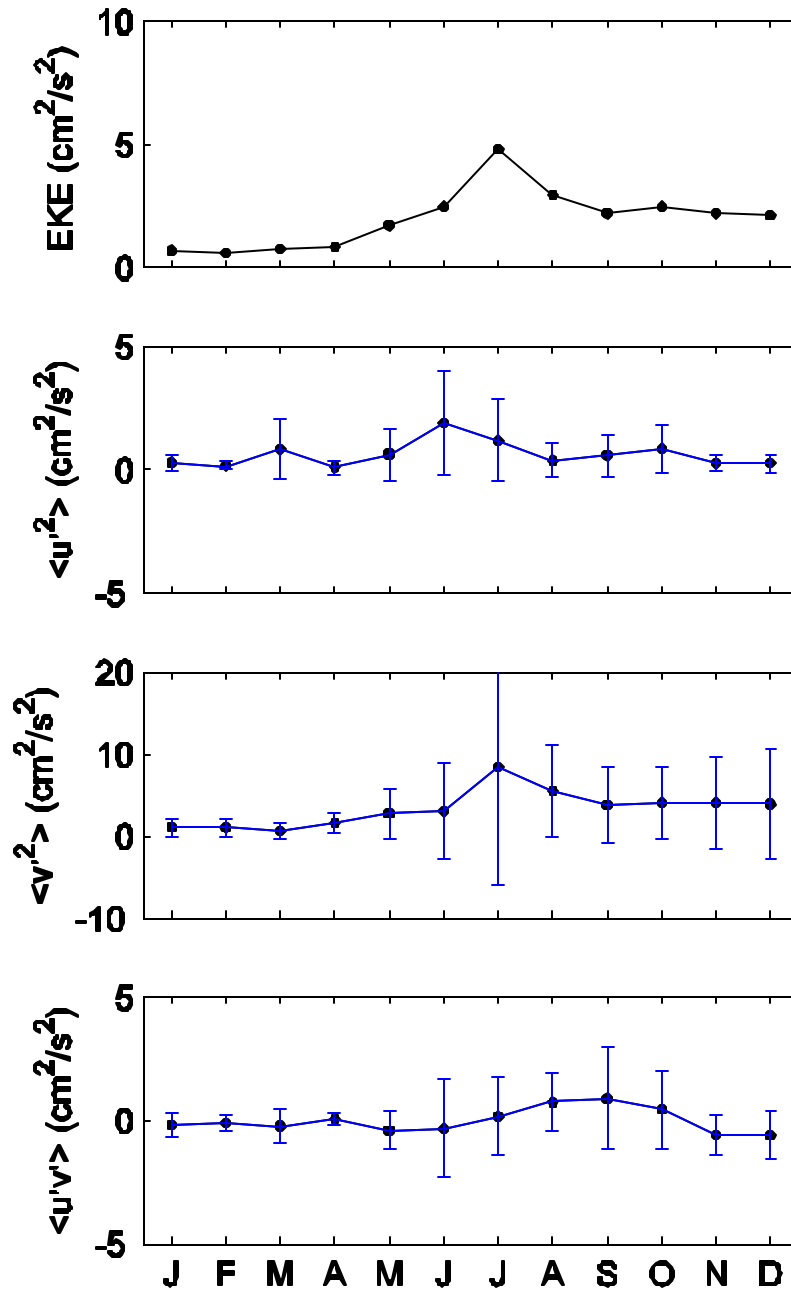


Figure III-16. Eddy field of daily averaged currents at 1200 m. A 7-day running mean was used to remove high frequency variability.

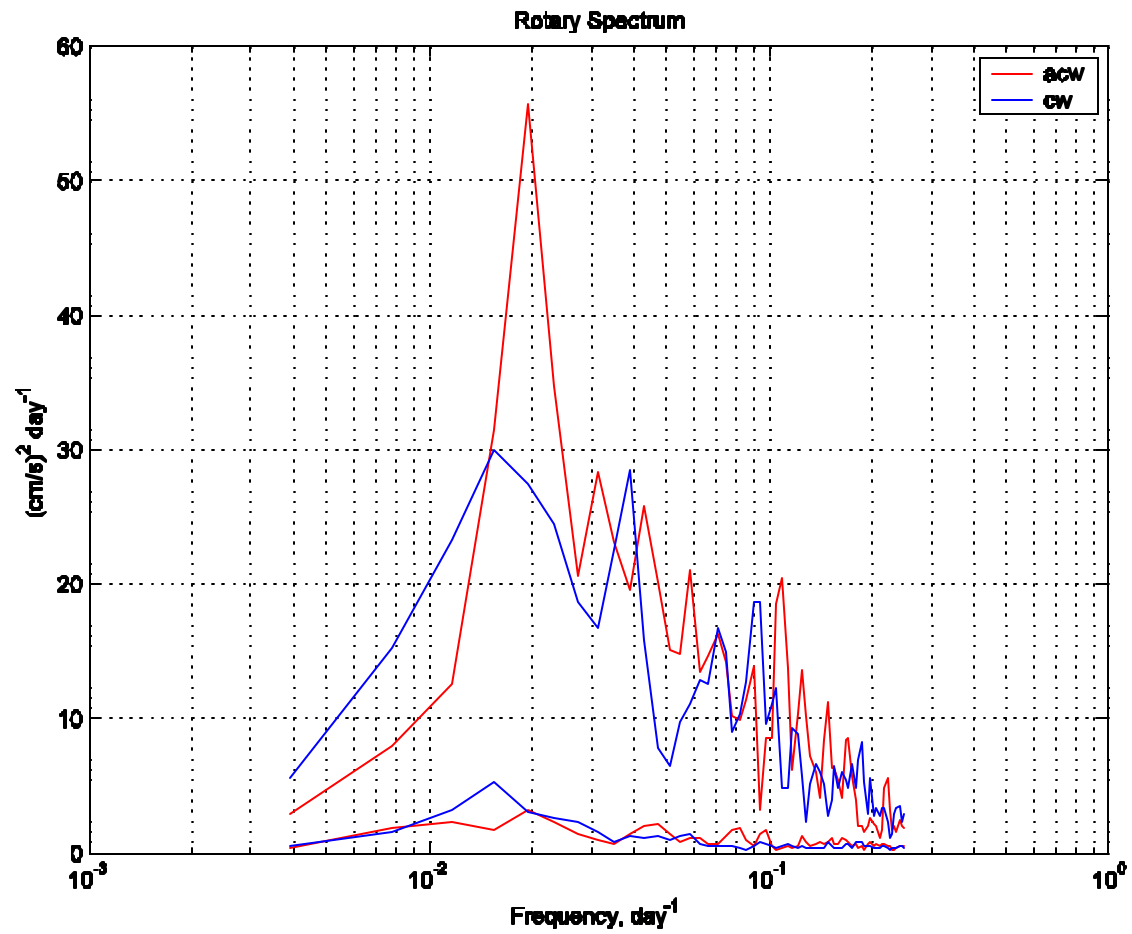


Figure III-17. Rotary spectra of the currents at 305 m (upper spectra) and 1200 m (lower spectra). The red (blue) line is the anticlockwise (clockwise) rotation.

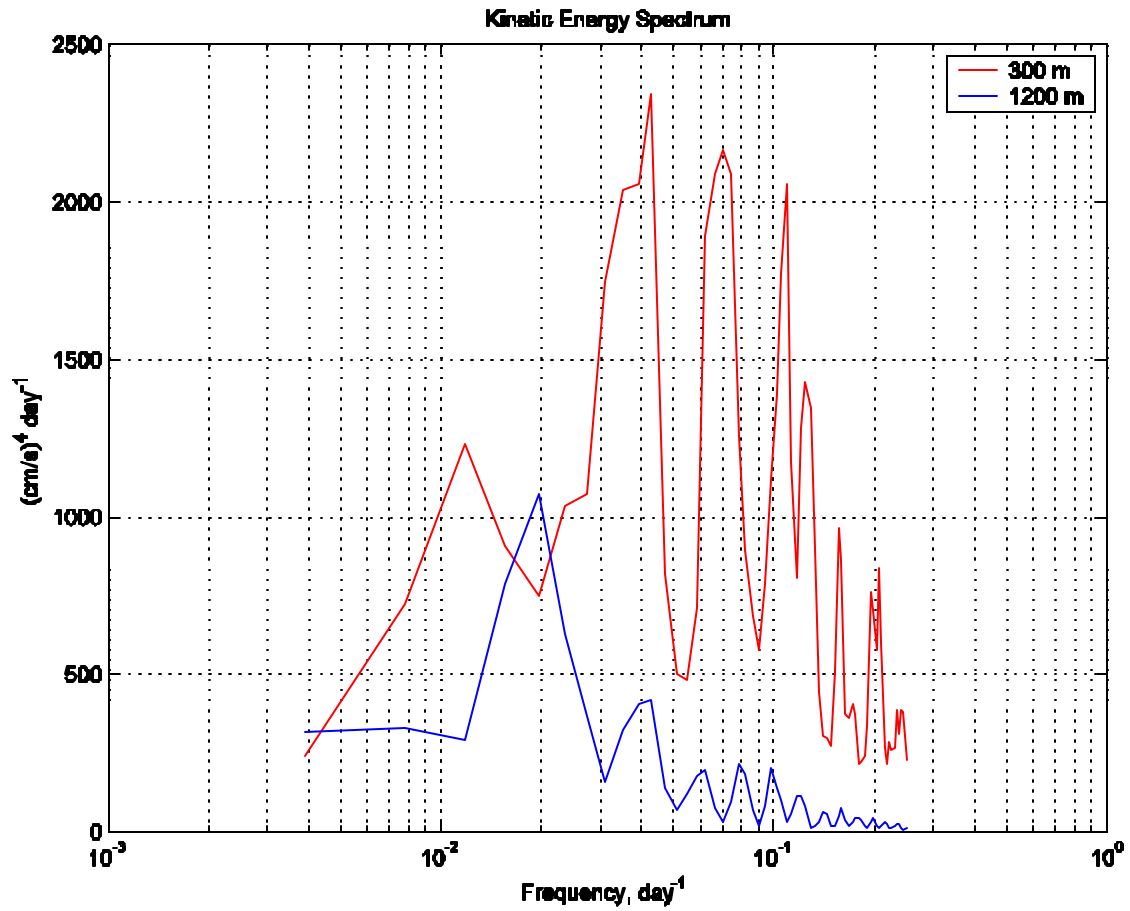


Figure III-18. Eddy kinetic energy variance preserving spectra at 305 (red line) and 1200 m (blue line).

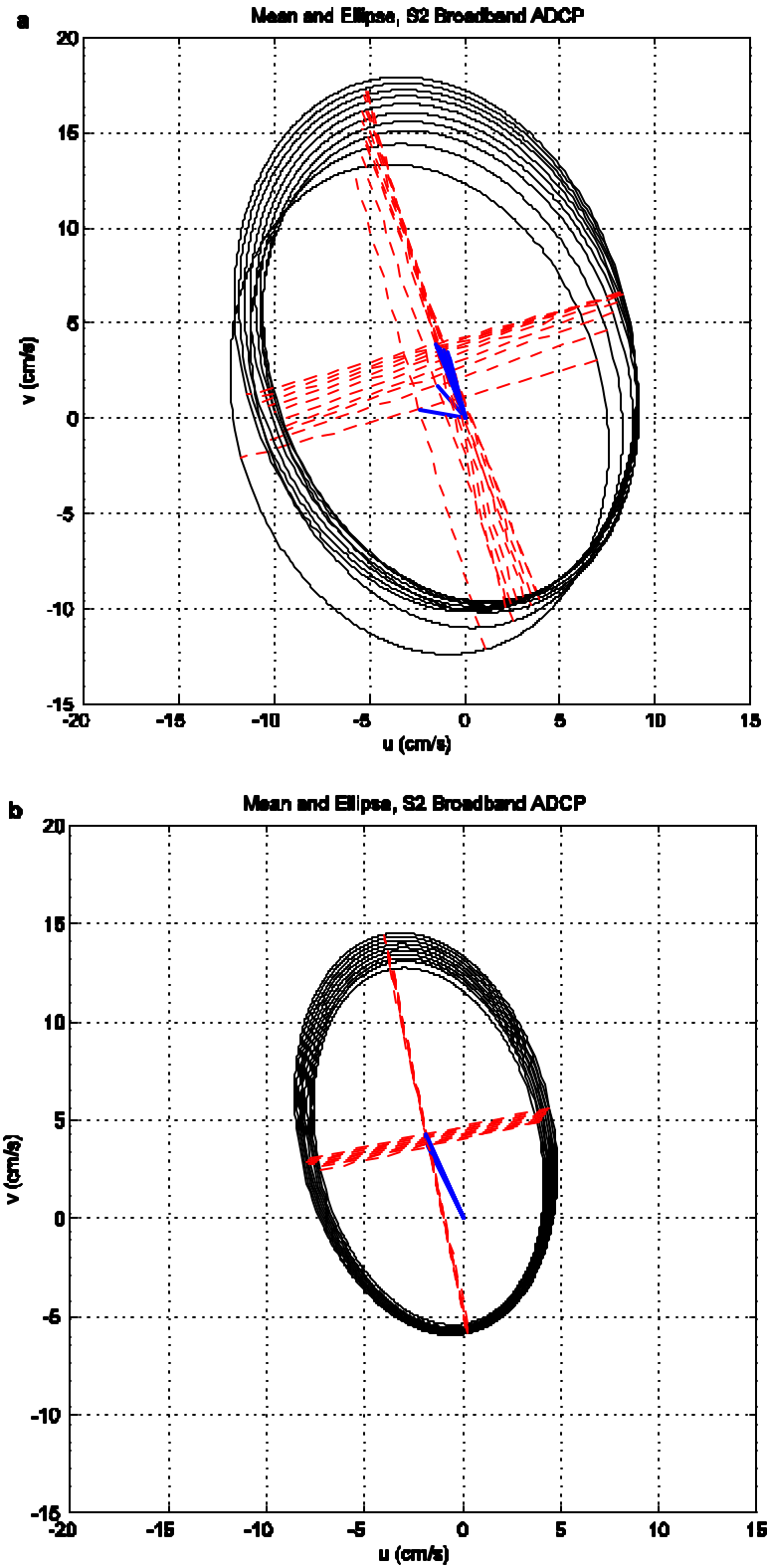


Figure III-19. Mean (blue), principal axes (red), and standard deviation ellipses at (upper) M2, 16-88 m, and (lower) S2, 210-290 m.

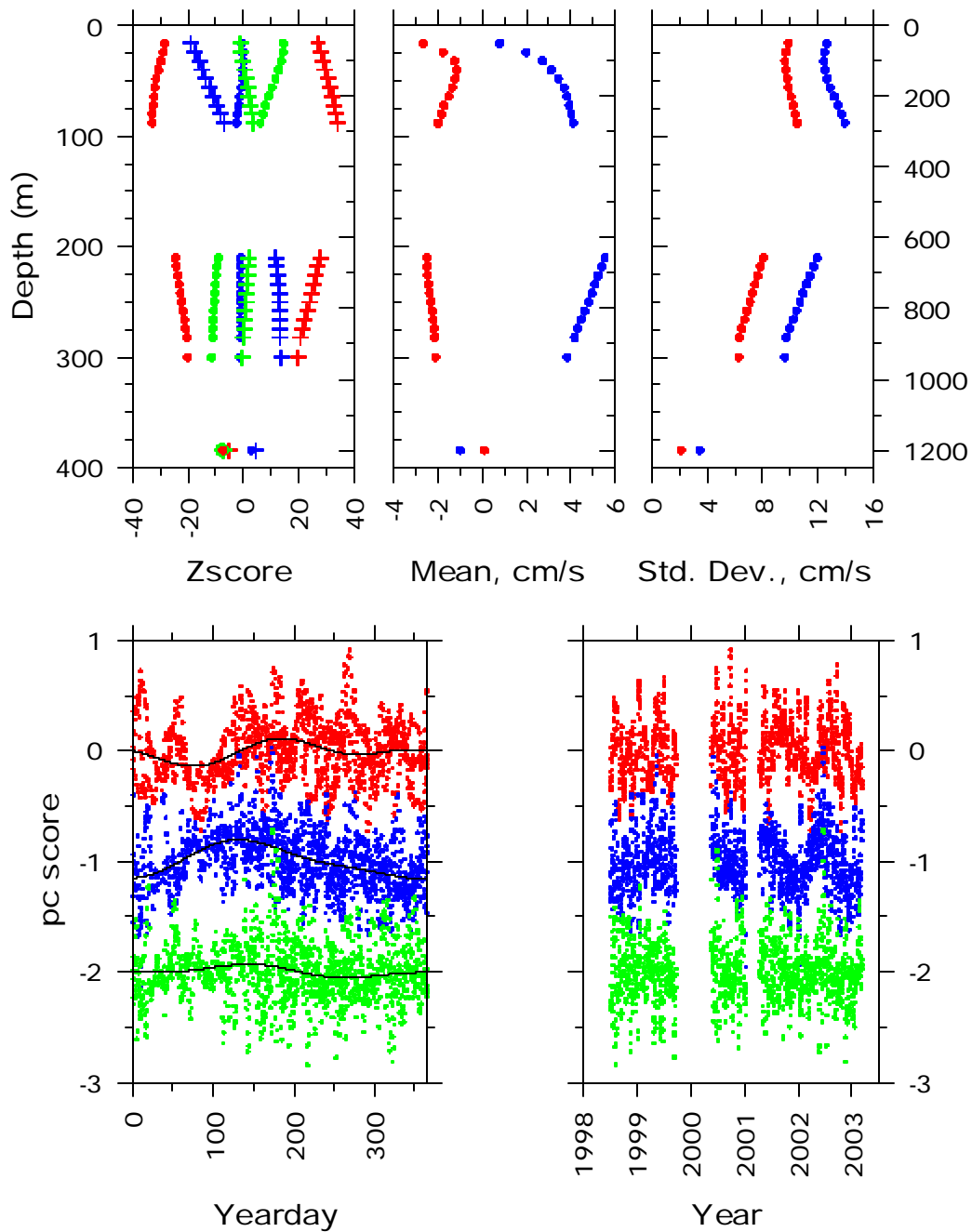


Figure III-20. Vertical structure of horizontal velocity at M2/S2. (upper) Zscore, mean and standard deviation of east-west (u) and north-south (v) components of velocity. (lower) Temporal variability of first three principal components as a function of yearday (left) and year (right). The first principal component is red, the second is blue and is displaced -1, and the third is green and displaced -2. Black solid lines in the lower right represent a biharmonic fit to the temporal variability of the corresponding principal component.

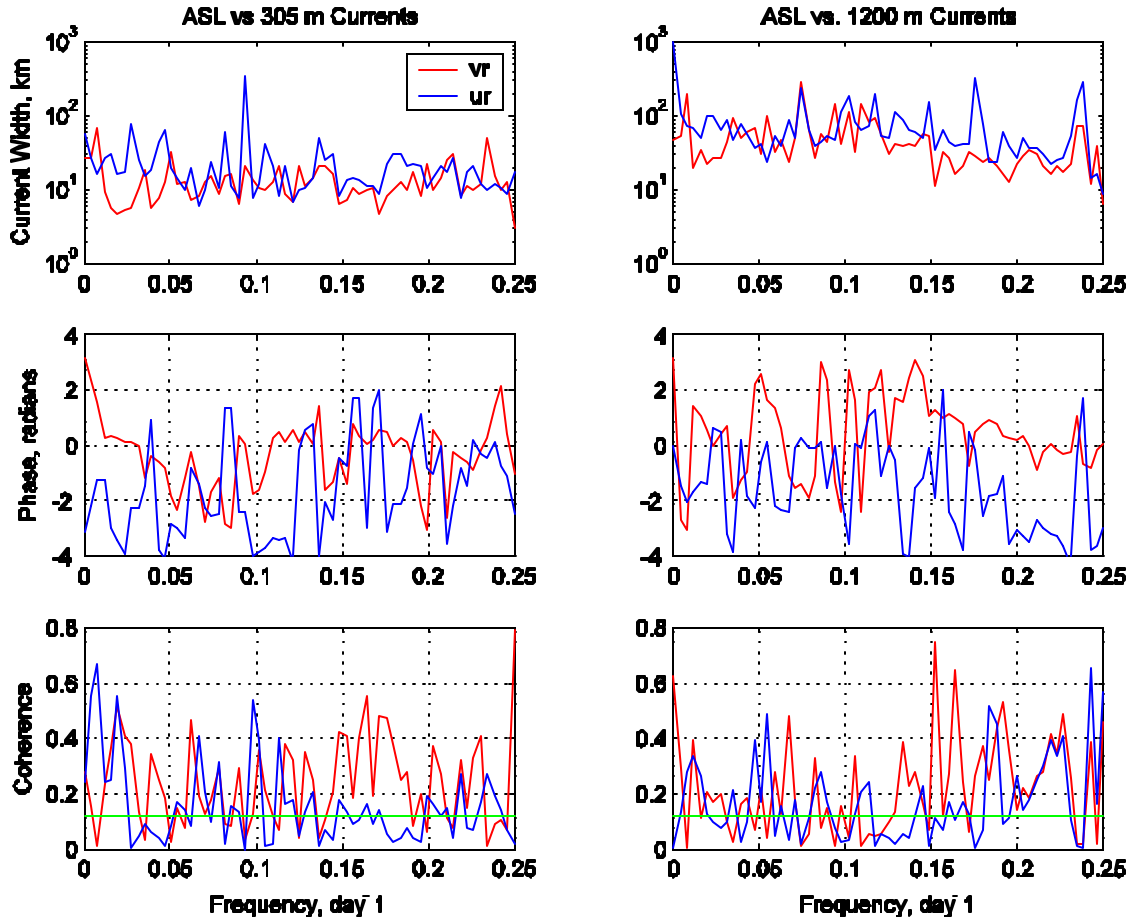


Figure III-21. Frequency dependent transfer functions between adjusted sea level (ASL) for Monterey and S2 currents. From left to right, the panels are current width (upper left), phase (mid left), and coherence (bottom left) of ASL vs. 305 m currents. Current width (upper right), phase (mid right), and coherence (bottom right) of ASL vs. 1200 m currents. Red (blue) line is ASL vs. along shore currents (ASL vs. across shore currents), and the green line on coherence panels represents the 99% confidence interval.

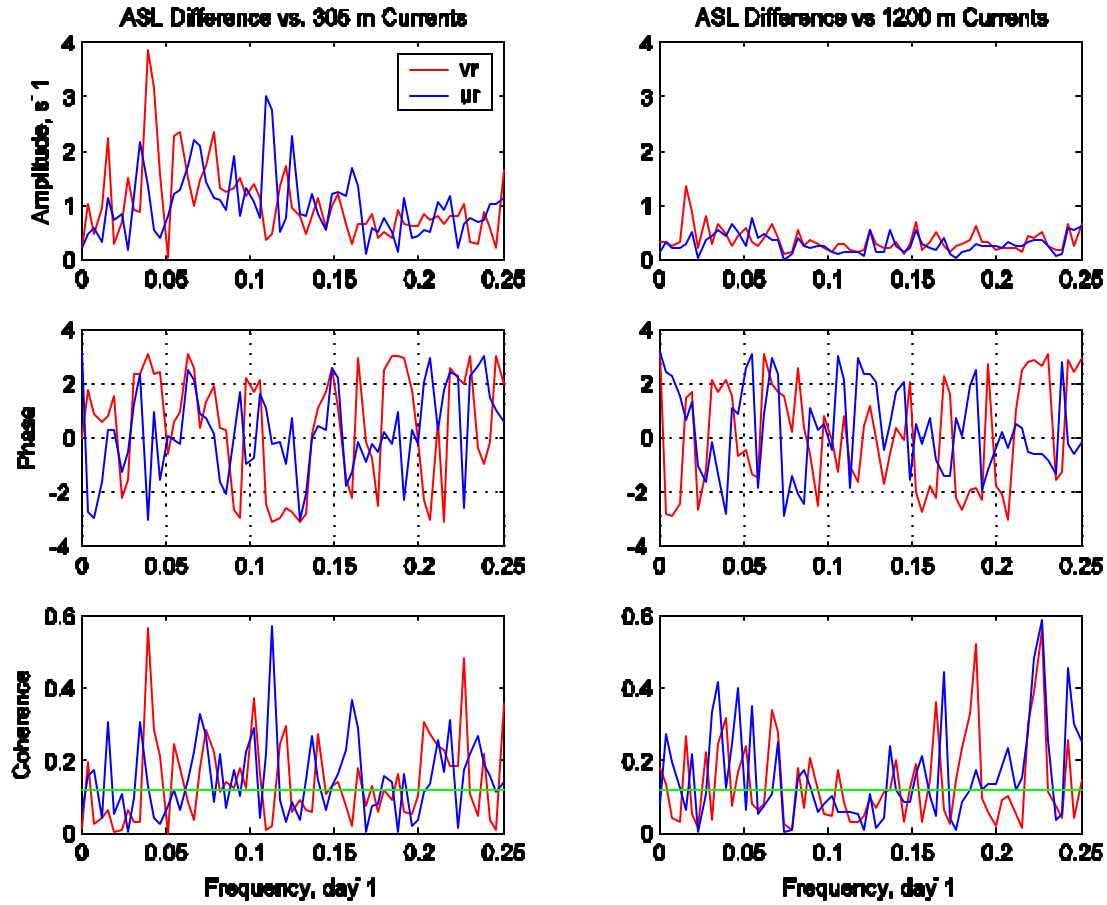


Figure III-22. Frequency dependent transfer functions for the change in horizontal pressure gradient versus S2 currents. The change in horizontal pressure gradient was approximated by subtracting ASL for Monterey from ASL at Port San Luis. From left to right, the panels are amplitude (upper left), phase (mid left), and coherence (bottom left) of ASL difference between Port San Luis and Monterey vs. 305 m currents. Amplitude (upper right), phase (mid right), and coherence (bottom right) of ASL difference between Port San Luis and Monterey vs. 1200 m currents. Red (blue) line is ASL difference between Port San Luis and Monterey vs. along shore currents (ASL difference between Port San Luis and Monterey vs. across shore currents), and the green line on the coherence panels represents the 99% confidence interval.

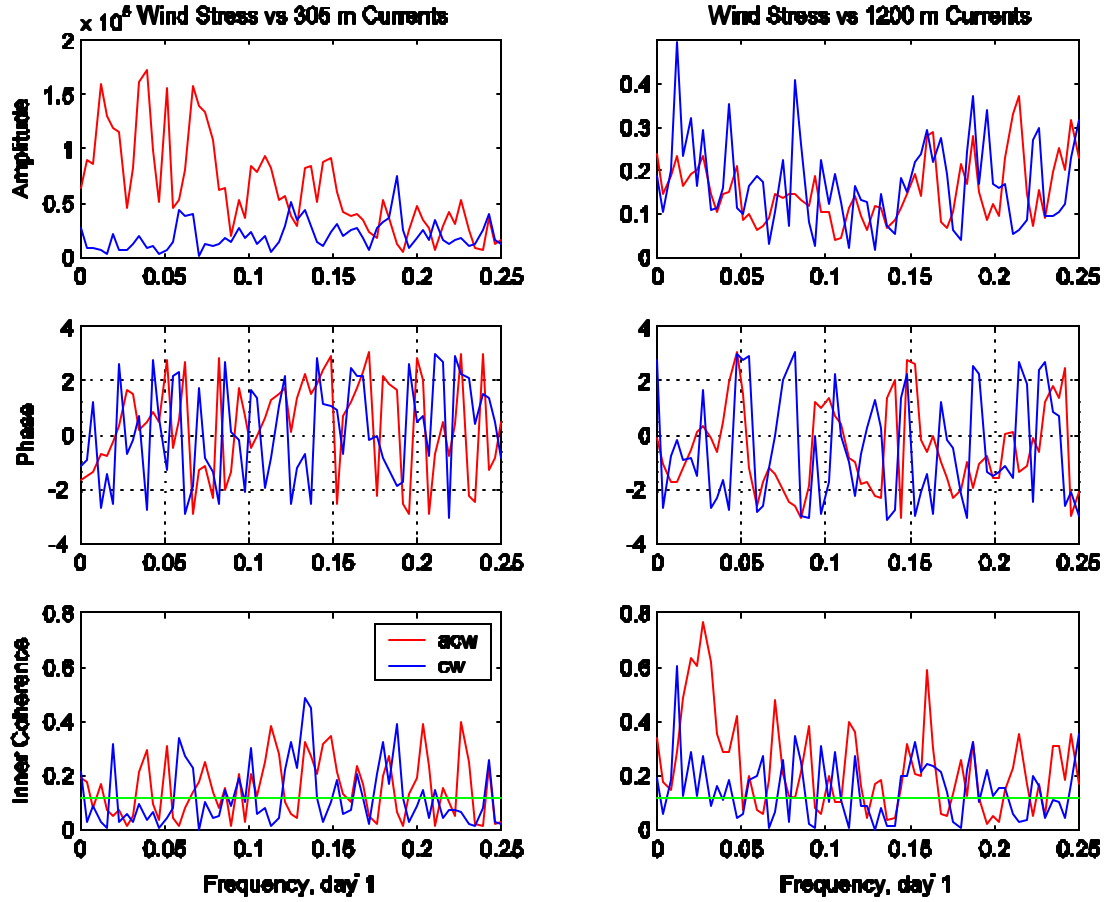


Figure III-23. Frequency dependent transfer functions for rotary cross spectra. From left to right, the panels are amplitude (upper left), phase (mid left), and coherence (bottom left) of wind stress vs. 305 m currents. Amplitude (upper right), phase (mid right), and coherence (bottom right) of wind stress vs. 1200 m currents. The red (blue) line is the alongshore wind stress vs. alongshore currents (across shore wind stress vs. across shore currents) and the green line on coherence panels represents the 99% confidence interval.

THIS PAGE INTENTIONALLY LEFT BLANK

IV. SUMMARY AND CONCLUSIONS

Biharmonic annual fits of currents, temperature and eddy kinetic energy at 300 and 1200 m, adjusted sea levels, and wind stress were constructed for the entire 5-year period of this study and are shown in Figure IV-1, and the goodness of fit for this biharmonic analysis is shown in Table IV-1. The relationship between currents and temperatures at 300 and 1200 m at mooring S2 site, and the relationship between along shore flow, adjusted sea levels and wind stress are described below.

A. CHARACTERISTICS OF CURRENTS OFF MONTEREY, BAY

At 305 m, the flow was dominated by poleward flow associated with the CU and the DC. The speed (direction) of the vector average flow at 305 m was 3.9 ± 0.04 cm/s ($334^\circ \pm 0.5^\circ$) and the variance ellipse was oriented along 349° with a semi-major (semi-minor) axis of 9.4 cm/s (3.4 cm/s). The mean direction was poleward in all months but October when strong equatorward flows in 1999 and 2002 resulted in southward mean flow. The orientation of the variance ellipse appeared to be controlled by the topography immediately to the east of the mooring site.

At 1200 m the speed (direction) of the vector average flow was 0.8 ± 0.02 cm/s ($169^\circ \pm 0.6^\circ$) and the variance ellipse was oriented in the same direction as the mean flow, 350° , with a semi-major (semi-minor) axis of 5.8 cm/s (2.0 cm/s). The direction of the variance ellipses and the mean flow at 1200 m was the same as that for 305 m and coincided with the orientation of the topography immediately to the east of the mooring site. The equatorward direction of the flow was a surprise. Geopotential gradients for layers below 1000 dbar decrease to the west, implying poleward geostrophic flow relative to a deep reference layer. Hickey (1979, 1998) has observed equatorward flow over the upper slope beneath the CU and refers to these flows as the “Washington Undercurrent.” An equatorward undercurrent was also generated during fall and winter in numerical model studies by Batteen and Vance (1998). An alternative explanation might lie in the proximity of the canyon to the mooring site. Mixing processes in the canyon would

reduce the stratification toward the Canyon head and create an up-canyon horizontal pressure gradient that might affect the flow at the S2 site.

The seasonal patterns of variability were modeled by fitting a sinusoid that contained annual and semiannual frequencies to data that was averaged by yearday. The resulting seasonal variability is shown in Fig. IV-1 and summarizes the results discussed previously in Chapter III. The very best results, in terms of the percent of the variance explained (Table IV-1), were for 305 m temperature (84%), Monterey adjusted sea level (90%), and the adjusted sea level difference between Port San Luis and Monterey (74%). The models for alongshore velocity at 305 m, alongshore wind stress, and 1200 m temperature accounted for 36%, 44%, and 58% of the variability, respectively. The models show minimum sea level, 305 m temperature, and maximum equatorward wind stress occur in spring at about yearday 120 and are followed by maximum poleward flow at 305 m in late spring on yearday 170. Minimum poleward flow at 305 m occurred in late winter and early fall, the former coinciding with the maximum poleward pressure gradient at the coast. The co-variation of temperature and sea level confirm the steric balance observed by Lisitzin and Pattullo (1961). The development of the spring poleward jet in the alongshore flow was largely captured by geostrophic adjustment (decrease in sea level and 305 m temperature). The phase difference between alongshore pressure gradient and maximum poleward velocity at 305 m suggests an arrested topographic wave.

The biharmonic models accounted for 37% and 28% of the variability of the kinetic energy at 305 m and 1200 m and 27% of the alongshore velocity at 1200 m. Kinetic energy was minimum in winter and maximum in late summer at about the same time as the equatorward flow at 1200 m was maximum (about yearday 200). The variability of kinetic energy and eddy kinetic energy (Fig. III-16) were in phase at 1200 m while the eddy kinetic energy maximum at 305 m occurred in October (Fig. III-15). The latter suggests baroclinic instability as a possible mechanism in the relaxation of the CU.

Although the biharmonic models reproduce the seasonal velocity trends, they do a poor job of showing the higher frequency, mesoscale variability associated with flows at

305 m and 1200 m. The spring jet at 305 m does not accelerate in the manner depicted in Figure IV-1 but instead consists of a series of fortnightly to monthly bursts of poleward flow followed by relaxations. The same is true for equatorward flows at 1200 m. Poleward mesoscale events were more intense at 305 m while the equatorward mesoscale flows were stronger at 1200 m and suggest that the former are surface trapped and the latter are bottom trapped. Variance preserving spectra show the dominance of about 30 to 60-day periods at both depths.

The 5-year time series of 305 m currents at S2 can be compared to a 5-year time series of 350 m currents in 800 m of water to the west of Point Sur from May 1989 to February 1995 (Collins et al., 1996). At Point Sur (S2) the mean flow was directed toward 334° (334°) at 7.6 cm/s (3.9 cm/s). The variance ellipse at Point Sur (S2) was oriented 345° (349°) with a semi-major axis of 9.7 cm/s (9.4 cm/s) and a semi-minor axis of 4.1 cm/s (3.4 cm/s). The major discrepancy in these statistics is that the mean vector averaged speed of the flow at S2 is about half that at the shallower site at Point Sur. The scatter plot for the velocity observations at Point Sur also showed a few instances of strong southwestward flow that were not observed at S2. The seasonal cycle of temperature and velocity at Point Sur were similar to those for S2 except that the peak poleward flow was about twice that shown in Fig. IV-1 for S2. Finally, the character of the spring jet at Point Sur exhibited less mesoscale variability than S2.

B. RECOMMENDATIONS FOR FUTURE WORK

M2 currently includes an ADCP that typically penetrates to a depth of 300 m (Fig. II-5). It is possible to compare ADCP measurements at M2 and S2 with a view toward eliminating redundant instruments. Figure IV-2 shows a comparison of velocity measurements at 290 m at S2 to 288 m measurements at M2. The M2 measurements were not corrected for mooring motion. Correlations for u and v exceeded 0.8 (Table IV-2) and the slope of the regression line was 0.96 for u and 0.91 for v (for perfect agreement between the measurements, the regression slope and correlation coefficient would be 1). Standard deviations of the differences of u and v were high, ~ 6 cm/s, and the zero intercept for v and speed was -3.0 cm/s and 4.8 cm/s. Compared to u and v , both the speed and direction scatter plots were noisy. The change in slope of the direction

comparisons at 90° suggests compass calibration problems. Since both MBARI and NPS use manufacturer recommended procedures for calibrations, these differences might be due to magnetic deviation created by other instruments on the M2 mooring. Differences in speed and direction might also be caused by motion of M2. Typically, M2 does not move very much during the period of measurement, but occasionally it transits across or around its 3.2 km watch circle when winds or currents change direction. The half-hourly GPS measurements at M2 were used to correct velocity measurements for mooring measurement but the result (not shown) was much noisier than shown in Fig IV-2.

The conclusion from these comparisons is that the extended range ADCP on M2 is suitable for measurements of mesoscale, seasonal and long term flow patterns at 300 m depth. The problems with using M2 ADCP measurements as a time series are due to extended periods of time when the ADCP at M2 does not work (e.g., September 1999 to April 2000), the mooring fails (late 1997 to June 1998), or the transducer faces need cleaning or the power is low (March 2002). Costs associated with improved ADCP operations at M2 may exceed those of the S2 measurements. And although M2 is a suitable platform for monitoring mesoscale flow, it is not a suitable platform for sediment trap measurements and the incremental costs of velocity measurements at a sediment trap are a small fraction of the mooring costs.

Fig. III-1 illustrated the limitations of the RCM-8 paddlewheel. It would be interesting to see how well an ADCP worked at 1200 m, e.g. whether or not there were enough scatterers for Doppler shift measurements over 80 m ranges. If so, the low threshold of the ADCP would aid in resolving speed and direction at least 24% of the time.

			Integer Percent Variance
VELOCITY	300 m	u_r	13
		v_r	36
	1200 m	u_r	7
		v_r	28
TEMPERATURE	300 m		84
	1200 m		58
KINETIC ENERGY	300 m		37
	1200 m		28
ADJUSTED SEA LEVEL	Monterey		90
WIND STRESS	t_r		20
	t_r		44
SEA LEVEL DIFFERENCE			74

Table IV-1. Percent of variance of daily averaged data explained by a biharmonic fit which includes annual and semiannual frequencies.

Variable	Mean Difference (cm/s)	S.D of difference (cm/s)	Slope of regression (cm/s)	Zero intercept (cm/s)	Correlation coefficient (cm/s)
u	0.3	5.9	0.96	-0.5	0.81
v	3.6	6.1	0.91	-3.0	0.86
Speed	-0.5	6.0	0.69	4.8	0.71

Table IV-2 Comparison of ocean current measurements at S2 at 290 m and M2 at 288 m, using acoustic Doppler current profilers from February 8 to August 28, 2002.

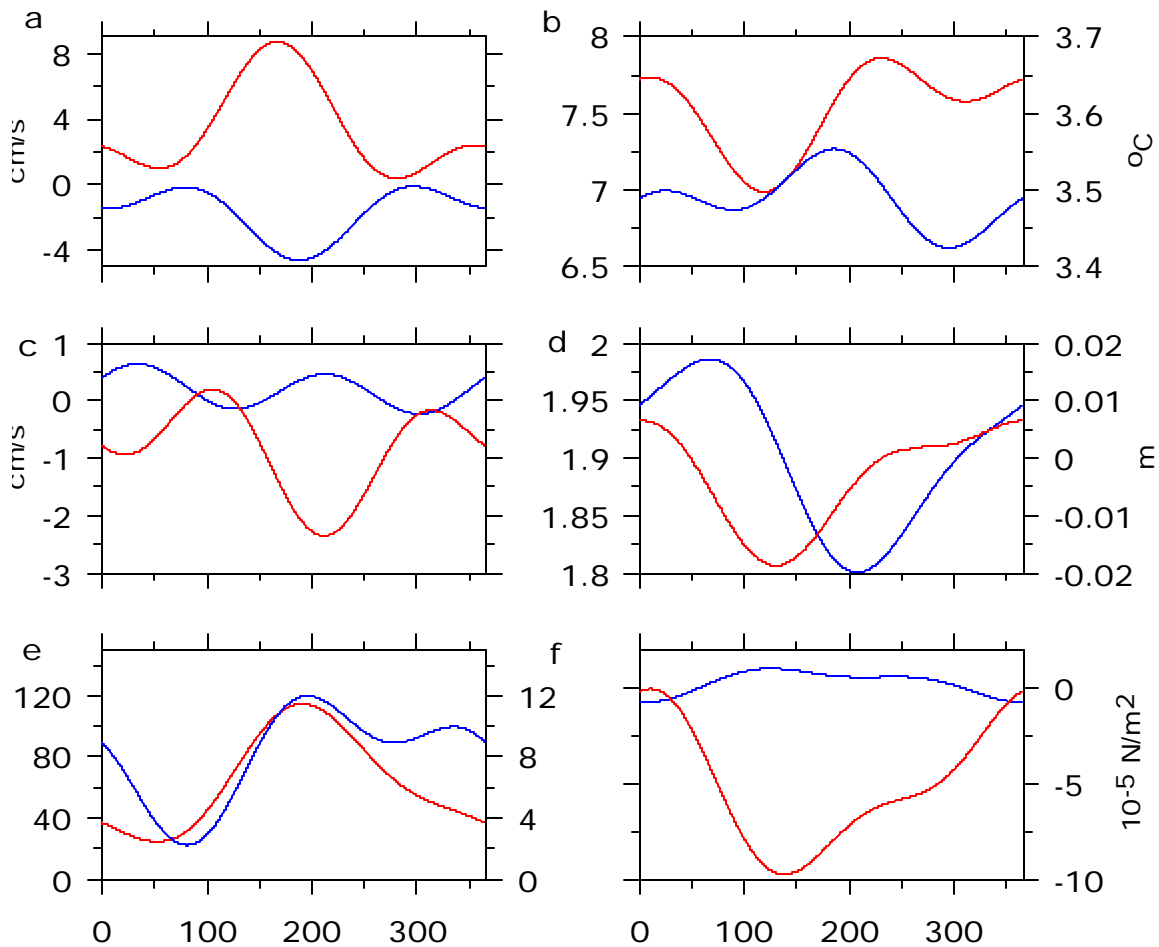


Figure IV-1. Biharmonic fit to daily averaged data. Biharmonic frequencies include annual and semiannual frequencies. (a) Current speed at 300 m. Red (blue) line represents the v_r (u_r) component of currents. (b) Temperature at 300 m (1200 m) is the red (blue) line. (c) Currents at 1200 m. The red (blue) line represents the v_r (u_r) component of currents. (d) ASL difference between Monterey and Port San Luis (blue line) and the ASL at Monterey (red line). (e) Kinetic energy at 300 m (1200 m) is the red line (blue line). (f) Wind stress t_{rx} (t_{ry}) is the blue (red) line.

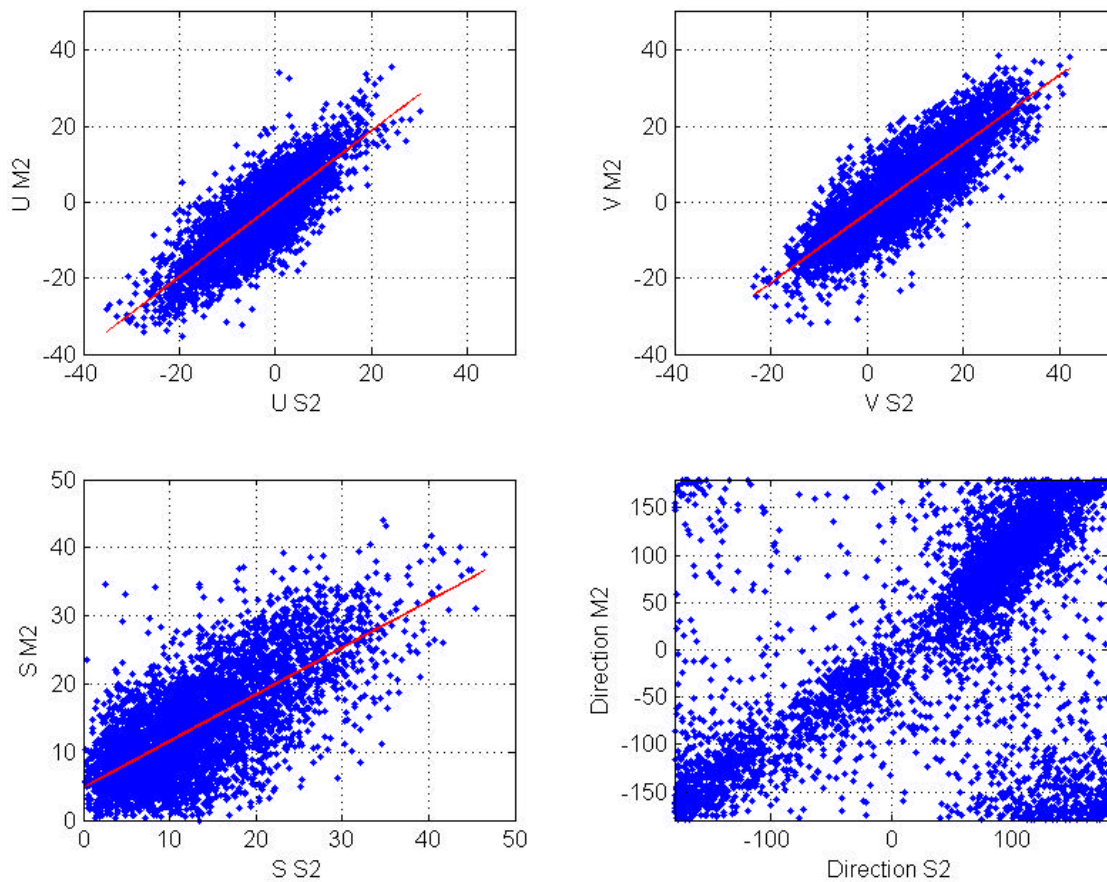


Figure IV-2. Comparison of current measurements at S2 (290 m) and M2 (288 m) using acoustic Doppler current profilers from February 8 to August 28, 2002. Upper left (upper right) east-west (north-south) velocity component. Solid red line is the linear regression of S2 and M2 measurements.

APPENDIX A. TIDAL COMPONENTS

A. HARMONIC ANALYSIS

To understand the nature of tidal currents, an analysis of the various tidal components was performed through harmonic analysis. Traditional harmonic tidal analysis allows us to specify the frequency to be examined and obtain their amplitudes and phase in the least-square sense (Godin, 1972; Emery and Thomson, 1997). Harmonic tidal constituents are dominated by diurnal and semidiurnal motion, followed by fortnightly, monthly, semi-annual, and annual variability.

The advantages with the method of least-squares analysis is that it permits resolution of several hundreds tidal constituents of which 45 are typically astronomical in origin. Both scalar and vector time series can be analyzed. If the record is not sufficiently long to permit the direct resolution of neighboring components in the diurnal and semidiurnal frequency bands the analysis makes provision for the inference and subsequent inclusion of these components in the analysis. Finally, the method allows for gaps in the time series by ignoring those times for which there are no data.

The following excerpt from Foreman (1977) summarizes the Least Squares Fitting method. ‘Assume that a sequence of water observations, y_i and the corresponding times t_i , $i = 1, \dots, N$, at which they occurred are given, one wants to find a function

$$y(t) = A_0 + \sum_{j=1}^M A_j \cos 2\mathbf{p}(\mathbf{s}_j t - \mathbf{f}_j)$$

where \mathbf{s}_j and M are the constituent frequencies and number of constituents, respectively, and are specified beforehand. The amplitudes A_j and phase \mathbf{f}_j remain to be chosen so that the values $y(t_i)$ of the fitting function at the sampling instants t_i agree as well as possible with the contemporaneous observed elevations y_i , that is

$$y_i - \left[A_0 + \sum_{j=1}^m A_j \cos 2\mathbf{p}(\mathbf{s}_j t_i - \mathbf{f}_j) \right] = \mathbf{e}_i \approx 0, \quad i = 1, \dots, N \quad (1)$$

At the observation times, t_i the time derivative $y'(t)$ of the fitting function should be approximately zero, that is

$$y'(t_i) = -\sum_{j=1}^M 2\mathbf{p}\mathbf{s}_j A_j \sin 2\mathbf{p}(\mathbf{s}_j t_i - \mathbf{f}_j) = \mathbf{d}_i \approx 0 \quad (2)$$

When the number of arbitrary constants $(2M+1)$ in the expression for $y(t)$ is less than $2N$, the fitting error \mathbf{e}_i and \mathbf{d}_i cannot be reduced exactly to zero, to satisfy the equations (2) and (3). A commonly adopted method in such over-determined problems is to minimize the sum of the squares of error at the observation times, which means, choosing the A_j and \mathbf{f}_j so as to minimize the error function

$$E = \sum_{i=1}^N \left\{ [y_i - y(t_i)]^2 + [wy'(t_i)]^2 \right\} = \sum_{i=1}^n \{ \mathbf{e}_i^2 + \mathbf{w}^2 \mathbf{d}_i^2 \} \quad (3)$$

That is, to find a least squares fit to the available data. \mathbf{w} in equation (3) represent an arbitrary positive weighting coefficient that permits control of the emphasis to be placed on satisfying the zero derivative condition compared to that placed on having $y(t)$ fit the observed elevations accurately.”

In the case of observed current velocities the least square method minimizes the difference between the observed current velocity and the sum of the solutions corresponding to that observation. The difference, or error, can be attributed to unsolved tidal constituents, inertial currents or noise in the signal. The extracted solution reflects only those current variations with a coherent phase and no assumptions are made about data outside the interval upon which the solution are fit (Pugh, 1986).

The analysis of tidal constituents requires observational periods that are normally multiples of synoptic periods involving the most important tidal constituents. The preferred record length for a complete tidal analysis is 369 days. This allows extraction of the amplitude and phase of at least 64 of the largest tidal constituents (Dronkers, 1964).

Tables A-1 and A-2 shown the principal tidal constituents at 305 and 1200 m calculated by using the Matlab™ function t_tide that used the method described by Pawlowicz et al. (2002). The record length used was 1718 days with a sampling interval of 30 min.

NAME	freq cph	major cm/s	emaj cm/s	minor cm/s	emin cm/s	inc	einc	pha	epha	snr
*SA	0.0001141	3.509	1.616	0.692	1.34	116.06	24.35	161.96	28.95	4.7
*SSA	0.0002282	2.432	1.679	0.694	1.14	117.86	38.00	181.57	42.88	2.1
MSM	0.0013098	0.460	1.107	0.101	0.94	96.39	84.81	156.88	180.13	0.17
MM	0.0015122	0.706	0.997	0.010	1.16	29.61	118.50	220.36	125.76	0.5
MSF	0.0028219	0.480	1.169	-0.042	0.96	134.76	86.84	68.71	171.58	0.17
MF	0.0030501	0.197	1.023	-0.021	0.96	124.11	100.52	299.40	224.83	0.037
ALP1	0.0343966	0.101	0.161	-0.066	0.14	168.33	129.34	309.60	156.39	0.4
2Q1	0.0357064	0.078	0.143	-0.066	0.16	100.71	135.45	251.16	159.61	0.3
SIG1	0.0359087	0.184	0.169	-0.124	0.18	46.71	100.29	246.84	93.13	1.2
Q1	0.0372185	0.140	0.172	0.038	0.17	22.48	114.53	114.02	91.29	0.67
RHO1	0.0374209	0.122	0.167	-0.079	0.17	158.17	120.61	194.87	140.75	0.53
*O1	0.0387307	0.402	0.212	0.191	0.20	133.04	46.92	212.12	51.35	3.6
TAU1	0.0389588	0.086	0.153	-0.042	0.14	57.53	108.05	257.72	140.07	0.31
BET1	0.0400404	0.096	0.165	-0.047	0.16	83.04	117.26	133.66	142.81	0.34
NO1	0.0402686	0.280	0.299	-0.254	0.34	10.06	137.18	125.88	145.14	0.88
CHI1	0.0404710	0.106	0.160	-0.042	0.15	28.29	99.70	81.49	125.59	0.44
PI1	0.0414385	0.170	0.176	-0.093	0.17	142.90	89.74	65.22	117.11	0.92
*P1	0.0415526	0.290	0.182	-0.014	0.21	96.88	40.53	180.17	40.58	2.5
S1	0.0416667	0.148	0.183	-0.072	0.19	124.91	107.72	131.77	130.40	0.65
*K1	0.0417807	0.566	0.193	0.263	0.19	94.91	31.49	188.28	31.78	8.6
*PSI1	0.0418948	0.282	0.158	-0.268	0.17	167.81	133.89	149.71	132.56	3.2
PHI1	0.0420089	0.119	0.146	-0.080	0.17	70.49	121.81	342.67	137.52	0.67
THE1	0.0430905	0.066	0.152	-0.001	0.14	14.96	120.89	151.23	176.53	0.19
J1	0.0432929	0.182	0.161	-0.131	0.17	117.98	102.93	261.85	106.62	1.3
SO1	0.0446027	0.183	0.182	-0.147	0.19	21.67	125.25	140.89	112.34	1
OO1	0.0448308	0.158	0.220	-0.019	0.21	154.96	101.75	288.39	119.99	0.51
UPS1	0.0463430	0.209	0.200	-0.119	0.20	179.70	99.06	231.98	100.98	1.1
OQ2	0.0759749	0.114	0.142	-0.068	0.15	179.92	112.51	103.90	106.90	0.65
EPS2	0.0761773	0.070	0.127	-0.027	0.13	155.12	118.80	352.64	173.20	0.3
2N2	0.0774871	0.190	0.143	-0.133	0.14	2.86	94.01	26.94	96.16	1.8
MU2	0.0776895	0.162	0.148	-0.097	0.14	71.92	83.09	205.72	98.79	1.2
*N2	0.0789992	0.498	0.186	-0.150	0.19	125.79	24.54	175.00	24.42	7.2
NU2	0.0792016	0.140	0.158	-0.028	0.16	159.46	99.57	197.73	103.86	0.78
GAM2	0.0803090	0.012	0.096	-0.004	0.09	161.47	141.87	336.86	270.08	0.016
*H1	0.0803973	0.574	0.168	-0.362	0.18	127.38	37.13	223.32	40.06	12
*M2	0.0805114	0.988	0.201	0.308	0.20	109.14	12.75	171.57	12.98	24
*H2	0.0806255	0.311	0.179	-0.129	0.16	117.09	42.97	330.44	46.90	3
MKS2	0.0807396	0.238	0.180	-0.203	0.19	28.51	108.46	234.69	102.27	1.7
LDA2	0.0818212	0.072	0.129	0.012	0.14	1.55	127.44	272.47	126.21	0.31
L2	0.0820236	0.048	0.111	-0.023	0.11	101.65	123.31	238.53	159.12	0.18
*T2	0.0832193	0.238	0.160	-0.198	0.17	91.83	98.33	265.36	104.74	2.2
*S2	0.0833333	1.072	0.206	-0.580	0.19	130.83	16.19	215.04	16.30	27
*R2	0.0834474	0.240	0.133	-0.201	0.13	126.18	97.83	266.33	102.79	3.3
K2	0.0835615	0.240	0.181	-0.139	0.17	142.49	74.91	223.72	78.45	1.8
MSN2	0.0848455	0.088	0.147	-0.050	0.13	27.10	125.56	115.49	158.62	0.36
ETA2	0.0850736	0.160	0.165	-0.104	0.15	49.21	85.03	347.60	92.03	0.94
MO3	0.1192421	0.044	0.054	-0.017	0.06	54.90	102.31	254.07	103.66	0.66
M3	0.1207671	0.046	0.052	0.001	0.05	91.68	81.69	14.73	87.52	0.77
SO3	0.1220640	0.054	0.057	-0.027	0.05	172.96	97.94	145.94	100.41	0.9
MK3	0.1222921	0.055	0.054	-0.024	0.05	23.73	88.71	326.64	89.85	1
*SK3	0.1251141	0.093	0.061	-0.046	0.06	153.84	56.87	189.28	64.39	2.4
MN4	0.1595106	0.016	0.041	-0.004	0.04	130.75	134.93	284.11	174.37	0.15
*M4	0.1610228	0.100	0.057	-0.022	0.06	44.23	36.77	118.37	37.79	3.1
SN4	0.1623326	0.031	0.047	0.001	0.04	136.54	108.72	85.48	113.13	0.45
MS4	0.1638447	0.068	0.056	-0.012	0.05	56.62	62.32	148.97	59.36	1.5
MK4	0.1640729	0.057	0.051	-0.025	0.06	108.15	80.49	207.21	84.93	1.2
S4	0.1666667	0.021	0.045	-0.009	0.04	121.25	137.44	341.67	147.41	0.21
SK4	0.1668948	0.070	0.050	-0.060	0.06	59.16	122.39	58.35	114.95	1.9
2MK5	0.2028035	0.032	0.029	-0.015	0.03	116.50	98.06	220.37	86.92	1.2

Table A-1. Major harmonic tidal constituents at 305 m depth. Amplitudes and phases are relative to Greenwich central time. A Raleigh criterion of 0.1 was used. The percent of variance predicted / variance original is 2.5%. The technique used follows Pawlowicz et al. 2002.

NAME	freq cph	major cm/s	emaj cm/s	minor cm/s	emin cm/s	inc	einc	pha	epha	snr
SA	0.0001141	0.717	0.712	-0.052	0.43	83.09	35.61	27.15	63.82	1
SSA	0.0002282	0.804	0.686	0.078	0.49	113.25	34.51	52.06	46.21	1.4
MSM	0.0013098	0.328	0.461	-0.145	0.48	168.20	127.77	18.59	161.59	0.51
MM	0.0015122	0.106	0.372	0.033	0.38	2.08	176.75	202.38	198.40	0.081
MSF	0.0028219	0.129	0.435	0.069	0.37	97.35	86.03	20.60	200.21	0.087
MF	0.0030501	0.291	0.477	-0.033	0.39	89.42	67.45	280.22	138.68	0.37
ALP1	0.0343966	0.018	0.085	-0.002	0.07	112.61	141.74	265.14	195.06	0.042
2Q1	0.0357064	0.041	0.088	-0.008	0.08	38.22	130.18	259.24	165.61	0.22
SIG1	0.0359087	0.021	0.078	-0.005	0.07	101.90	144.93	112.00	215.93	0.07
Q1	0.0372185	0.073	0.083	-0.005	0.09	167.22	91.00	234.48	110.34	0.76
RHO1	0.0374209	0.024	0.083	-0.011	0.08	124.31	135.34	19.69	186.49	0.086
O1	0.0387307	0.143	0.110	-0.009	0.10	117.77	57.76	57.67	51.97	1.7
TAU1	0.0389588	0.046	0.067	-0.020	0.07	88.90	121.62	155.59	132.92	0.47
BET1	0.0400404	0.038	0.079	0.004	0.07	150.01	106.35	36.34	183.60	0.23
NO1	0.0402686	0.068	0.171	0.033	0.17	131.51	134.26	199.88	142.44	0.16
CHI1	0.0404710	0.031	0.085	0.005	0.07	150.65	135.73	28.87	222.64	0.14
PI1	0.0414385	0.073	0.090	-0.033	0.09	111.49	108.83	253.98	101.47	0.66
*P1	0.0415526	0.151	0.101	-0.022	0.09	155.63	44.82	106.10	48.07	2.2
S1	0.0416667	0.087	0.111	-0.011	0.11	32.19	96.98	171.27	111.12	0.61
*K1	0.0417807	0.513	0.113	-0.080	0.11	143.01	14.95	43.59	13.48	21
*PSI1	0.0418948	0.141	0.099	0.024	0.09	115.97	52.82	146.64	49.39	2
PHI1	0.0420089	0.077	0.084	-0.021	0.09	163.10	89.35	341.21	105.48	0.84
THE1	0.0430905	0.058	0.092	-0.041	0.07	81.21	121.77	193.83	138.04	0.39
J1	0.0432929	0.064	0.084	-0.024	0.09	134.06	97.60	116.42	130.57	0.57
SO1	0.0446027	0.082	0.107	-0.059	0.09	157.73	106.17	111.02	113.97	0.58
OO1	0.0448308	0.059	0.109	-0.047	0.12	9.28	131.43	154.80	165.80	0.29
UPS1	0.0463430	0.047	0.092	-0.026	0.10	23.83	113.64	103.62	152.35	0.26
OQ2	0.0759749	0.044	0.099	0.003	0.08	6.94	113.87	113.79	156.78	0.2
EPS2	0.0761773	0.104	0.102	-0.058	0.11	144.33	91.46	251.99	103.98	1
2N2	0.0774871	0.086	0.107	-0.030	0.09	113.49	113.84	36.08	99.12	0.64
MU2	0.0776895	0.040	0.112	0.025	0.10	31.42	131.84	201.08	175.50	0.13
N2	0.0789992	0.183	0.146	0.056	0.12	152.41	62.08	116.96	63.43	1.6
NU2	0.0792016	0.155	0.119	-0.106	0.12	113.24	94.15	60.35	85.67	1.7
*GAM2	0.0803090	0.295	0.133	0.013	0.13	16.61	24.89	176.25	25.87	4.9
H1	0.0803973	0.154	0.124	-0.059	0.14	158.90	69.97	166.18	69.30	1.5
*M2	0.0805114	0.786	0.160	-0.008	0.15	53.77	11.66	179.64	10.86	24
*H2	0.0806255	0.282	0.128	-0.211	0.14	10.83	74.04	132.44	75.87	4.8
*MKS2	0.0807396	0.242	0.138	-0.152	0.15	90.74	74.36	183.56	73.48	3.1
LDA2	0.0818212	0.111	0.116	-0.041	0.12	168.60	96.48	151.79	129.30	0.92
L2	0.0820236	0.080	0.109	-0.062	0.11	138.66	131.53	110.08	138.74	0.54
T2	0.0832193	0.101	0.134	-0.020	0.11	20.51	93.93	89.49	109.98	0.56
*S2	0.0833333	0.648	0.166	-0.077	0.16	57.32	14.09	145.16	14.59	15
R2	0.0834474	0.089	0.099	-0.046	0.10	50.80	91.74	189.14	100.14	0.8
K2	0.0835615	0.180	0.132	0.009	0.13	35.91	59.00	102.56	65.97	1.8
MSN2	0.0848455	0.073	0.107	-0.047	0.12	149.90	126.87	143.08	110.74	0.46
ETA2	0.0850736	0.024	0.112	0.012	0.09	93.65	143.80	154.30	218.69	0.047
MO3	0.1192421	0.015	0.039	0.009	0.04	75.59	121.57	174.62	138.74	0.15
M3	0.1207671	0.043	0.041	-0.026	0.04	177.37	103.20	73.15	112.02	1.1
SO3	0.1220640	0.027	0.037	-0.002	0.04	118.99	102.70	179.03	114.39	0.54
*MK3	0.1222921	0.059	0.042	0.018	0.04	122.59	63.40	229.31	66.27	2
SK3	0.1251141	0.021	0.040	-0.004	0.04	5.91	109.27	336.37	156.37	0.28
MN4	0.1595106	0.046	0.043	0.004	0.05	35.20	67.68	7.95	69.85	1.1
*M4	0.1610228	0.073	0.048	0.020	0.05	41.03	48.26	208.92	46.64	2.3
*SN4	0.1623326	0.069	0.041	-0.059	0.04	87.52	109.47	16.01	112.77	2.9
MS4	0.1638447	0.018	0.037	-0.001	0.03	94.58	114.98	109.37	176.02	0.24
MK4	0.1640729	0.047	0.051	-0.000	0.04	170.23	83.96	350.97	81.19	0.85
S4	0.1666667	0.011	0.032	-0.000	0.03	52.42	132.05	80.51	194.02	0.13
SK4	0.1668948	0.051	0.051	-0.023	0.05	88.20	85.83	100.44	91.52	1
2MK5	0.2028035	0.035	0.029	-0.014	0.03	100.75	65.90	19.97	67.88	1.5

Table A-2. Major harmonic tidal constituents at 1200 m depth. Amplitudes and phases are relative to Greenwich central time. A Raleigh criterion of 0.1 was used. The percent of variance predicted / variance original is 2.5%. The technique used follows Pawlowicz et al. 2002.

THIS PAGE INTENTIONALLY LEFT BLANK

APPENDIX B. ROTARY SPECTRA ANALYSIS

Spectral Analysis is used to determine how the variance of a time series is distributed over frequency. Rotary energy analysis was performed on the raw current meter data using Matlab™ programs, based on the discrete Fourier transform and the periodogram method. A Hanning window is applied with a 50% overlap to ensure correct confidence levels (the confidence interval for all spectra is 95%). As is usual practice, the mean and trend of the time series were removed before analysis.

A. Rotary Spectra

Any band-limited series of horizontal velocity can be considered as a realization of a continuous, stationary, stochastic process with a zero mean and constant variance (Pugh, 1986). Fast Fourier Transform algorithms may be used to partition the sample variance among frequency bands.

For rotary spectra analysis, velocity components u and v are combined into complex vector $w = u - iv$. These complex velocities are decomposed into clockwise and counterclockwise motions, and transformed into negative and positive frequencies, respectively. The following excerpt from Mooers (1973) summarizes the rotary spectra analysis.

Consider that a typical realization for an arbitrary frequency band, $f \pm \Delta f$, for the horizontal velocity w is :

$$w = u + iv$$

Where the components u and v are arbitrary sinusoids

$$u(t) = a_1(f)\cos(2\pi ft) + b_1(f)\sin(2\pi ft) \quad (1)$$

$$v(t) = a_2(f)\cos(2\pi ft) + b_2(f)\sin(2\pi ft) \quad (2)$$

Replacing $\cos(2\mathbf{p}ft)$ and $\sin(2\mathbf{p}ft)$ by complex exponential and rearranging terms

$$\mathbf{w} = u + iv = \left(\frac{a_1 + b_2}{2} \right) e^{i2\mathbf{p}ft} + i \left(\frac{a_2 - b_1}{2} \right) e^{i2\mathbf{p}ft} + \left(\frac{a_1 - b_2}{2} \right) e^{i2\mathbf{p}ft} + i \left(\frac{a_2 + b_1}{2} \right) e^{i2\mathbf{p}ft}$$

The rotary spectrum is derived (Gonella, 1972) by considering a transformation of variables from set (a_1, a_2, b_1, b_2) to a set $(A, C, \mathbf{h}, \mathbf{z})$ such that

$$\mathbf{w} = u + iv = A e^{i\mathbf{h}} e^{i2\mathbf{p}ft} + C e^{-i\mathbf{z}} e^{-i2\mathbf{p}t}$$

In the hodograph plane

$A + C$ = Length of the semi-major axis of the ellipse

$|A - C|$ = Length of the semi-minor axis of the ellipse

$\frac{(\mathbf{h} - \mathbf{z})}{2}$ = Direction of the major axis

$\frac{(\mathbf{h} + \mathbf{z})}{2}$ = Temporal phase of the ellipse

The amplitude A and C corresponds to the counterclockwise and clockwise component of the motion, respectively. The rotary spectrum is a plot of $2TA^2$ vs. frequency at positive frequencies, where T is the record length in time.

The transformation used for the analysis is

$$A = \frac{1}{2} \left[(b_2 + a_1)^2 + (a_2 - b_1)^2 \right]^{\frac{1}{2}}$$

$$C = \frac{1}{2} \left[(b_2 - a_1)^2 + (a_2 + b_1)^2 \right]^{\frac{1}{2}}$$

$$\tan \mathbf{h} = \frac{a_2 - b_1}{a_1 + b_2}$$

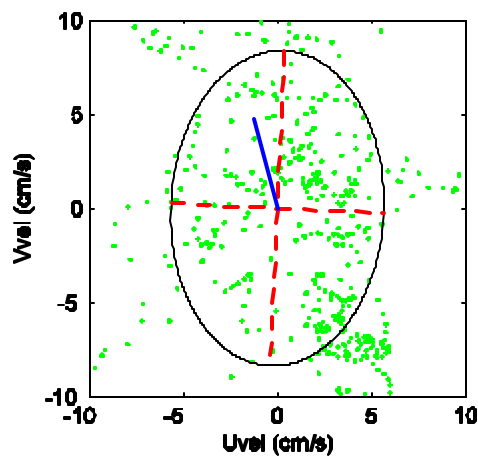
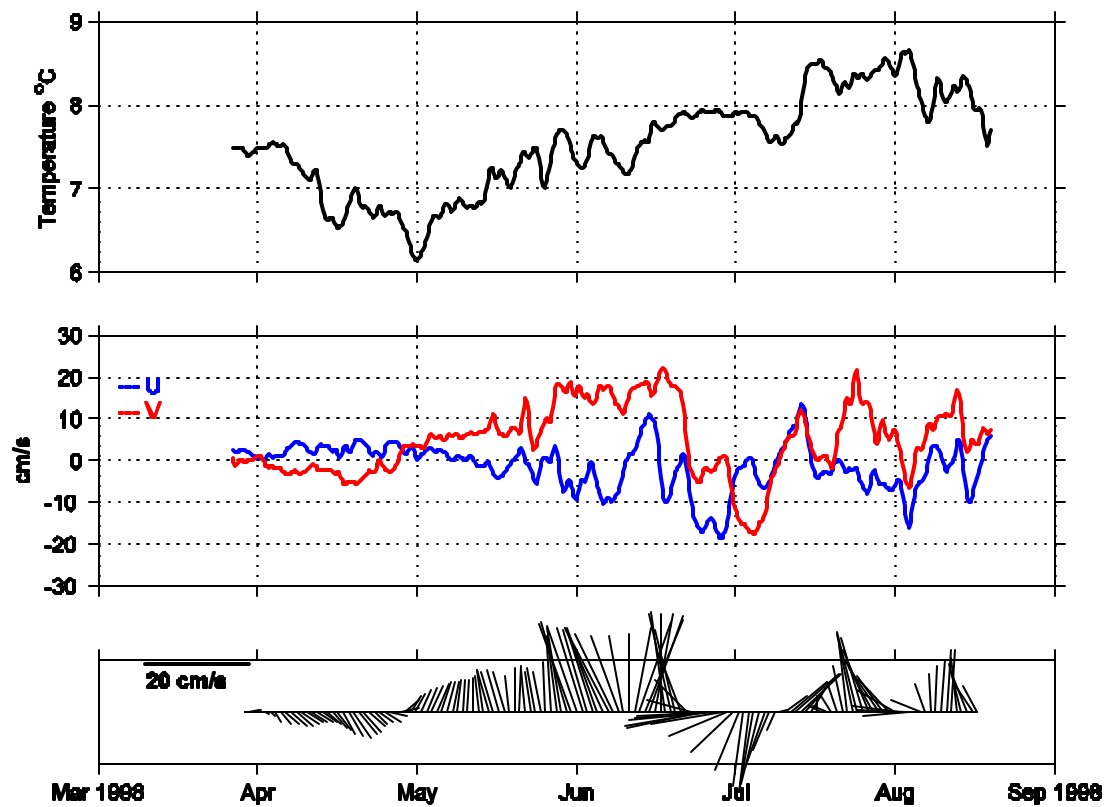
$$\tan \mathbf{z} = \frac{a_2 + b_1}{b_2 - a_1}$$

where A and C are the amplitude of w at positive and negative frequencies respectively.

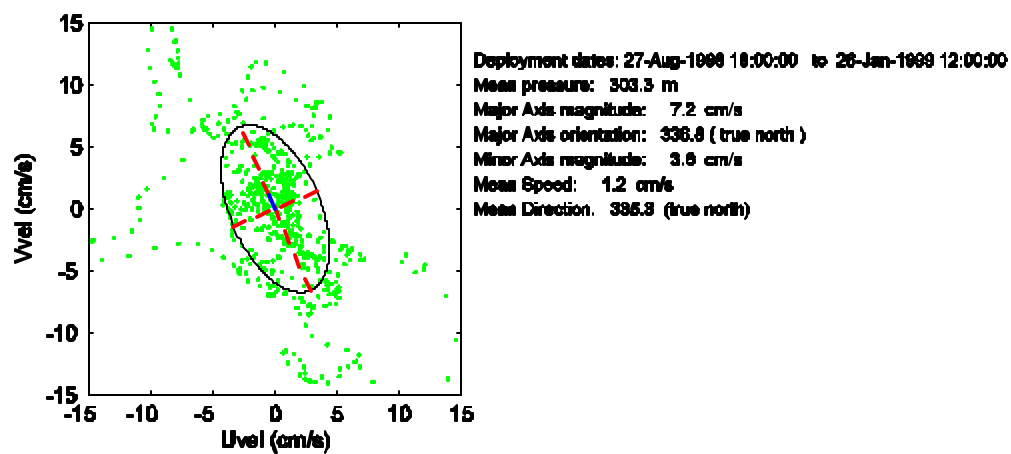
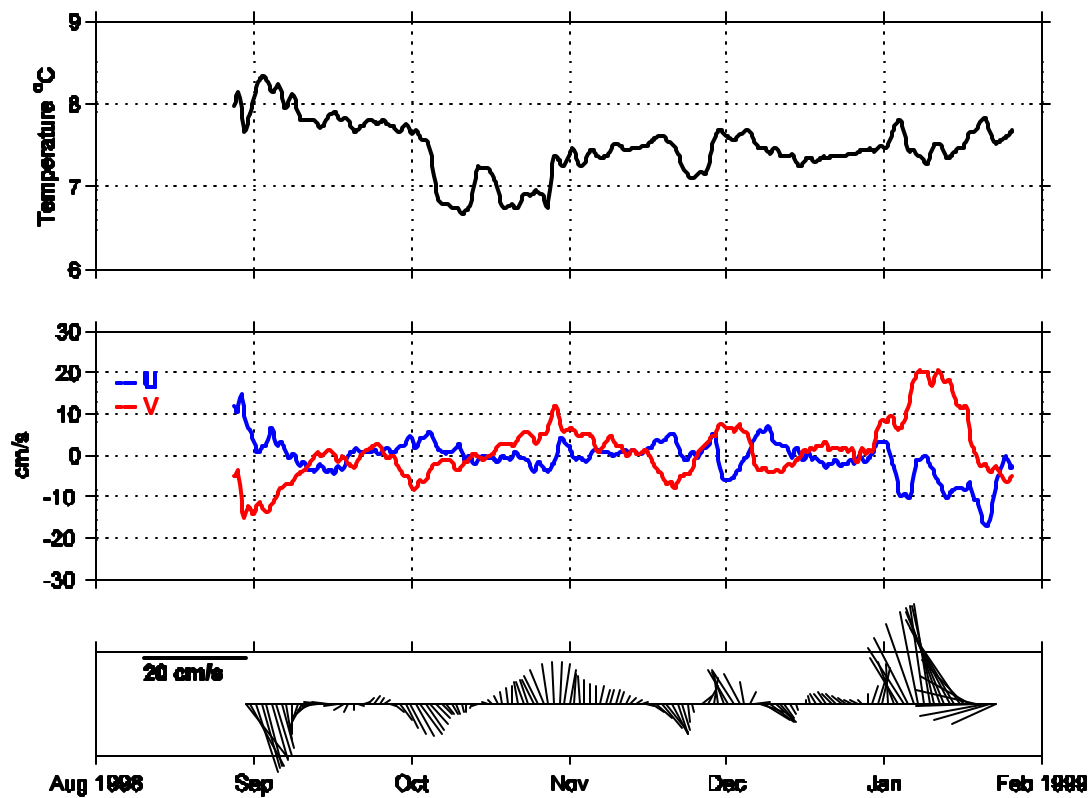
THIS PAGE INTENTIONALLY LEFT BLANK

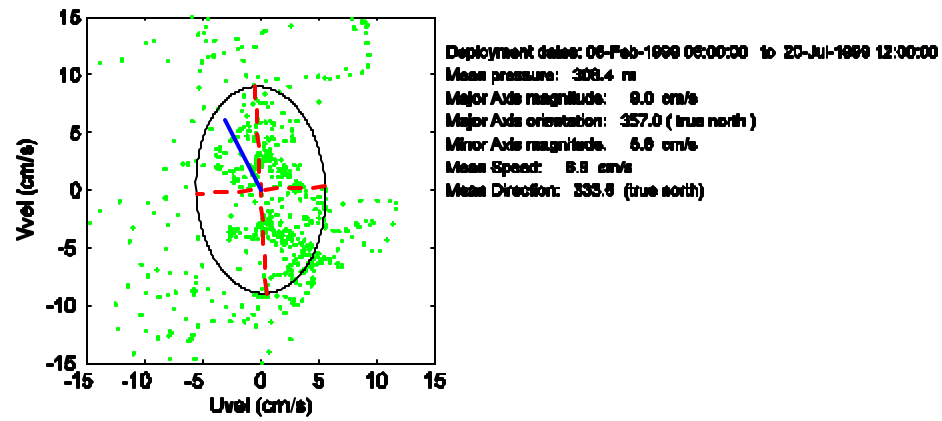
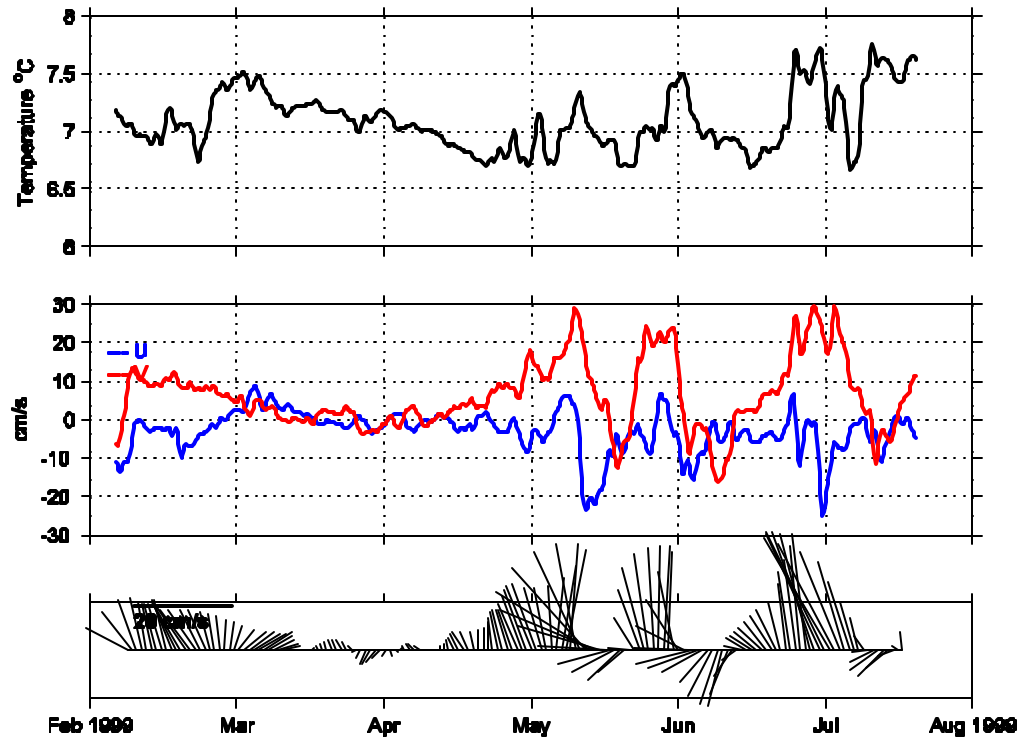
APPENDIX C. TIME SERIES OF CURRENTS AND TEMPERATURES, MEANS AND ELLIPSES PARAMETERS BY DEPLOYMENT AT 305 AND 1200 M

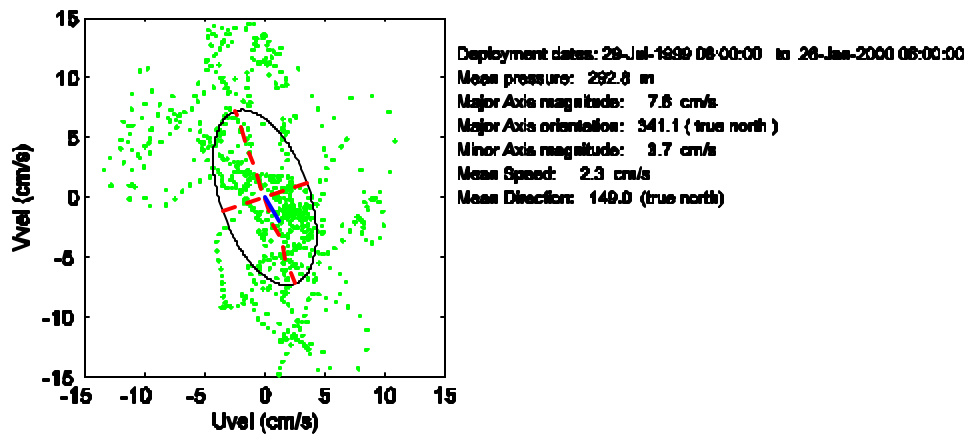
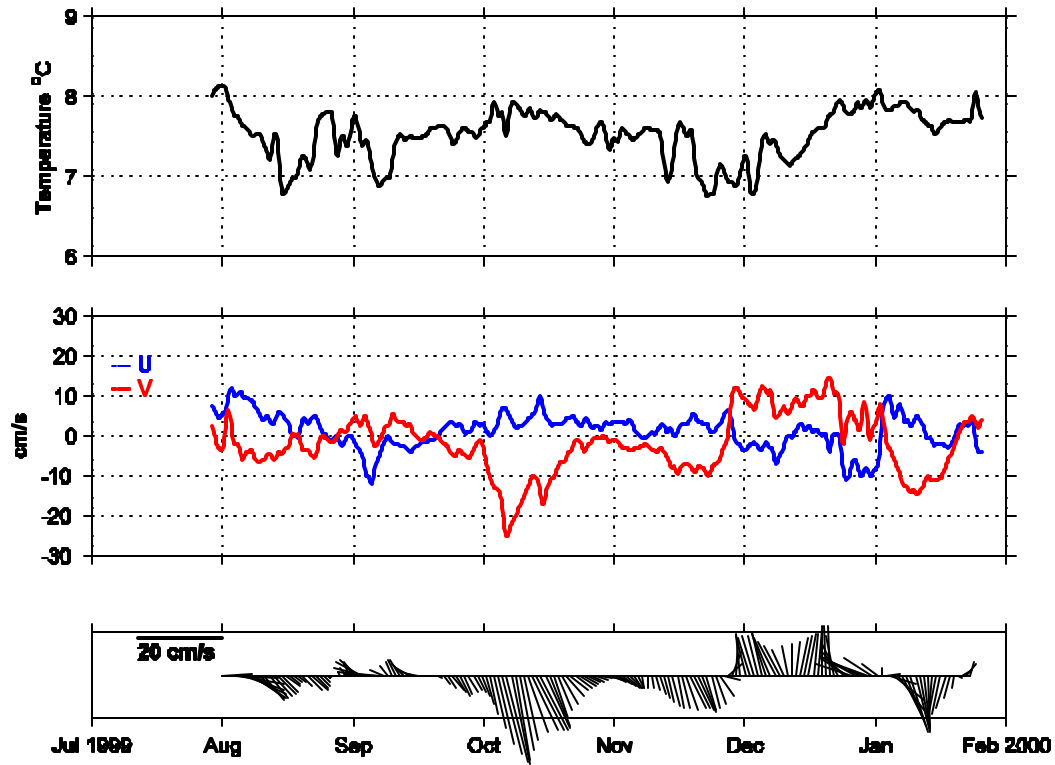
The figures in this appendix serve as a data record and document the data for each deployment. Time series of daily currents and temperatures, means and ellipses parameters at 305 and 1200 m were determined using 6-hour data by deployment.

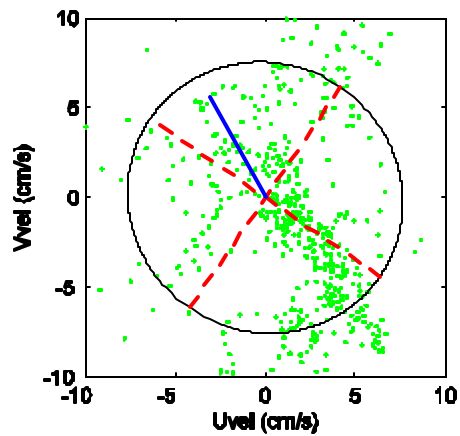
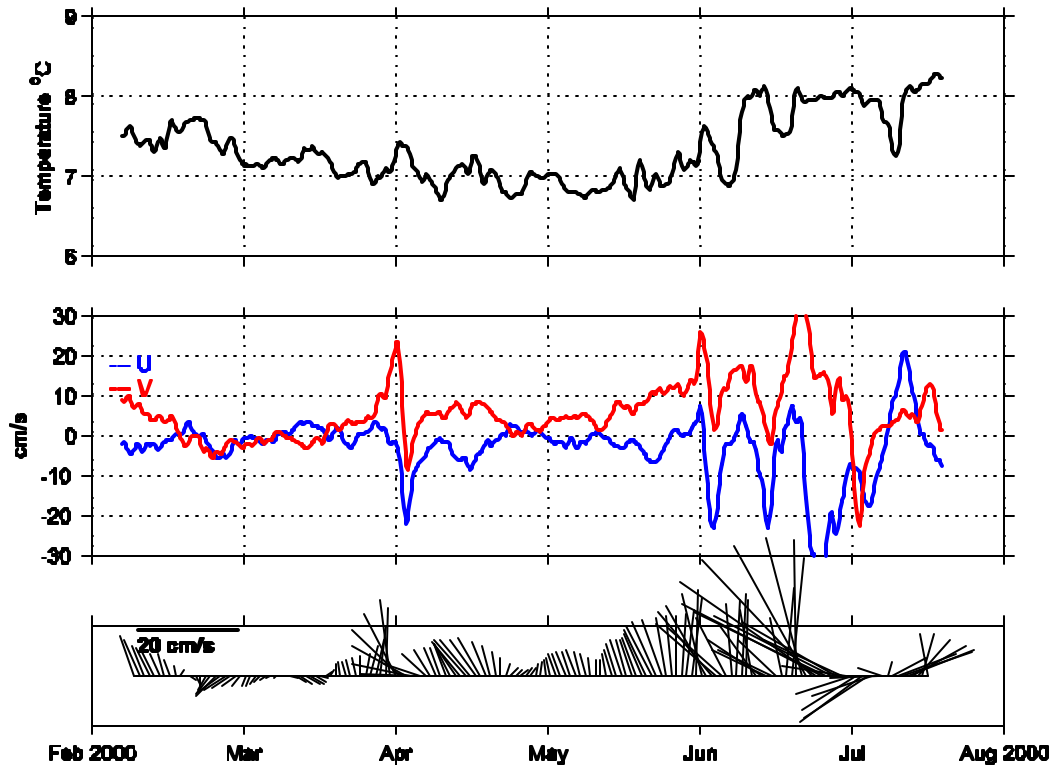


Deployment dates: 26-Mar-1998 18:00:00 to 19-Aug-1998 16:00:00
 Mean pressure: 294.7 m
 Major Axis magnitude: 8.4 cm/s
 Major Axis orientation: 182.6 (true north)
 Minor Axis magnitude: 5.7 cm/s
 Mean Speed: 4.9 cm/s
 Mean Direction: 345.0 (true north)









Deployment dates: 07-Feb-2000 08:00:00 to 18-Jul-2000 12:00:00

Mean pressure: 294.7 m

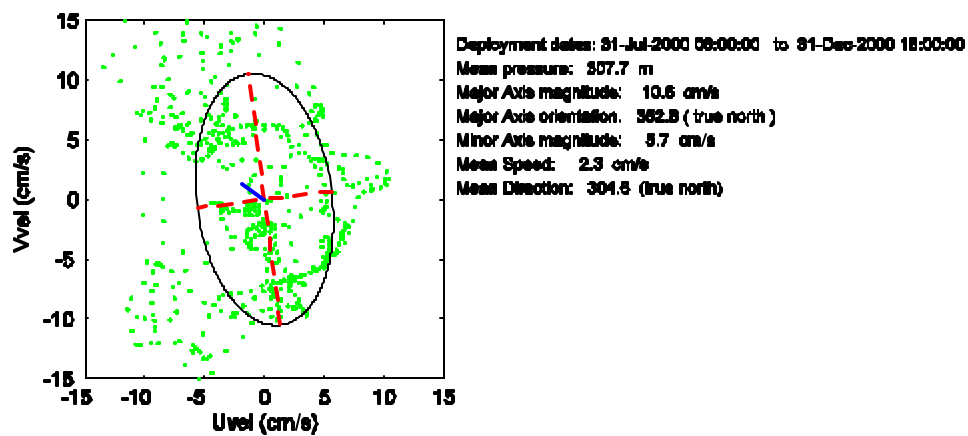
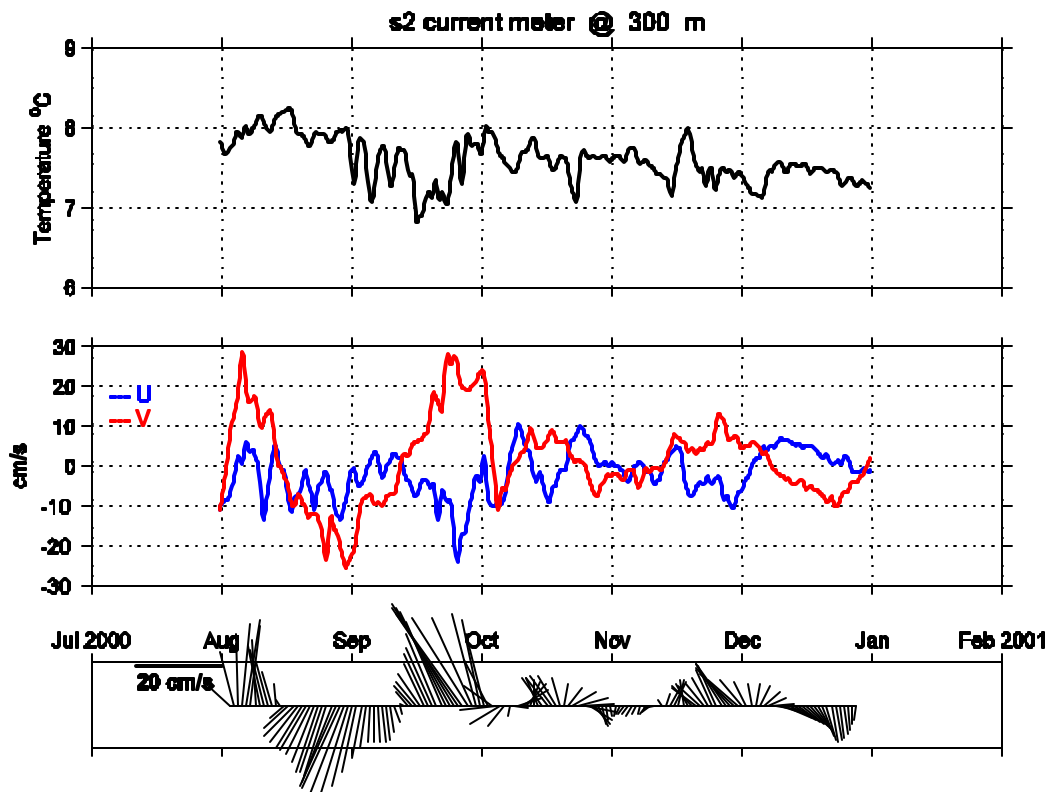
Major Axis magnitude: 7.8 cm/s

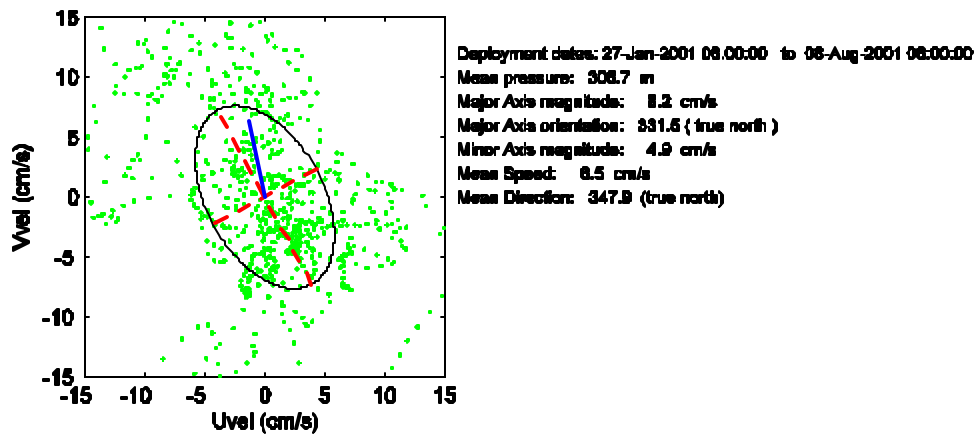
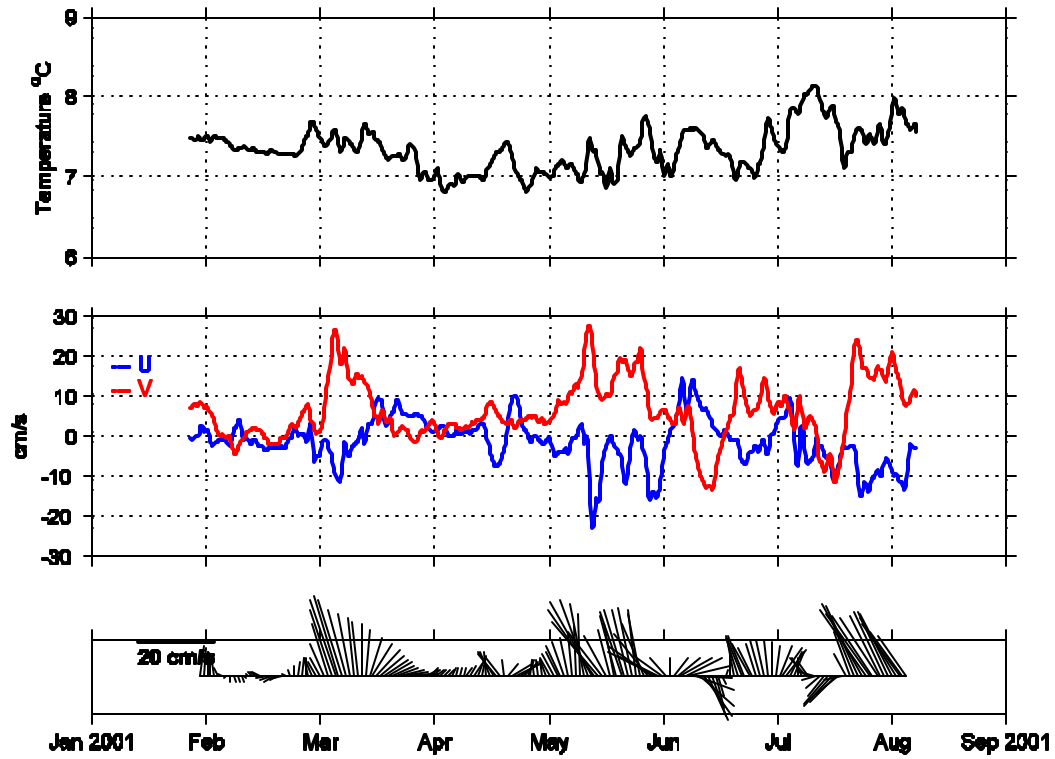
Major Axis orientation: 304.4 (true north)

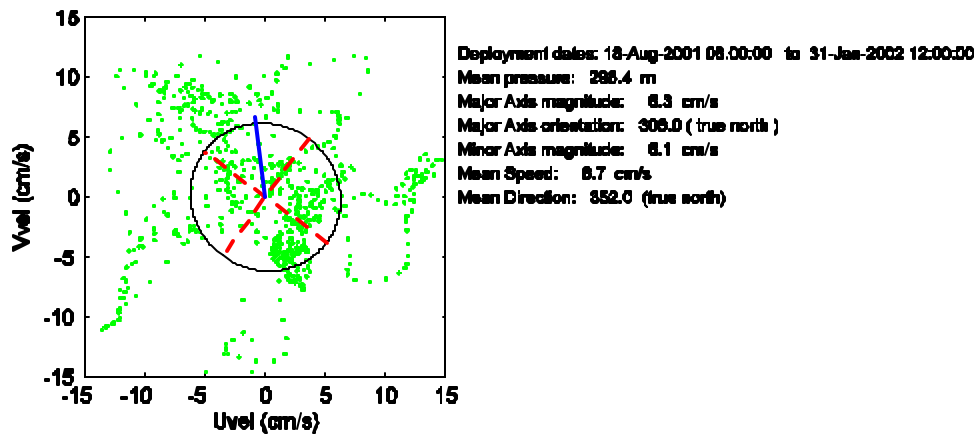
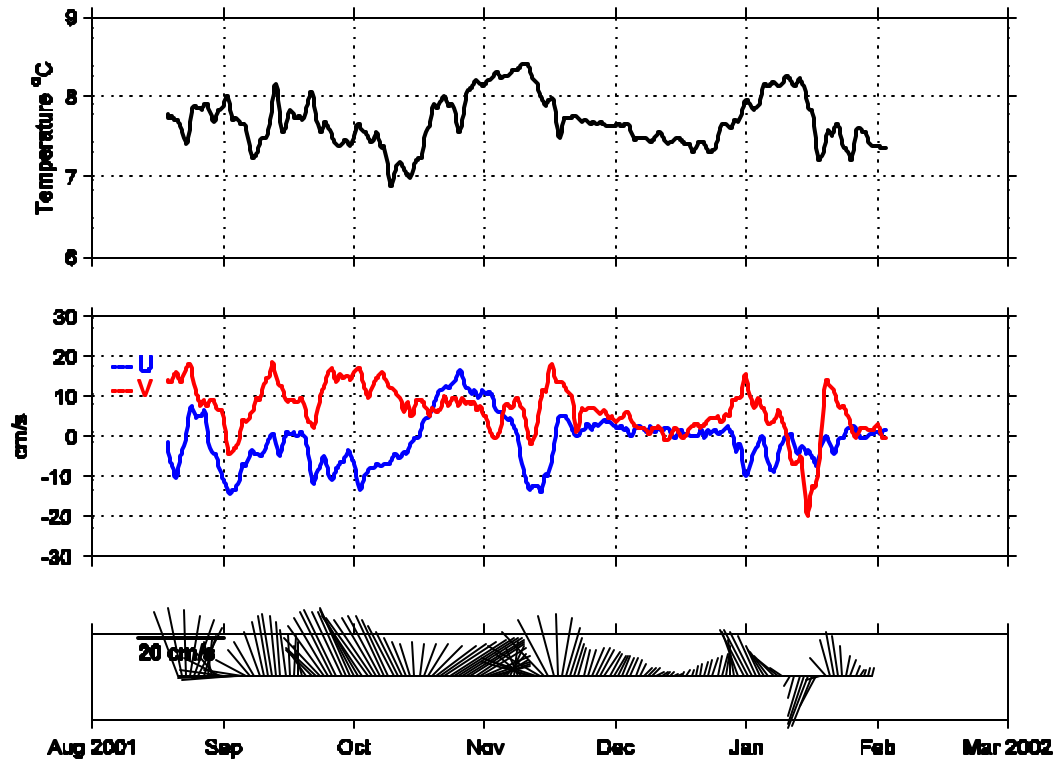
Minor Axis magnitude: 7.4 cm/s

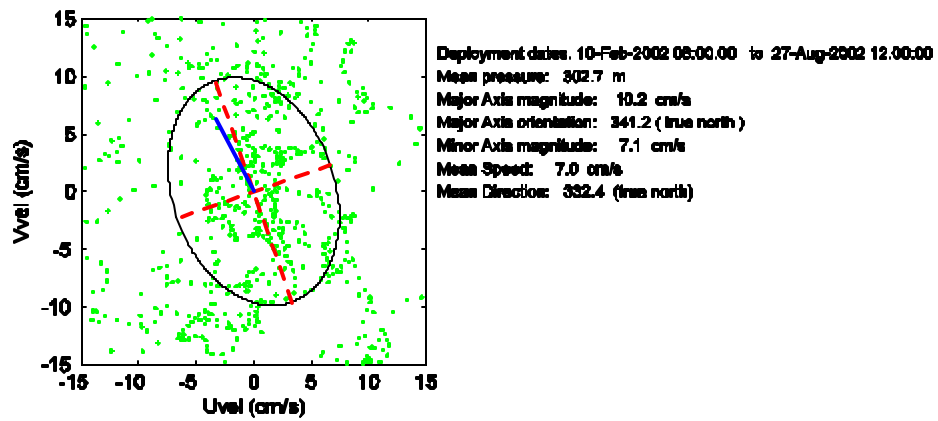
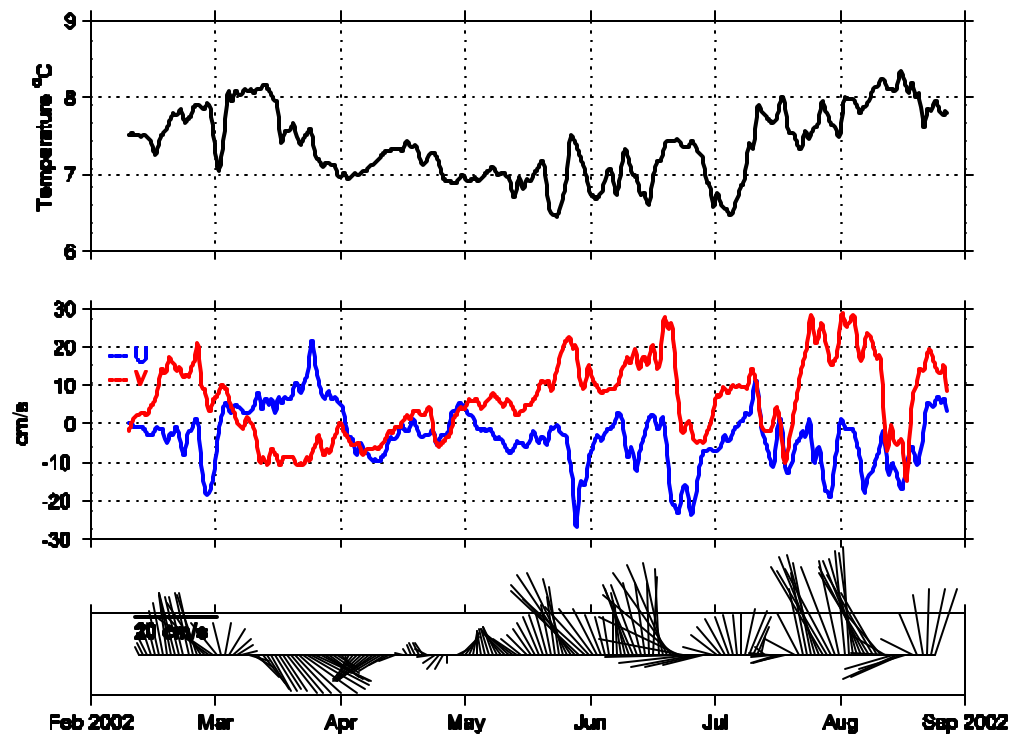
Mean Speed: 6.4 cm/s

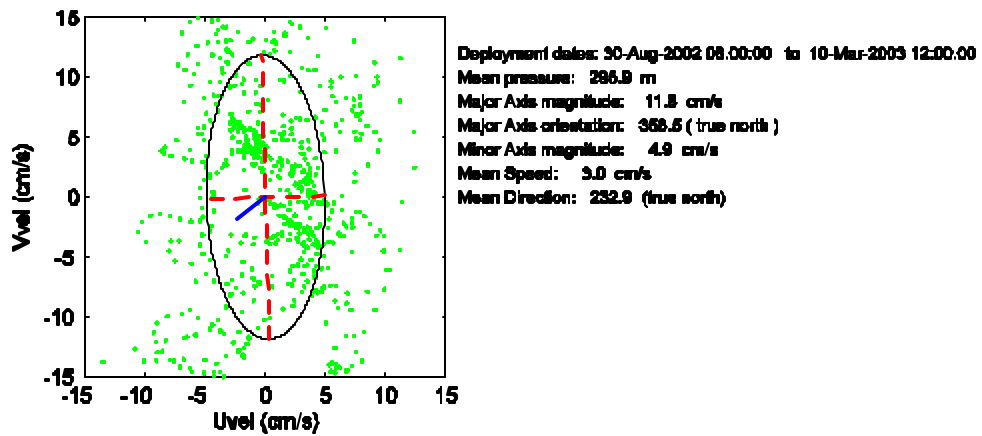
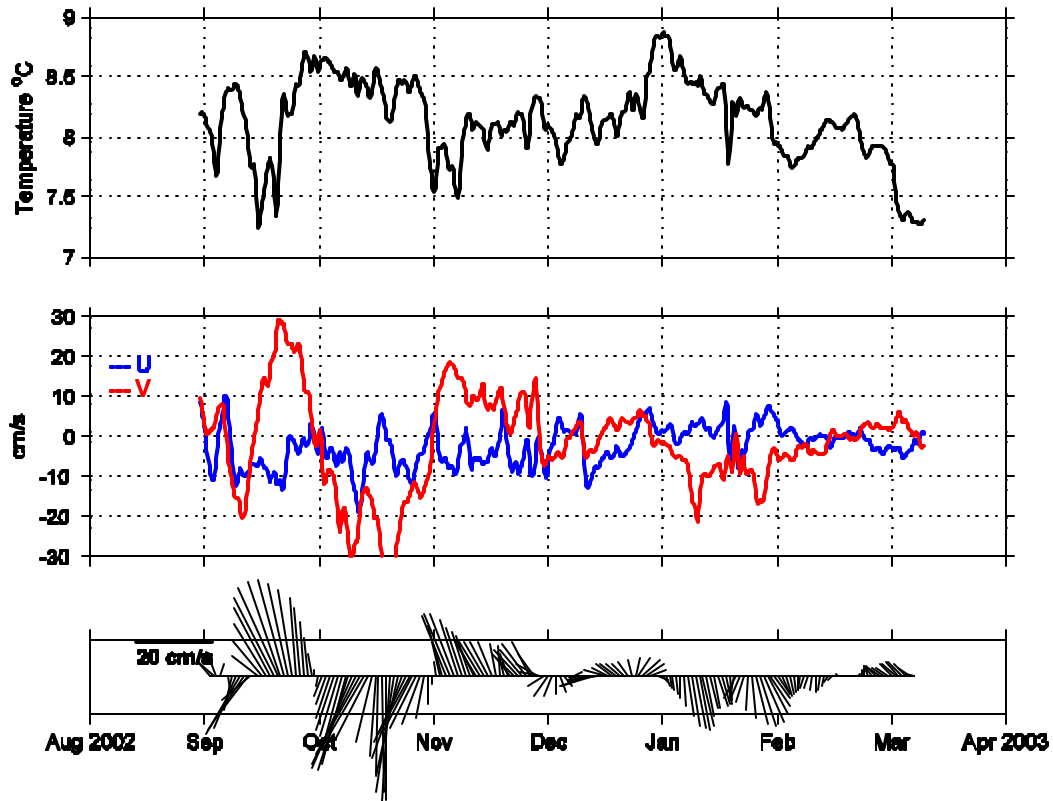
Mean Direction: 331.3 (true north)

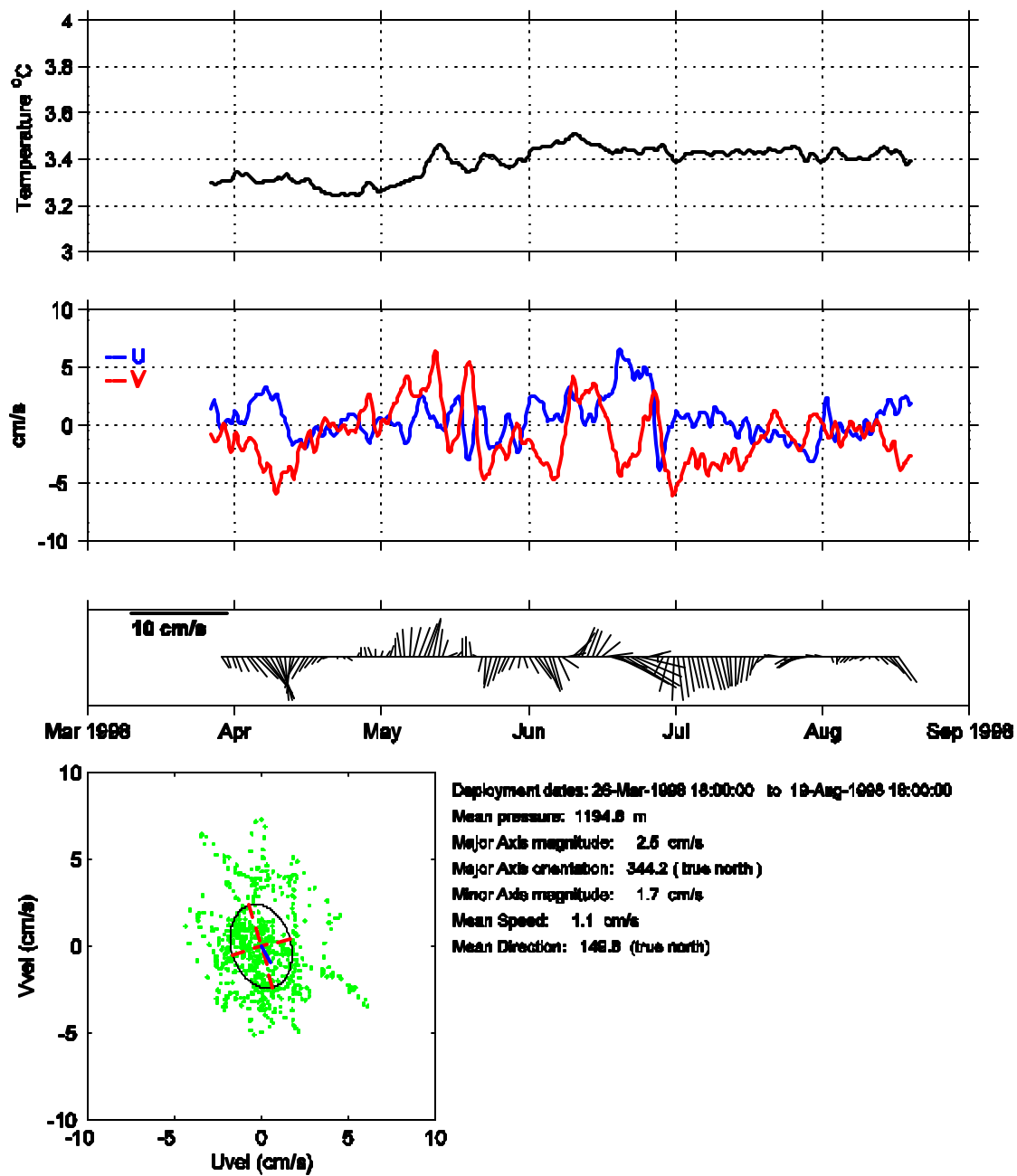


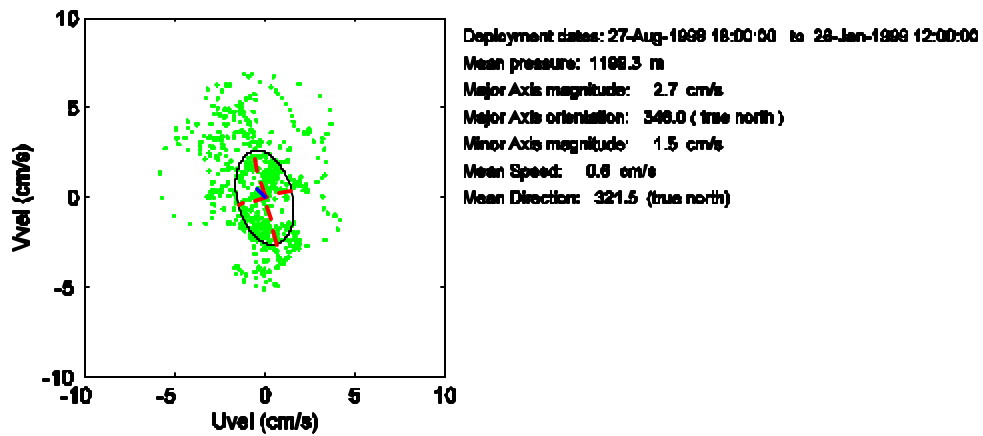
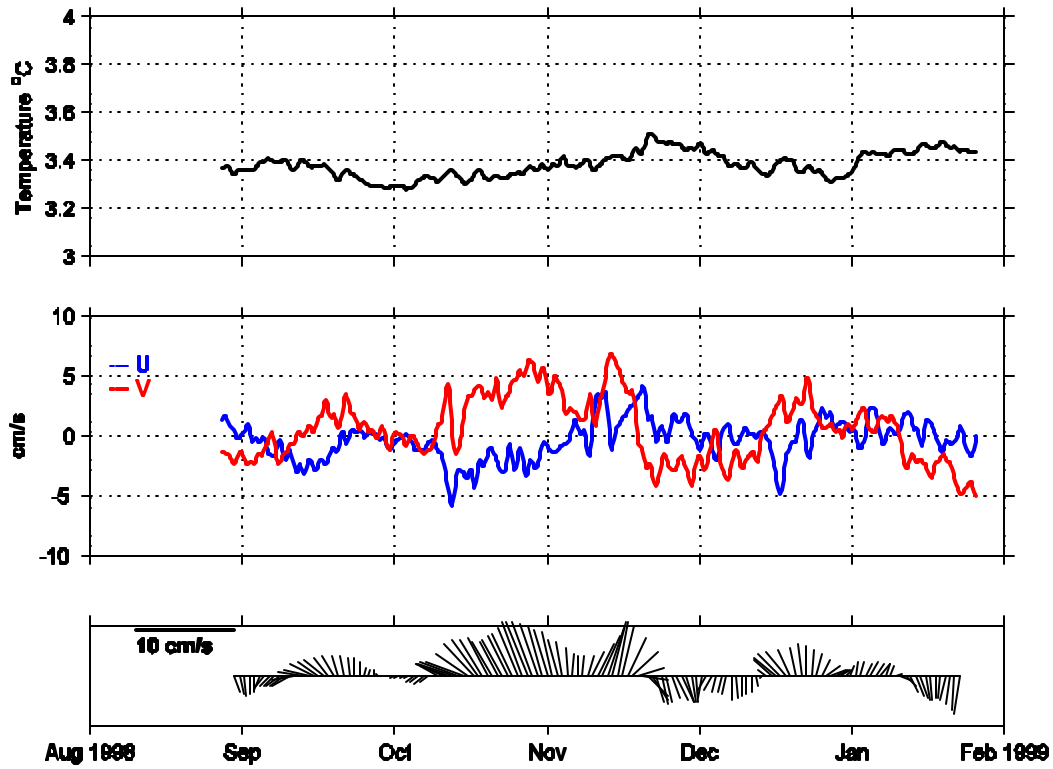


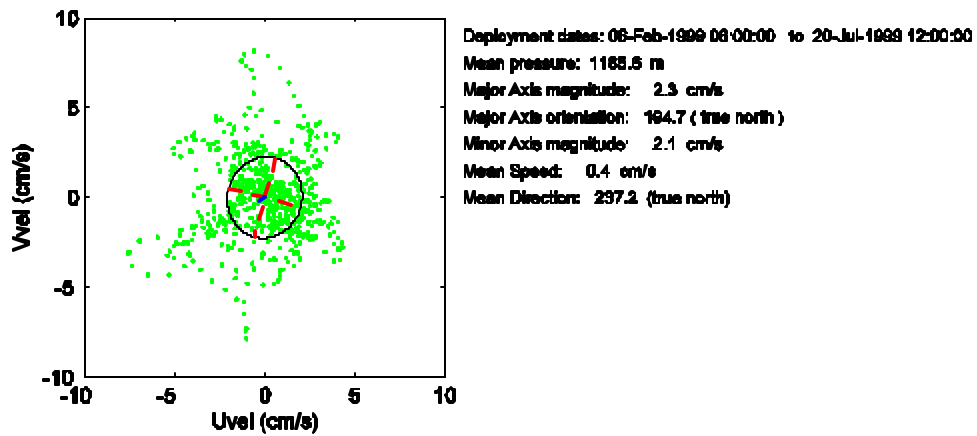
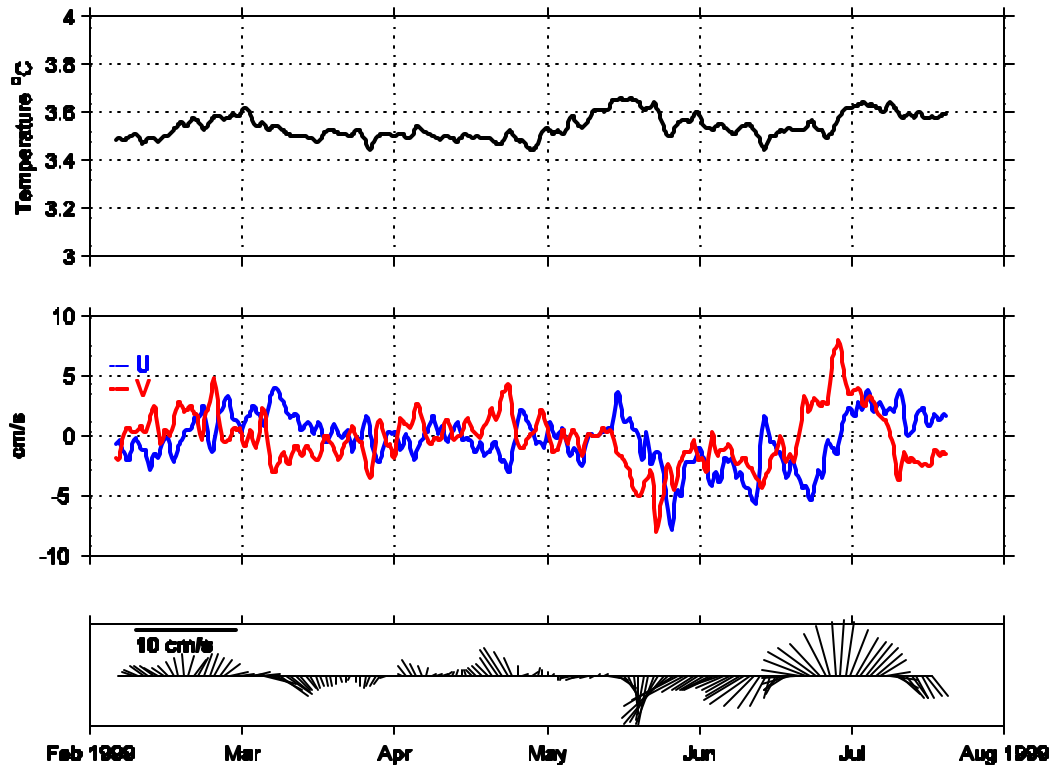


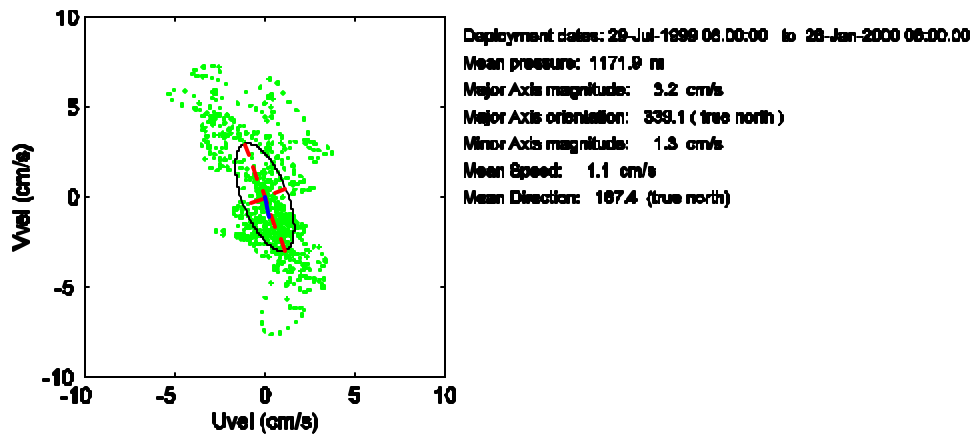
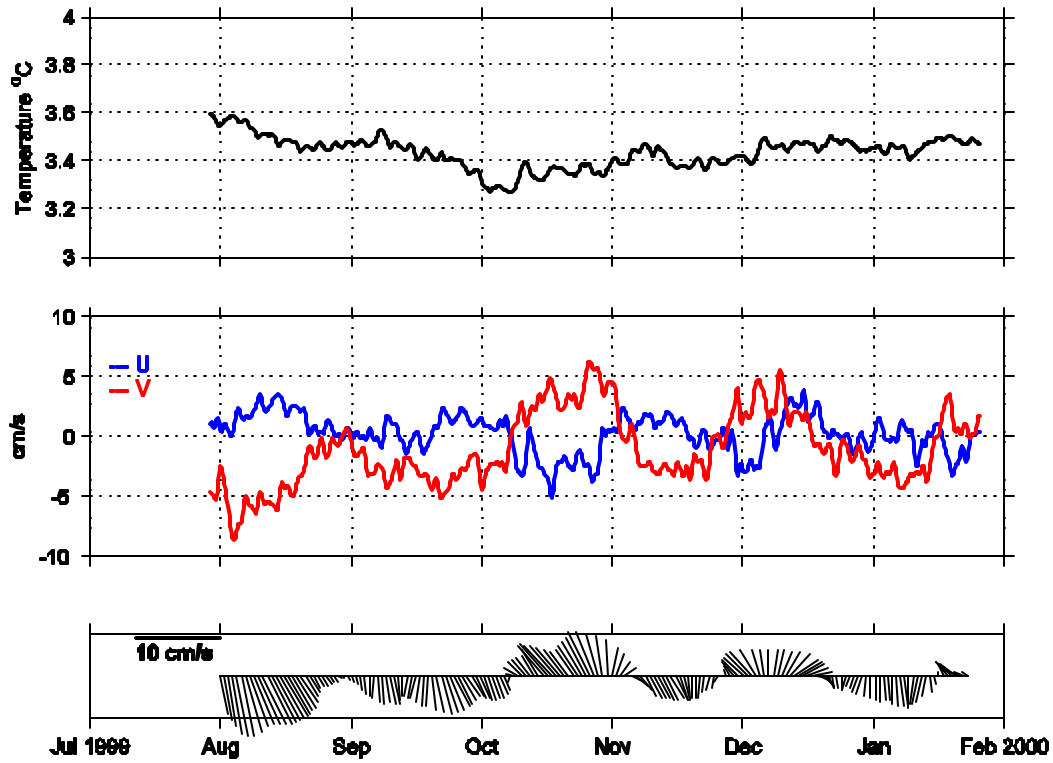


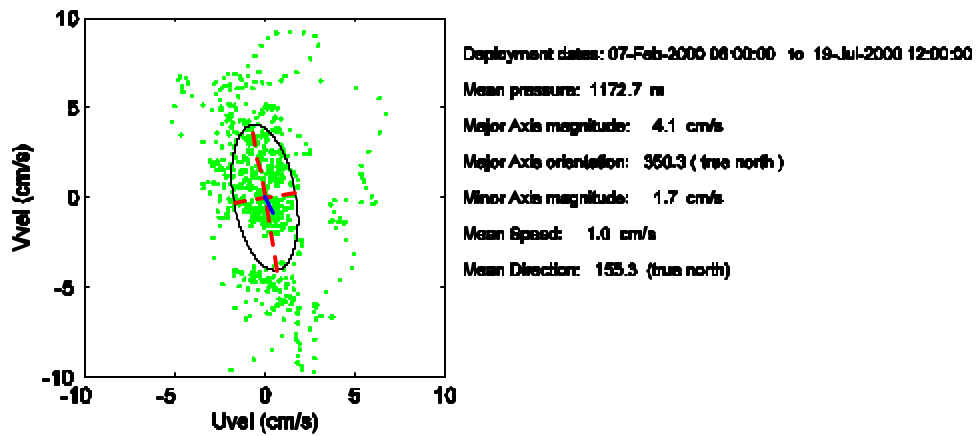
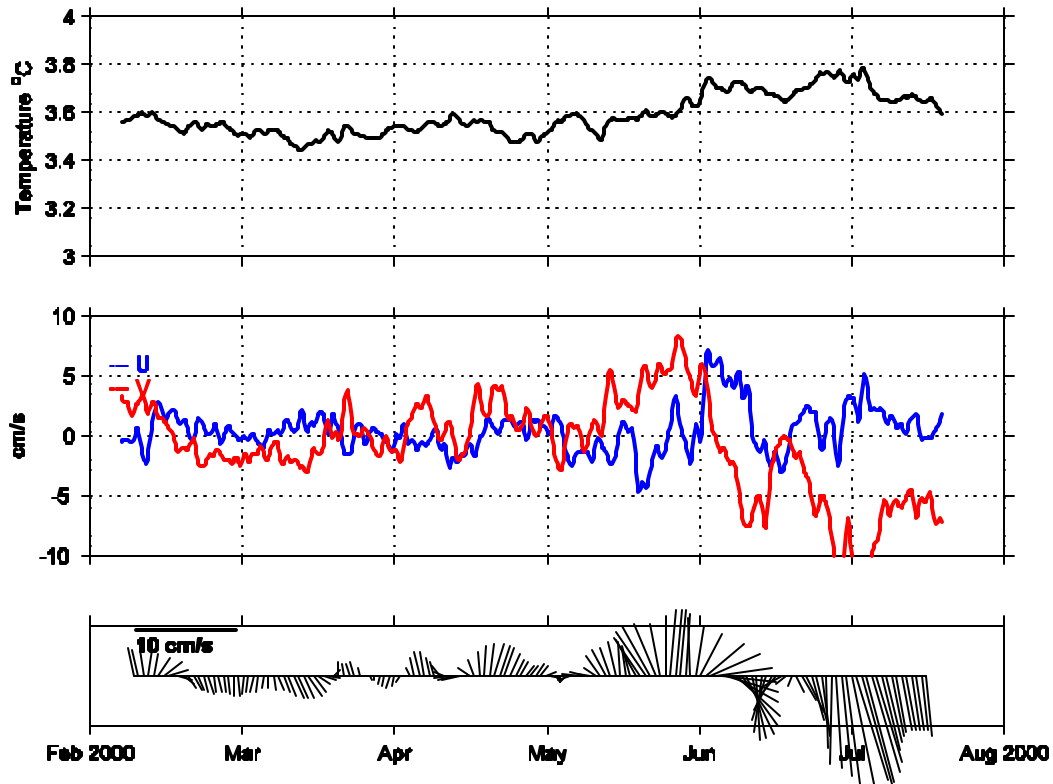


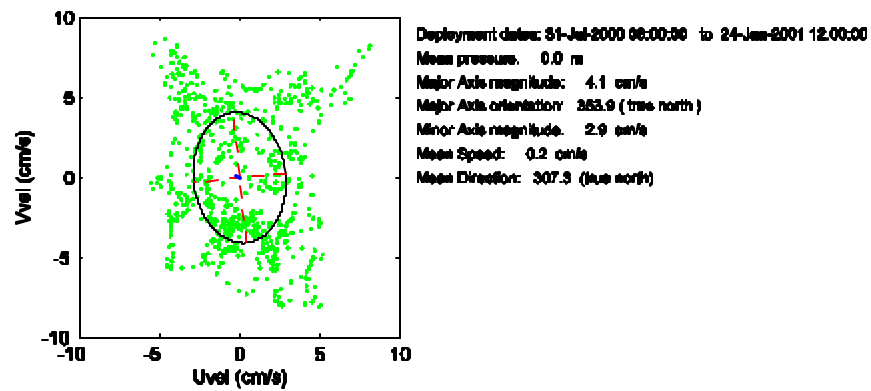
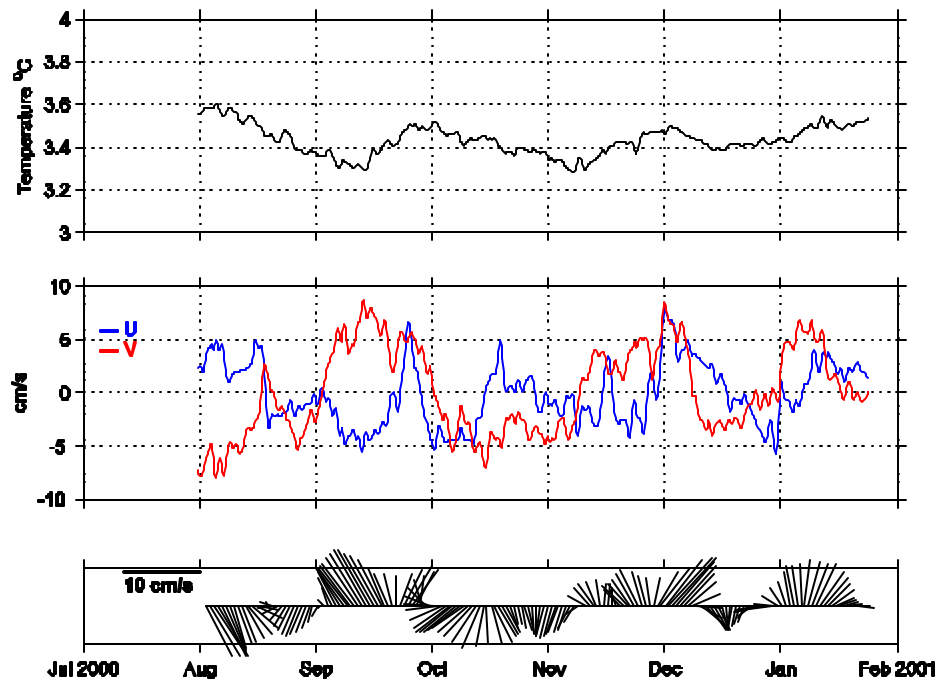


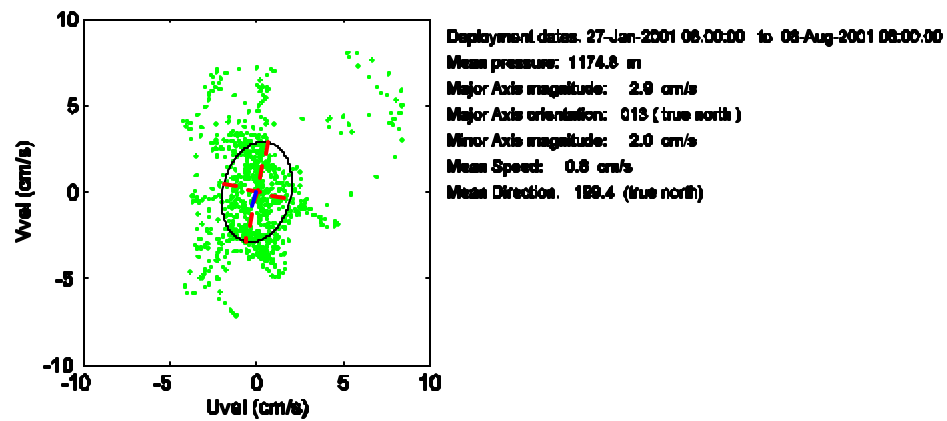
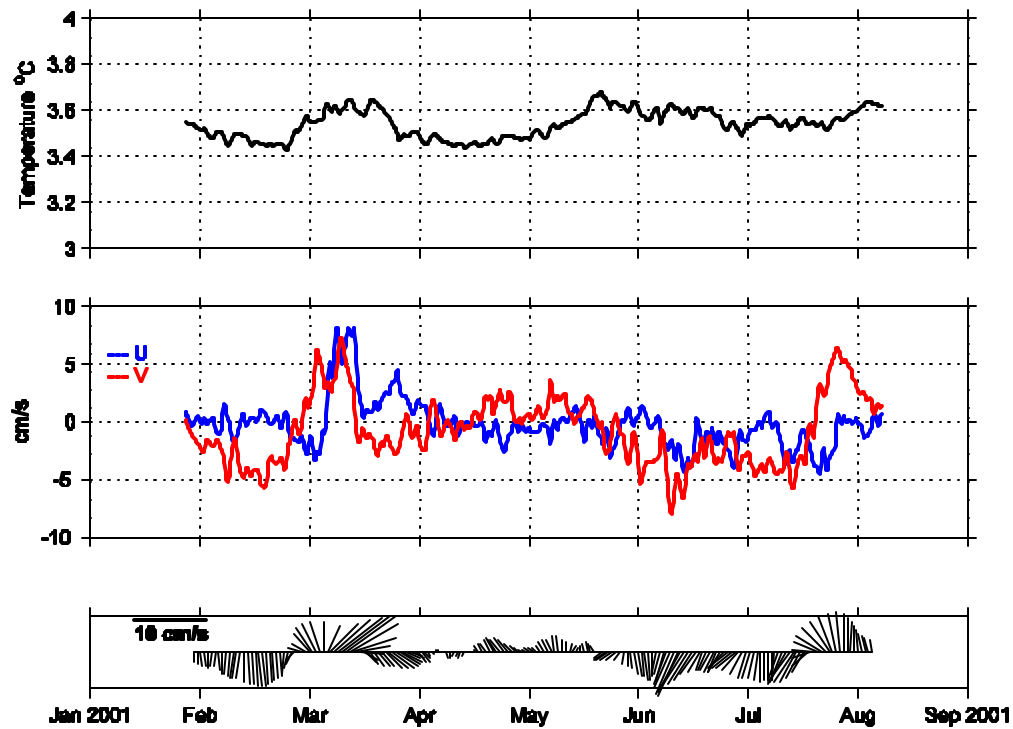


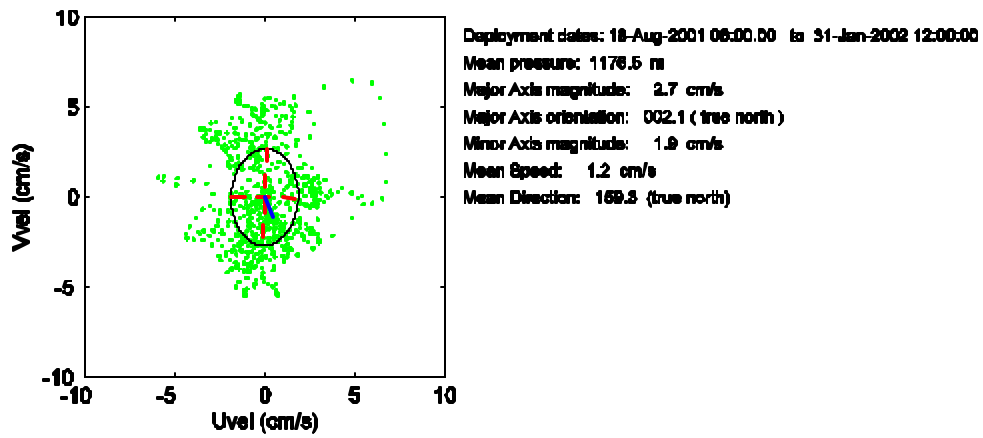
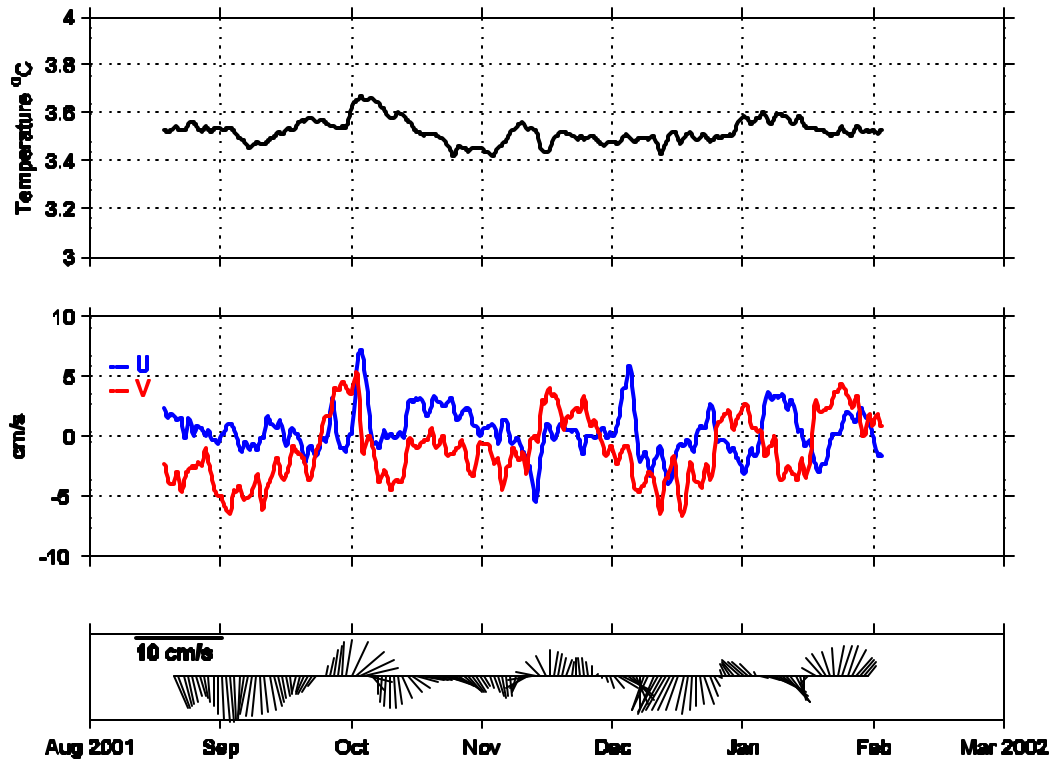


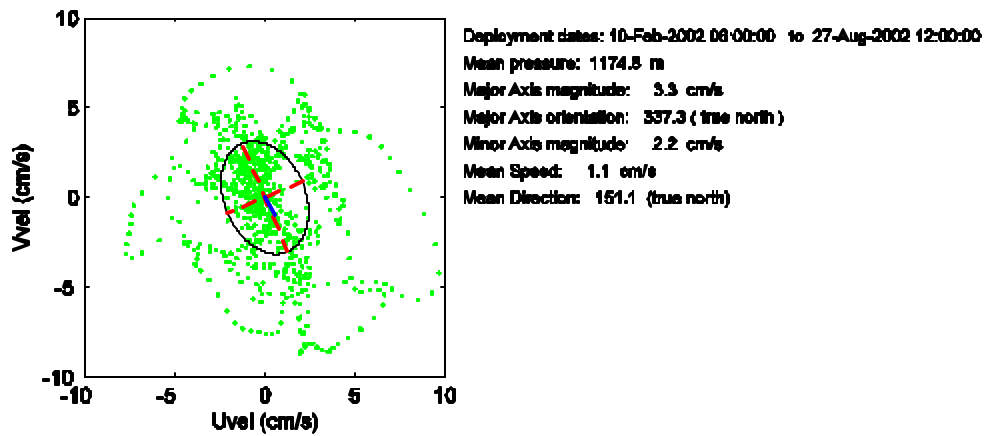
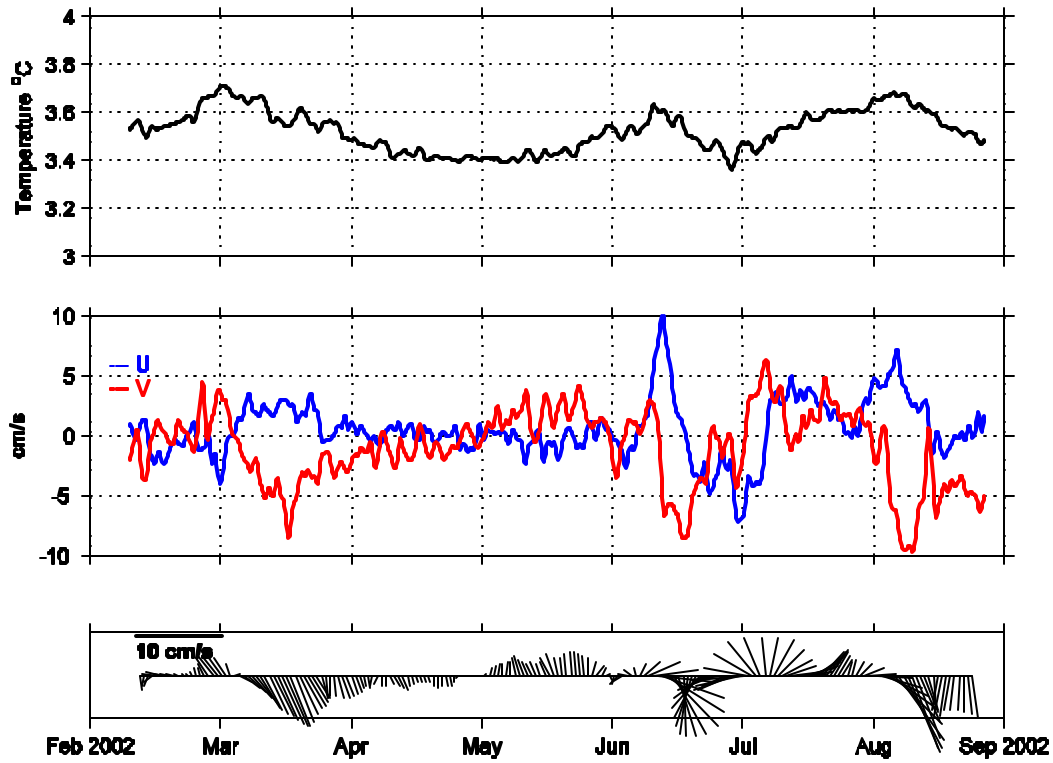


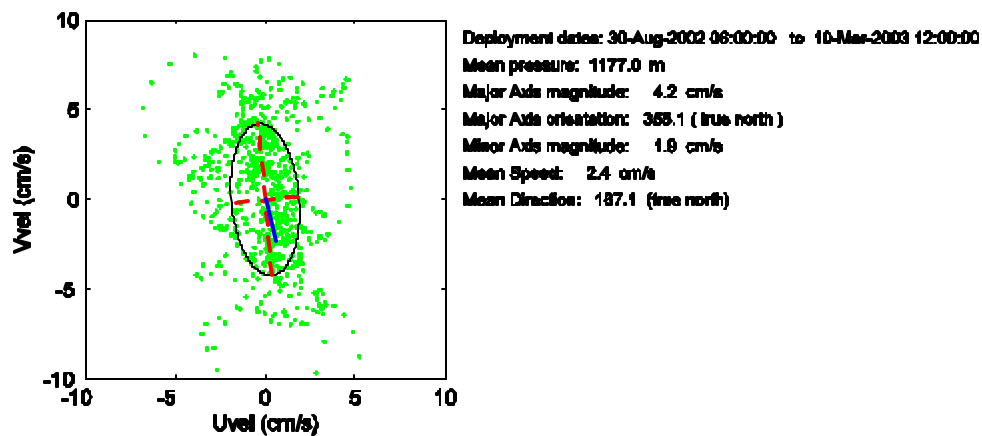
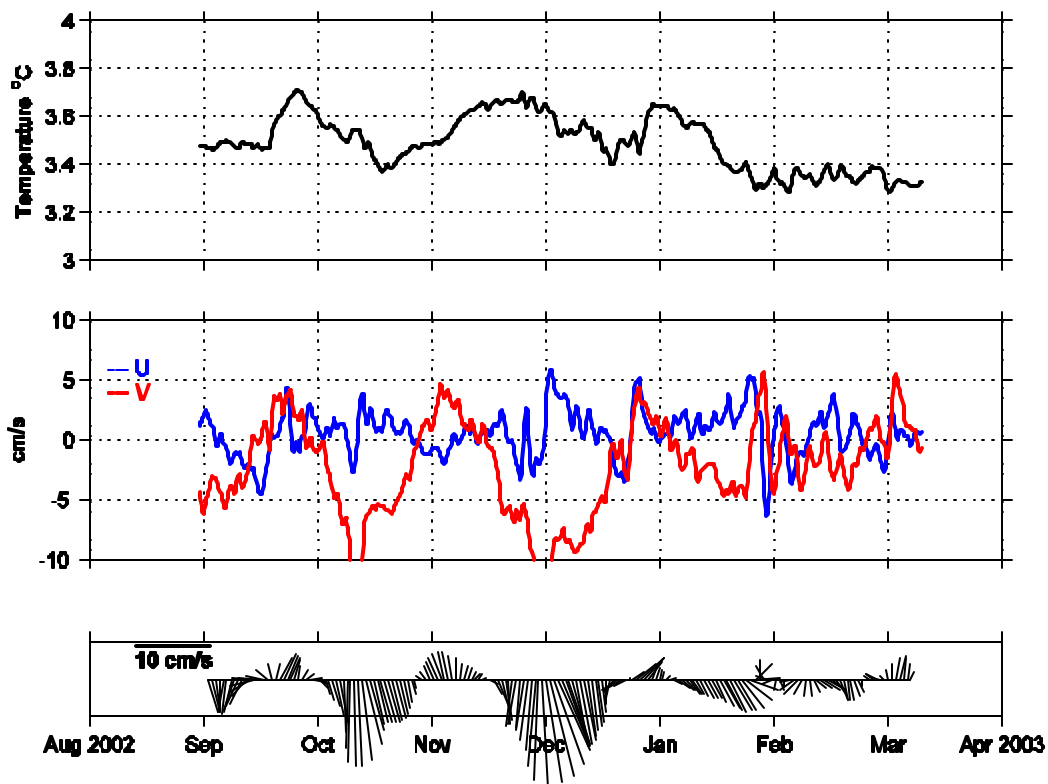












THIS PAGE INTENTIONALLY LEFT BLANK

LIST OF REFERENCES

Alessi, C. A., R. C. Beardsley, R. Limeburner, and L. K. Rosenfeld. 1985. *CODE-2: Moored Array and Large-Scale Data Report*. WHOI Technical Report No. 85-35. Woods Hole, MA. Woods Hole Oceanographic Institution. 14 pp.

Batteen, M. L. 1997. *Wind-forced modeling studies of currents, meanders, and eddies in the California Current system*. Journal of Geophysical Research, 102. No. C1. 985-1010.

Batteen, M. L. and P. W. Vance. 1998. *Modeling studies of the effects of wind forcing and thermohaline gradients on the California Current System*. Deep Sea Research II, 4. 1507-1556.

Bendat, J. S. and A. G. Piersol. 1986. *Random Data, Analysis and Measurement Procedures*. 2nd Ed., John Wiley and Sons, Inc., N. Y. 594 pp.

Breaker, L. C. and W. W. Broenkow. 1994. *The Circulation of Monterey Bay and related processes*. Oceanography and Marine Biology: an Annual Review, 32. 1-64.

Chelton, D. B. 1984. *Seasonal Variability of Alongshore Geostrophic Velocity Off Central California*. Journal of Geophysical Research, 89. No. C3. 3473-3486.

Chereskin, T. K., M. Y. Morris, P. P. Niiler, P. M. Kosro, R. L. Smith, S. R. Ramp, C. A. Collins, and D. L. Musgrave. 2000. *Spatial and temporal characteristics of the mesoscale circulation of the California Current from eddy-resolving moored and shipboard measurements*. Journal of Geophysical Research, 105. No. C1. 1245-1269.

Collins, C. A. 1968. *Description of measurements of current velocity and temperature over the Oregon continental shelf, July 1965-February 1966*. Deep Sea Research II, 47. 765-782.

Collins, C. A., C. G. Castro, H. Asanuma, T. A. Rago, S. K. Han, R. Durazo, and F. P. Chavez. 2003. *The California Current System off Monterey, California: Physical and Biological Coupling*. Deep Sea Research II, 50. 2389-2404.

Collins, C. A., N. Garfield, T. A. Rago, F. W. Rischmiller, and E. Carter. 2000. *Mean structure of the inshore countercurrent and California undercurrent off Point Sur, California*. Deep Sea Research II, 47. 765-782.

Collins, C. A., R. G. Paquette, and S. R. Ramp. 1996. *Annual Variability of Ocean currents at 350 m depth over the continental slope off Point Sur, California*. CalCOFI Reports, 37. 257-263.

Denbo, D. W., and J. S. Allen. 1984. *Rotary Empirical Orthogonal Function Analysis of Currents near the Oregon Coast*. Journal of Physical Oceanography, 14. No. C12. 35-46.

Dronkers, J. J. 1964: *Tidal computations in rivers and coastal waters*. North-Holland Publishing Company, Amsterdam, Interscience Publishers, N.Y. 518 pp.

Duxbury, A. C., and A. Duxbury. 1999. *An introduction to the world's oceans*. Addison-Wesley, Reading, MA., 549 pp.

Emery, W. J. and R. E. Thompson. 1997. *Data Analysis Methods in Physical Oceanography*. Pergamon, New York, 638 pp.

Garfield, N., C. A. Collins, R. G. Paquette, and E. Carter. 1998. *Lagrangian Exploration of the California Undercurrent, 1992-1995*. Journal of Physical Oceanography, 29. No. C12. 560-583.

Godin, G. 1972. *The analysis of tides*. University of Toronto Press, Toronto, 264 pp.

Hickey, B. M. 1979. *California Current System-Hypotheses and facts*. Progress in Oceanography, 8. 191-279.

Hickey, B. M. 1998. *Western North America, tip of Baja California to Vancouver Island*. In: The Sea, 11, Wiley, New York, 345-393.

Huyer, A. 1999. *Shelf Circulation*, In: The Sea, 9, Wiley, New York, 423-466.

Lisitzin, E. and J. G. Pattullo. 1961. *The Principal Factors Influencing the Seasonal Oscillation of Sea Level*. Journal of Geophysical Research, 66. No. 3. 845-852.

Lynn, R. J. and J. J. Simpson. 1987. *The California Current System: The Seasonal Variability of its Physical Characteristics*. Journal of Geophysical Research, 92. No. C12. 12947-12966.

MBARI. Monterey Bay Aquarium Research Institute.
http://www.mbari.org/oasis/mooring_map4.jpg June 19, 2003.

Mooers, C. N. K. 1973. *A technique for the cross spectrum analysis of pairs of complex-valued time series, with emphasis on properties of polarized components and rotational invariants*. Deep Sea Research, 20. 1129-1141

Noble, M. A. and S. R. Ramp. 2000. *Subtidal currents over the central California slope: evidence for offshore veering of the undercurrent and for direct, wind-driven slope currents*. Deep-Sea Research II, 47. 871-906.

Paduan, J. D. and L. K. Rosenfeld. 1996. *Remotely sensed surface currents in Monterey Bay from shore-based HF radar (Coastal Ocean Dynamics Application Radar)*. Journal of Geophysical Research, 101. No. C9. 20669-20686.

Pawlowicz, R., B. Beardsley, and S. Lentz. 2002. *Classical Tidal Harmonic Analysis Including Error Estimates in MATLAB using T_TIDE*. Computers and Geosciences 28, 929-937.

Pennington, J. T. and F. P. Chavez. 2000 *Seasonal fluctuations of temperature, salinity, nitrate, chlorophyll and primary production at station H3/M1 over 1989-1996 in Monterey Bay, California*. Deep-Sea Research II, 47. 947-973.

Pickard, G. L. and W. J. Emery. 1964. *Descriptive Physical Oceanography*. Pergamon, New York, 249 pp.

Pierce, S. D., R. L. Smith, P. M. Kosro, J. A. Barth, and C. D. Wilson. 2000. *Continuity of the poleward undercurrent along the eastern boundary of the mid-latitude north Pacific*. Deep-Sea Research II, 47. 811-829.

Pugh, D. T. 1986. *Tides, Surges and Mean Sea Level*. John Wiley and Sons, N.Y. 472 pp.

Ramp, S. R., L. K. Rosenfeld, T. D. Tisch, and M. R. Hicks. 1997. *Moored observations of the current and temperature structure over the continental slope off central California I. A basic description of the variability*. Journal of Geophysical Research, 102. No. C10. 22877-22902.

Rischmiller, F. W. 1993. *Variability of the California Current System off Point Sur, California, from April 1988 to December 1990*. M.S. thesis, Department of Oceanography, Naval Postgraduate School, Monterey, CA. 159 pp.

Rosenfeld, L. K., F. B. Schwing, N. Garfield, and D. E. Tracy. 1994. *Bifurcated flow from an upwelling center: a cold water source for Monterey Bay*. Continental Shelf Research, 14. No. 9. 931-964.

Skogsberg, T. 1936. *Hydrography of Monterey Bay, California. Thermal conditions, 1929-1933*. Transactions of the American Philosophical Society, 29. 1-152.

Strub, P. T., J. S. Allen, A. Huyer, and R. L. Smith. 1987. *Seasonal Cycles of Currents, Temperatures, Winds, and Sea Level over the Northeast Pacific Continental Shelf: 35° N to 48° N*. Journal of Geophysical Research, 92. No. C2. 1507-1526.

Tisch, T. D., S. R. Ramp, and C. A. Collins. 1992. *Observations of the Geostrophic Current and Water Mass Characteristics off Point Sur, California, From May 1988 Through November 1989*. Journal of Geophysical Research, 97. No. C8. 12535-12555.

INITIAL DISTRIBUTION LIST

1. Dudley Knox Library
Naval Postgraduate School
Monterey, CA
2. Dr. Curtis A. Collins
Department of Oceanography, OC/Co
Naval Postgraduate School
Monterey, CA
3. Reginaldo Durazo
UABC Facultad de Ciencias Marinas
Ensenada, B.C., MEX
4. Mr. Thomas A. Rago
Department of Oceanography, OC/Rg
Naval Postgraduate School
Monterey, CA
5. Dr. Mary L. Batteen
Department of Oceanography, OC/Bv
Naval Postgraduate School
Monterey, CA
6. Library
Moss Landing Marine Laboratories
California State Colleges
Moss Landing, CA
7. Dr. Francisco Chavez
Monterey Bay Aquarium Research Institute
Moss Landing, CA
8. Dr. Leslie Rosenfeld
Department of Oceanography, OC/Ro
Naval Postgraduate School
Monterey, CA
9. Dr. Erika Shaw
Naval Postgraduate School
Monterey, CA

10. Dr. Carmen Castro
IIS CSIC
Eduardo Cabello,6
36208 Vigo
Espana.
11. Dr. Steven Bograd
NMFS WASC Route: F/SWC6
PH: (831) 648-8314
Steven.Bograd@noaa.gov
12. Dr. Marlene Noble
U.S. Geological Survey
345 Middlefield Rd. MS 999
Menlo Park CA. 94025
mnoble@usgs.gov
13. Ms. Marla Stone
Department of Oceanography, OC/So
Naval Postgraduate School
Monterey, CA
14. Dr. Steve Ramp
Department of Oceanography, OC/Ra
Naval Postgraduate School
Monterey, CA
15. Dr. Jeff Paduan
Department of Oceanography, OC/Pd
Naval Postgraduate School
Monterey, CA
16. Dr. Robert L. Smith
College of Oceanic and Atmospheric Sciences
Oregon University
Corvallis. OR.
17. ENS. Alicia Washkevich
Naval Postgraduate School
Monterey, CA